DESIGN AND SIMULATION OF INTRACAVITY FORWARDS AND BACKWARDS OPTICAL PARAMETRIC OSCILLATORS

DESIGN AND SIMULATION OF INTRACAVITY FORWARDS AND BACKWARDS OPTICAL PARAMETRIC OSCILLATORS

By JOSHUA KNELLER, B.Eng.

A Thesis Submitted to the School of Graduate Studies in Partial Fulfilment of the Requirements for

the Degree Doctor of Philosophy

McMaster University DOCTOR OF PHILOSOPHY (2024)

Hamilton, Ontario (Department of Engineering Physics)

TITLE: Design and Simulation of Intracavity Forwards & Backwards Optical Parametric Oscillators

AUTHOR: Joshua Kneller, B.Eng. (McMaster University)

SUPERVISOR: Professor Chang-Qing Xu

NUMBER OF PAGES: xiii, 131

i Abstract

Intracavity optical parametric oscillators are an attractive method for generating light throughout the infrared (IR) wavelength range due to their ability to simultaneously achieve high output powers and narrow linewidths. Despite the extensive volume of literature published on this type of laser, there are gaps in existing models that must be addressed to aid in the development of these lasers. A new model for an intracavity backwards optical parametric oscillator (IC-BOPO) is proposed to determine the feasibility of using periodically poled lithium niobate (PPLN) as a nonlinear material in a continuous wave IC-BOPO. It is shown that it is possible to reach the laser threshold when using a low power laser diode as the pump source and a commercially available off-the-shelf PPLN. It is also shown that the proposed laser is capable of achieving watt level output power with picometer linewidth at mid-infrared wavelength using a 20 W pump laser diode. To further optimize the lasers, a systematic study is presented which investigates the effects of multiple parameters on the laser performance such as nonlinear crystal length, cavity size, output coupler radius and pump laser spot size. Additionally, effects such as thermal lensing and beam overlap within the nonlinear crystal are considered. With proper cavity setup, it is possible to reach the laser threshold with PPLN crystal as short as 2 cm with a 10 W pump laser diode. A new model for a passively Q-switched intracavity optical parametric oscillator (IC-OPO) is also presented. The effects of thermalization, excited state absorption in the Q-switch crystal, beam

overlap in the nonlinear crystal and nonlinear loss due to pump depletion in the nonlinear crystal are all considered. The model accurately calculates both the temporal and output power characteristics of the laser. The calculated signal pulse width from the model was 1.75 ns compared to the experimentally measured value of 2 ns.

ii Acknowledgements

There are many people I would like to thank, who have supported me throughout this journey. I would first like to thank every member of my research group for always being available to listen to my ramblings and providing help wherever possible. I would like to especially like to thank Bin for teaching me how to build a laser and always being there to find the flaw in one of my ideas, Liam for our conversations on different models and methods for simulating laser performance, Tyler for being willing to fabricate all the crystals used in my experiments, and Saeed for your endless patience when completing tedious experiments.

I am thankful for the support of my entire family who encouraged me through every step of this process. To my aunts, uncles and cousins, I am incredibly grateful for all that you have done for me from the beginning and the support you continue to show. To all the friends I made along the way, thank you for being there to make this stressful journey a little brighter. Sorry for every time I made you listen to my ramblings of the latest in laser research.

I would like to extend thanks to my committee members Dr. Bradley and Dr, Fang, whose wisdom and experience were invaluable.

Finally, I would like to thank my grandparents for always believing in me and for trying their best to remember what type of lasers I designed. Thank you to my mother for always believing in me, especially when I didn't. Thank you to my partner

Melissa for your endless support throughout this long journey. There is no way it would have been possible without you. Lastly, thank you to my supervisor Dr. Xu for constantly sharing your seemingly endless knowledge with me and always guiding me to the approach and answer to any problem I encountered. Without your guidance this would not have been possible.

iii Table of Contents

iv Table of Figures

v Table of Tables

vi List of Abbreviations

IR – Infrared

IC-BOPO – Intracavity Backwards Optical Parametric Oscillator

IC-OPO – Intracavity Optical Parametric Oscillator

PPLN – Periodically Poled Lithium Niobate

OPO – Optical Parametric Oscillator

CW - Continuous Wave

DRO – Doubly Resonant Optical Parametric Oscillator

SRO – Singly Resonant Optical Parametric Oscillator

KTP – Potassium Titanyl Phosphate

IC - Intracavity

PP – Periodically Poled

BOPO – Backwards Optical Parametric Oscillator

PPKTP – Periodically Poled Potassium Titanyl Phosphate

Mid-IR – Middle Infrared

GHG – Greenhouse Gas

DPSS – Diode Pumped Solid State

QPM – Quasi Phase Matching

OC – Output Coupler

PF – Parametric Fluorescence

SPDC – Spontaneous Parametric Down Conversion

Nd:YVO4 – Neodymium Doped Yttrium Orthovanidate

Cr:YAG – Chromium Doped Ytterbium Aluminum Garnet

GSA – Ground State Absorption

ESA – Excited State Absorption

Nd:YAG – Neodymium Doped Yttrium Aluminum Garnet

LiDAR – Light Detection and Ranging

DIAL – Differential Absorption Light Detection and Ranging

IPDA – Integrated path Differential Absorption

FWHM – Full Width Half Maximum

NIR – Near Infrared

QCL – Quantum Cascade Laser

ICL – Interband Cascade Laser

HR – High Reflection

AR – Anti-Reflection

HT – High Transmission

vii Declaration of Authorship

I, Joshua Kneller, declare that this thesis, "Design and Simulation of Intracavity Forwards and Backwards Optical Parametric Oscillators", was authored by and contains research work performed by the author, in consultation with Dr. Chang-Qing Xu, with the following exceptions:

Chapter 5: Saeed Salimian Rizi assisted with experimental measurements.

This thesis has resulted in three journal publications of which I am the first author and main contributor.

1. **J. Kneller**, L. Flannigan, and C.-Q. Xu, "Theoretical study of diode pumped intracavity backward optical parametric oscillator based on periodically poled lithium niobate," *Appl. Phys. B*, vol. 129, no. 6, p. 99, 2023, doi: 10.1007/s00340-023-08045-4.
2. **J. Kneller**, L. Flannigan, and C.-Q. Xu, "Design Considerations for Continuous Wave Intracavity Backwards Optical Parametric Oscillators," *Photonics*, vol. 11, no. 4. 2024, doi: 10.3390/photonics11040318.
3. **J. Kneller**, S. Salimian Rizi, L. Flannigan, and C. Xu, "The effects of thermalization on the performance of passively Q-switched IC-OPOs," *Front.*

Phys., vol. 12, 2024, [Online]. Available:

https://www.frontiersin.org/journals/physics/articles/10.3389/fphy.2024.142867

1 Introduction

1.1 Background and Motivations

Since it's demonstration in 1960 [1], the laser has undergone rapid development resulting in its integration into many aspects of modern society. With applications in numerous fields such as metrology, spectroscopy, communication, surgery, video display, defense, the laser is a truly versatile technology.

The development of nonlinear optics followed shortly after the first laser with the demonstration of second harmonic generation in crystalline quartz [2]. Not long after this, the first demonstration of an optical parametric oscillator (OPO) was reported with a pulsed pump source [3], [4]. Due to the high input intensities required, initial operation of OPOs was limited to pulsed operation as this allowed for the required threshold intensities to be met. As laser technology improved, sources capable of operating in continuous wave (CW) at high enough intensities were developed allowing for CW OPOs to be realized [5]. Along with the developments of improved laser sources, different OPO setups were utilized to improve the device's performance. The first CW OPO was achieved using a doubly resonant structure, termed a doubly resonant OPO (DRO), where both generated wavelengths were confined within the OPO cavity. This structure has the benefit of reducing the threshold pump power for the nonlinear interaction [5]. DROs however, suffer from reduced output wavelength stability and tunability as a result of the doubly resonant structure [3], [6]. The use of a singly resonant OPO (SRO) where only one of the generated wavelengths is confined within the cavity reduces both of these issues at the cost of a higher pumping threshold [6].

Despite the early achievement of a CW DRO, achieving an SRO remained a much more difficult task due to the low nonlinear gain available under CW pumping and the confinement of only one of the generated waves. Realization of an SRO required a high intensity pump source and a high-quality nonlinear material with a large nonlinearity. In 1993 the first CW SRO was demonstrated, using a 532 nm frequency doubled Nd:YAG laser and a potassium titanyl phosphate (KTP) nonlinear crystal [7]. The SRO used a dual pass pump setup to reduce the threshold of the nonlinear interaction and achieve CW operation [8]. An improved OPO structure where the nonlinear crystal and OPO cavity are placed within the pump cavity, termed an intracavity OPO (IC-OPO), was another major development in OPO technology [9]. The IC structure allowed for a greater flexibility in OPO design the pumping threshold and output wavelength stability were no longer limiting factors. Since then, a tremendous amount of progress has been made in IC-OPO performance and modeling [10], [11], [12]. Another important development in OPO technology, and nonlinear optics, was the development of periodically poled (PP) materials, first proposed in 1962 [13], and first demonstrated in an OPO in 1996 [14].

An advantage of the OPO is the tunability of the output wavelength without the need to change anything in the laser design. By changing the temperature of the nonlinear crystal, the phase matching condition is modified. This results in new output wavelengths. Temperature tuning allows for continuous tuning of the output wavelengths of an OPO. Additionally, many of the nonlinear crystals used in OPOs have large transparency windows, with some reaching into the far infrared (IR), enabling a wide range of possible output wavelengths [15], [16].

In addition to the OPO, another nonlinear interaction was proposed in the early days of nonlinear optics known as backwards optical parametric amplification (BOPO) [17]. Similar to the OPO, two fields are generated within a nonlinear crystal, however in the case of the BOPO one of the generated waves counter-propagates relative to the other two. However, unlike the success that was seen by the OPO, the BOPO remained elusive due to the large momentum mismatch caused by the counterpropagating idler wave. It wasn't until 2007 that the device was first realized using PPKTP [18]. Since then, numerous experimental and theoretical papers have been published, paving the way for a new generation of lasers based on BOPOs [19], [20], [21].

Of particular interest is the development of lasers capable of high-power emission in the middle infrared (mid-IR) wavelength range [22], [23], [24]. Trace gas detection and monitoring has become increasingly important in recent years as the effects of greenhouse gasses on the atmosphere have been of concern [25]. As a result of this accurate, real time, monitoring of greenhouse gas concentrations within the atmosphere is needed. Many of the Greenhouse Gases (GHGs) of interest, such as methane and nitrous oxide, have their strongest absorption lines within the mid-IR wavelength range. As such, lasers sources capable of emitting in this wavelength range are highly demanded.

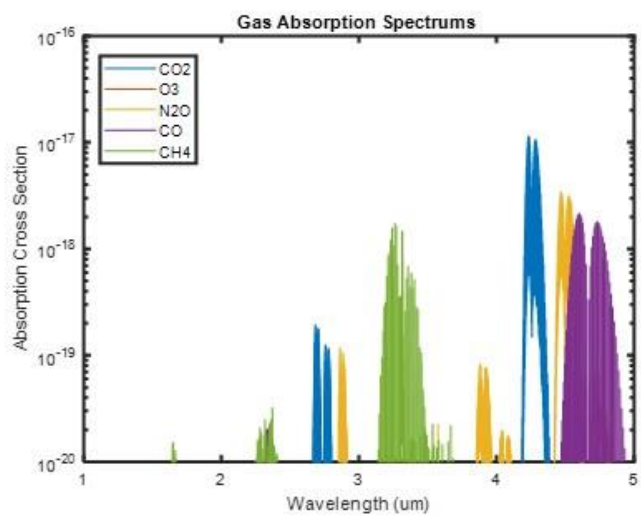

Figure 1-1: Absorption spectrums of various gasses taken from the HITRAN database.

1.2 Objectives

The objectives of this research are to develop improved models of IC-OPO and IC-BOPO lasers based on periodically poled lithium niobate (PPLN). The research explores different physical phenomena and how they affect the performance of the forementioned devices, resulting in high quality models capable of exploring both temporal and spatial effects.

The IC-OPO has been discussed extensively in literature since its first demonstration. Numerous models have been developed to predict and model the behavior observed experimentally [26], [27], [28], [29]. Despite this however, there is currently no model capable of accurately predicting the temporal characteristics of passively Q-switched IC-OPOs. Additionally, these models focus only of the time domain and do not account for the spatial variation in intensity within the nonlinear crystal.

Recently, the first experimental demonstration of the BOPO was reported [18]. Despite the attractiveness of the BOPO, it remains poorly reported in literature due to a number of reasons. The first is the difficulty in manufacturing a PP crystal with a small enough period to satisfy the phase matching condition of the nonlinear interaction. Currently, it has only been demonstrated in PPKTP [18], [20], [21]and only with pulsed pumping. Theoretical work has been reported analyzing the potential of other material such as PPLN to be used in pulsed BOPOs and found that it is feasible. However, the use of other materials has only been analyzed in single pass pump configurations. Theoretical studies have also been reported investigating CW BOPOs using single pass pumping. There are no theoretical reports analyzing the potential for the BOPO to be operated in CW using an IC structure, as is done with the IC-OPO.

1.3 Thesis Outline

Chapter 2 covers the underlying physics of the devices discussed within this thesis. It begins by giving a brief overview of the origin of nonlinear optics and discusses the derivation of nonlinear phenomena related to this work. Following this, the coupled wave equations that were previously derived are used to explain the operating principles of single pass OPOs and BOPOs in both pulsed and continuous wave operation. The next section details the operating principles of intracavity OPOs and BOPOs. To fully understand the operating principles of these devices' additional models for intracavity diode pumped solid state (DPSS) lasers and passively Q-switched DPSS lasers are also described. Finally, a method for coupling these models with the coupled wave equations to simulate intracavity OPOs and BOPOs is presented and discussed.

Chapter 3 discusses the feasibility of using PPLN to achieve CW operation in an IC-BOPO. It is shown that using 5th order quasi phase matching within PPLN, a CW IC-BOPO can be realized by using a rate equation model for a DPSS laser coupled with the coupled wave equations of nonlinear optics. The performance of the device is discussed, including threshold, output power and output linewidth; and shown to be acceptable for applications such as greenhouse gas detection.

Chapter 4 builds the work presented in Chapter 3 by performing a theoretical systematic study of the proposed device to optimize performance. Parameters such as nonlinear crystal length, cavity length, and output coupler radius are varied, with their effects on device performance discussed in-depth.

Chapter 5 proposes a new model for a passively Q-switched IC-OPO to allow for the accurate calculation of temporal pulse characteristics. A new set of rate equations for a passively Q-switched DPSS laser are proposed and used to model the temporal profile and output energy of the pulse. The theoretical results are compared to experimentally obtained results and discussed. Finally, the coupled wave equations are integrated into the rate equation model to simulate a passively Q-switched IC-OPO, again comparing the results to experimentally obtained results.

The following is a list of work completed by the author which appear in this thesis:

4. **J. Kneller**, L. Flannigan, and C.-Q. Xu, "Theoretical study of diode pumped intracavity backward optical parametric oscillator based on periodically poled lithium niobate," *Appl. Phys. B*, vol. 129, no. 6, p. 99, 2023, doi: 10.1007/s00340-023-08045-4.
5. **J. Kneller**, L. Flannigan, and C.-Q. Xu, "Design Considerations for Continuous Wave Intracavity Backwards Optical Parametric Oscillators," *Photonics*, vol. 11, no. 4. 2024, doi: 10.3390/photonics11040318.
6. **J. Kneller**, S. Salimian Rizi, L. Flannigan, and C. Xu, "The effects of thermalization on the performance of passively Q-switched IC-OPOs," *Front. Phys.*, vol. 12, 2024, [Online]. Available:

https://www.frontiersin.org/journals/physics/articles/10.3389/fphy.2024.142867

1.

2 Theory

2.1 Nonlinear Origin

When the light is incident on a medium the electric field, $\vec{E}$, of the light induces a polarization, $\vec{P}$, in the medium. When the intensity of the field is low, the polarization of the medium is linearly proportional to the incident electric field. The linear relationship between the electric field and the polarization can be expressed as:

$$\vec{P} = \varepsilon_0 \chi^{(1)} \vec{E} \tag{1}$$

where $\chi^{(1)}$ is the linear susceptibility of the medium and ε_0 is the permittivity of free space. When the intensity of the incident light is increased, the linear relationship between the electric field and the induced polarization begins to breakdown. To describe this, it is common to express the polarization as a power series of the electric field strength as [30]:

$$\vec{P} = \varepsilon_0 \left[\chi^{(1)} \vec{E} + \chi^{(2)} \vec{E}^2 + \ldots \right] \tag{2}$$

where $\chi^{(2)}$ is the second order nonlinear susceptibility of the medium [30].

To understand how the nonlinear polarization affects an electromagnetic wave travelling through a dielectric we must analyze Maxwells equations. The four Maxwell equations in a dielectric may be written as:

$$\nabla \bullet \vec{E} = \frac{\rho}{\varepsilon_0} \tag{3}$$

$$\nabla \times \vec{E} = -\frac{\partial \vec{B}}{\partial t} \tag{4}$$

$$\nabla \bullet \vec{B} = 0 \tag{5}$$

$$c^2 \nabla \times \vec{B} = \frac{\partial \vec{E}}{\partial t} + \frac{\vec{J}}{\varepsilon_0} \tag{6}$$

where $\vec{E}$ is the electric field, ρ is the total charge density, ϵ_0 is the permittivity of free space, $\vec{B}$ is the magnetic field flux density, c is the speed of light in a vacuum and $\vec{J}$ is the current density. The total charge density contains both the bound, ρ_b, and free charge density, ρ_f, such that $\rho = \rho_b + \rho_f$. Since we are considering a wave propagating through a dielectric material the free charge density is 0, so the total charge density is equal to the bound charge density. The bound charge density is related to the polarization of the medium by:

$$\rho = \rho_b = -\nabla \bullet \vec{P} \tag{7}$$

Similarly to the bound charge, the total current density is also equal to the sum of the bound and free current density. As was the case for the free charge density, the free current density is also zero, so the total current density is equal to the bound current density. This can be related to the polarization as:

$$\vec{J} = \vec{J}_b = \frac{\partial \vec{P}}{\partial t} \tag{8}$$

where $\overrightarrow{J_b}$, is the bound current. Eqs.(7) & (8) can be substituted into Eqs. (3) - (6) to give:

$$\nabla \bullet \vec{E} = \frac{-\nabla \bullet \vec{P}}{\varepsilon_0} \tag{9}$$

$$\nabla \times \vec{E} = -\frac{\partial \vec{B}}{\partial t} \tag{10}$$

$$\nabla \bullet \vec{B} = 0 \tag{11}$$

$$c^2 \nabla \times \vec{B} = \frac{\partial \vec{E}}{\partial t} + \frac{1}{\varepsilon_0}\frac{\partial \vec{P}}{\partial t} \tag{12}$$

In a homogeneous dielectric, a net surface charge density is created due to the polarization while the internal bound charge density remains zero. From this we can state that $\nabla \cdot \vec{E} = 0$. Taking the curl of Eq. (10) and simplifying the left-hand side using the previous observation $\nabla \times (\nabla \times E) = \nabla\left(\nabla \cdot \vec{E}\right) - \nabla^2 \vec{E} = -\nabla^2 \vec{E}$, we get:

$$\nabla^2 \vec{E} = \frac{\partial}{\partial t}\left(\nabla \times \vec{B}\right) \tag{13}$$

From here substituting Eq. (12) into Eq. (13) gives:

$$c^2 \nabla^2 \vec{E} = \frac{\partial^2 \vec{E}}{\partial t^2} + \frac{1}{\varepsilon_0}\frac{\partial^2 \vec{P}}{\partial t^2} \tag{14}$$

The polarization as expressed in Eq. (2) can be separated into the linear and nonlinear parts as $\vec{P} = \epsilon_0 \chi^{(1)} \vec{E} + \vec{P}^{NL}$, where P^{NL} is the nonlinear components of the polarization, and substituted into the last equation to give:

$$c^2 \nabla^2 \vec{E} = \frac{\partial^2 \vec{E}}{\partial t^2} + \frac{1}{\varepsilon_0}\frac{\partial^2 (\varepsilon_0 \chi^{(1)} \vec{E} + \vec{P}_{NL})}{\partial t^2} \tag{15}$$

Simplifying and grouping like terms in the above equation gives:

$$\nabla^2 \vec{E} - \frac{\varepsilon_r}{c^2}\frac{\partial^2 \vec{E}}{\partial t^2} = \frac{1}{c^2 \varepsilon_0}\frac{\partial^2 \vec{P}_{NL}}{\partial t^2} \quad (16)$$

where $\epsilon_r = 1 + \chi^{(1)}$and is the relative permittivity of the dielectric. Assuming the wave travels only in the z direction the equation becomes:

$$\frac{\partial^2 \vec{E}}{\partial z^2} - \frac{\varepsilon_r}{c^2}\frac{\partial^2 \vec{E}}{\partial t^2} = \frac{1}{c^2 \varepsilon_0}\frac{\partial^2 \vec{P}_{NL}}{\partial t^2} \quad (17)$$

The solutions to the wave equation are:

$$\vec{E}_n(z,t) = E_n(z)e^{i(k_n z - \omega_n t)} + c.c. \quad (18)$$

$$\vec{P}_n(z,t) = P_n(z)e^{-i\omega_n t} + c.c. \quad (19)$$

where c.c. is the complex conjugate, ω_n is the angular frequency on the nth field. For three wave mixing processes there are three fields present: the pump, signal and idler. The fields have been assumed to be constant in time, making the above derivation only valid for CW input at a constant intensity. Inserting Eqs. (18) & (19) into Eq. (17), and making the slowly varying envelope approximation to eliminate the second order derivative gives:

$$\frac{\partial \overrightarrow{E_n}(z)}{\partial z} = i\frac{\omega_n}{2\varepsilon_0 c n_n}\vec{P}_n^{NL}(z) \quad (20)$$

where n_n is the material refractive index at the fields wavelength. The nonlinear source term P^{NL} for each of the three fields is:

$$\vec{P}_p = 2\varepsilon_0 d_{eff}\vec{E}_s\vec{E}_i \quad (21)$$

$$\vec{P}_s = 2\varepsilon_0 d_{eff}\vec{E}_p\vec{E}_i \quad (22)$$

$$\vec{P}_i = 2\varepsilon_0 d_{eff}\vec{E}_p\vec{E}_s \quad (23)$$

where the subscripts p,s and i refer to the pump, signal and idler field, respectively. d is the nonlinear coefficient of the material used.

2.2 Phase Matching

The wavelengths of the two generated waves are determined by the conservation of energy and the phase matching condition. The conservation of energy requires that the sum of the energy of the signal & idler photon be equal to the energy of the pump photon. The phase matching condition is given by the equation:

$$\Delta k = k_p - k_s - k_i \quad (24)$$

where Δk is the phase mismatch, k_p is the pump wavevector, k_s is the signal wavevector and k_i is the idler wavevector. The phase matching condition is satisfied when the phase mismatch is equal to 0.

Achieving perfect phase matching is possible through use of a birefringent crystal and precisely aligning the angular orientation of said crystal so that the refractive index of each of the beams satisfies Eq. (24) [30]. In practice this is quite difficult due to the need for precise alignment and limits the choice of nonlinear material to ones which exhibit birefringence. The need for a precise crystal orientation also limits the ability to use the orientation of the crystal which would have the largest nonlinear coefficient.

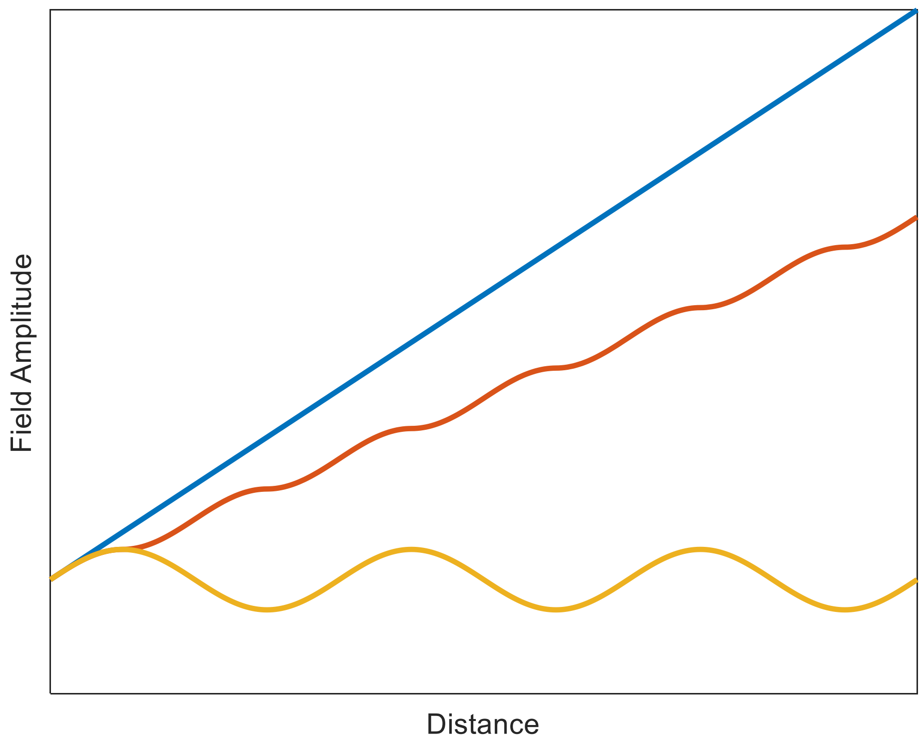

Figure 2-1: Conversion efficiency of different phase matching methods.

blue is perfect phase matching, orange is quasi phase matching and yellow is no phase matching

An alternative to perfect phase matching is quasi phase matching (QPM). QPM works by periodically inverting the sign of the nonlinear coefficient of the material such that the interaction is always positive, resulting in efficient energy transfer into the generated wavelengths. The effect of poling on the phase matching condition can be expressed as:

$$\Delta k = k_p - k_s - k_i - {}^{2\pi}\!/_{\Lambda} \tag{25}$$

where Λ is the poling period. From Eq. (25) it is possible to select the output signal and idler wavelengths by choosing an appropriate poling period.

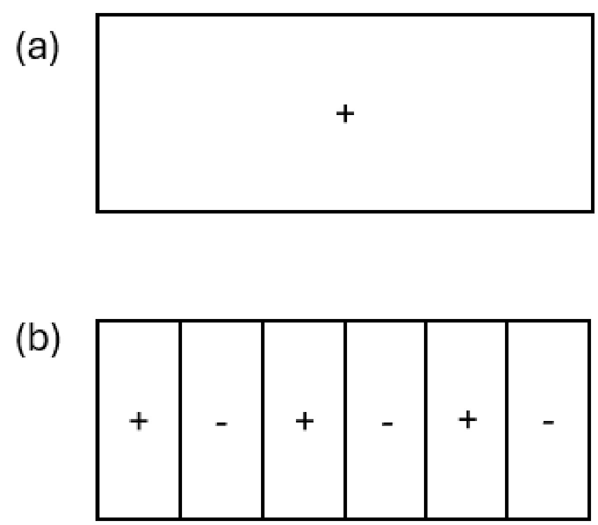

Figure 2-2: a) unpoled nonlinear crystal, b) nonlinear crystal with poling

2.3 Single Pass OPO

The OPO is based on a second order nonlinear interaction and as such requires a medium with a nonzero second order nonlinear susceptibility. In an OPO the nonlinear crystal is placed within a resonator. The OPO is a three-wave mixing process where a pump field is incident upon the nonlinear crystal, resulting in the splitting of the pump photons into signal and idler photons. The signal refers to the generated photon with the shorter wavelength, while the idler refers to the longer wavelength photon. As two wavelengths are generated, a single OPO can be used as either a near- or mid-IR source depending on the design of the cavity. If the design goal is to achieve a near-IR emitting OPO, where the useful emission is at the signal wavelength, the cavity output coupler (OC) is generally partially reflecting at the signal wavelength, lowering the signal confinement within the OPO cavity but increasing the output. If the goal is to achieve high power mid-IR operation, then the OC is generally set to be highly reflecting at the signal wavelength, to nearly perfectly confine the signal wave to increase the conversion efficiency of the idler wave.

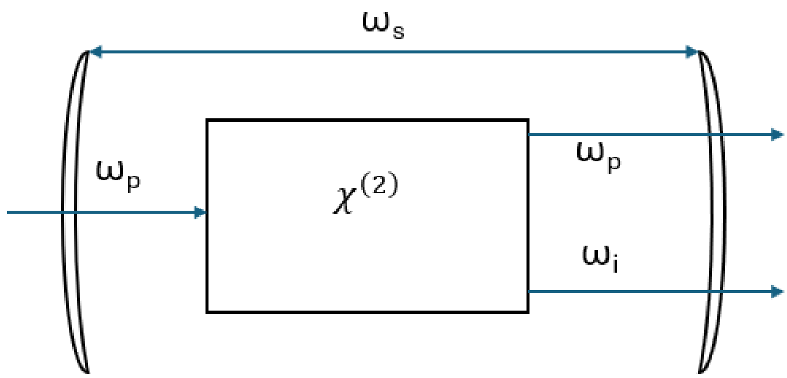

Figure 2-3: Diagram of an OPO where the signal wave is confined and the idler is coupled out of the OPO cavity.

The three coupled wave equations which describe the OPO can be found by inserting Eqs. (21) - (23) into Eq. (20) which results in:

$$\frac{\partial \vec{E}_p(z)}{\partial z} = i\frac{\omega_p}{cn_p}\chi^{(2)}\vec{E}_s(z)\vec{E}_i(z)e^{-i\Delta k} \tag{26}$$

$$\frac{\partial \vec{E}_s(z)}{\partial z} = i\frac{\omega_s}{cn_s}\chi^{(2)}\vec{E}_p(z)\vec{E}_i^{*}(z)e^{i\Delta k} \tag{27}$$

$$\frac{\partial \vec{E}_i(z)}{\partial z} = i\frac{\omega_i}{cn_i}\chi^{(2)}\vec{E}_p(z)\vec{E}_s^*(z)e^{i\Delta k} \tag{28}$$

where the asterisk represents the complex conjugate of the respective field.

Placing the nonlinear crystal within a resonator allows for the buildup of one of the generated waves; increasing the device efficiency and also lowering the pump threshold required.

2.3.1 Spontaneous Parametric Down Conversion/Parametric Fluorescence

From the coupled wave equations for the OPO presented in the previous section it is clear that in order to obtain a nonzero output, two of the three fields must have an initial nonzero value. This requires there to be an additional input field besides the pump field at either the signal or idler wavelength. The answer to this is that the signal and idler fields are initially generated through a quantum mechanical process where a pump photon is split into two photons, which become the input to the signal and idler fields in the coupled wave equation. The process of the pump photon splitting into the signal and idler photon is required to satisfy both the conservation of energy as well as the phase matching condition. This process is known as parametric fluorescence (PF) or spontaneous parametric down conversion (SPDC).

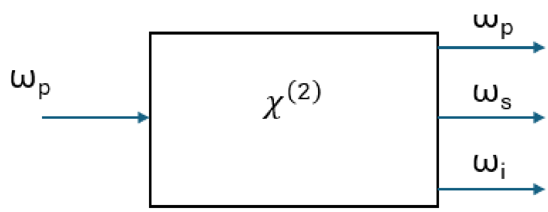

Figure 2-4: Diagram of the SPDC process.

The process of PF can be described as a quantum mechanical probability that a pump photon will spontaneously split into two photons of lower energy such that the energy of the two photons is equal to the pump photon energy. Another description of the process is the zero point energy fluctuations of the signal and idler fields. The quantum noise of a single mode, assuming a half photon per mode [19], [31], can be calculated as:

$$E = \sqrt{\frac{\hbar\omega}{w_0^2 L\pi\varepsilon_0 n}} \tag{29}$$

PF is a linear process dependent only on the pump intensity, when in a bulk crystal [32], and as a result is the dominant process at low pump intensities. As the signal and idler fields build within the crystal the contribution from the coupled wave equations becomes larger until it becomes the dominant process at which point PF becomes insignificant.

2.4 Single Pass BOPO

The single pass BOPO functions similarly to the single pass OPO, the difference being one of the two generated waves counter propagates relative to the pump. This requires that the phase matching condition of the BOPO be modified from Eq. (25) to:

$$\Delta k = k_p - k_s + k_i - {}^{2\pi}\!/_{\Lambda} \tag{30}$$

where we have assumed that it is the idler wave which counter propagates relative to the pump and have changed the sign of its wave vector to account for this. As a result, there is a much larger momentum mismatch between the three waves, requiring a much shorter poling period to satisfy the phase matching condition. It also worth mentioning that either the signal or idler can be made to counter propagate, but since the idler wave is defined as the wave with the longer wavelength, the momentum mismatch is smaller when it is the one which counter propagates. The smaller momentum mismatch makes achieving a BOPO with a counter propagating idler waves easier. For the purpose of this we will always refer to the idler as the counter propagating wave unless explicitly stated.

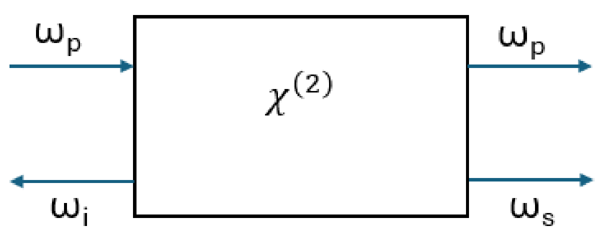

Figure 2-5: BOPO nonlinear interaction where the idler counter-propagates relative to the input pump

Despite the difficulties in achieving the required phase matching condition, there is a great interest in the development of a BOPO due to two properties. The first is that the counter propagating waves allow for effective oscillation without the need for an external cavity structure. This greatly reduces the device size and lowers the risk of misalignment when compared to a standard OPO. The second property is that the counter propagating wave will have a narrow linewidth, often on the order of 10s of pm, while the forward travelling waves spectrum will be a wavelength shifted replica of the pumps spectrum. This differs from the standard OPO, where both waves typically have a linewidth on the order of nm. To show this, we can expand Eq. (30) as a first order taylor series and assume the pump spectrum to be a delta function:

$$\Delta\omega_{BOPO} = \frac{2.7831}{\left|\frac{1}{v_{g,s}} + \frac{1}{v_{g,i}}\right| L} \tag{31}$$

where $\Delta\omega_{BOPO}$ is the emission bandwidth, $v_{g,s}$ and $v_{g,i}$ are the signal and idler group velocity, respectively, and L is the nonlinear crystal length. The factor 2.7831 rad is the phase mismatch accumulated throughout the crystal at which point the conversion efficiency drops to 50%. To compare to the OPO the same process can be done with Eq. (25):

$$\Delta\omega_{OPO} = \frac{2.7831}{\left|\frac{1}{v_{g,s}} - \frac{1}{v_{g,i}}\right| L} \tag{32}$$

Comparing the two equations, the denominator in the BOPO case will be larger resulting in a smaller emission bandwidth than the OPO.

In the above analysis the effect of the pump bandwidth was not considered. The wavelength tuning rate of the signal and idler with respect to the pump can also be calculated using the phase matching equation as:

$$\frac{\partial \omega_s}{\partial \omega_p} = \frac{v_{g,i}\left(v_{g,p} + v_{g,i}\right)}{v_{g,p}\left(v_{g,i} + v_{g,s}\right)} \tag{33}$$

and

$$\frac{\partial \omega_i}{\partial \omega_p} = \frac{v_{g,i}\left(v_{g,p} - v_{g,i}\right)}{v_{g,p}\left(v_{g,i} + v_{g,s}\right)} \tag{34}$$

From the above equations, the idler tuning rate with respect to the pump is expected to be smaller than that of the signal wave. The rate $\partial \omega_i / \partial \omega_p$ is generally around 0.01 (depending on the material used) while the rate $\partial \omega_s / \partial \omega_p$ is typically 1.01. As a result the idler wave bandwidth is expected to be much smaller than the pump, while the signal waves spectrum is essentially a phase shifted copy of the pumps. This allows for the BOPO to be used as a tunable source of high power mid-ir light while also achieving an narrow emission linewidth.

2.5 Pulsed Pumping

When deriving the previous coupled wave equations, it was assumed that the electric field was constant in time, representing a CW input. In order to properly model an OPO/BOPO under pulsed pumping the time dependence of the electric field and nonlinear polarization must also be considered. The time dependent electric field and polarization solution to the wave equation is:

$$\vec{E}_n(z,t) = E(z,t)e^{i(k_n z - \omega_n t)} + c.c. \tag{35}$$

$$\vec{P}_n(z,t) = P(z,t)e^{-i\omega_n t} + c.c. \tag{36}$$

Substituting these equations into the wave equation and following the same process as before gives the time dependent coupled wave equations:

$$\frac{\partial \vec{E}_p(z)}{\partial z} + \frac{1}{c}\frac{\partial \vec{E}_p(t)}{\partial t} = i\frac{\omega_p}{cn_p}\chi^{(2)}\vec{E}_s(z)\vec{E}_i(z)e^{-i\Delta k} \tag{37}$$

$$\frac{\partial \vec{E}_s(z)}{\partial z} + \frac{1}{c}\frac{\partial \vec{E}_s(t)}{\partial t} = i\frac{\omega_s}{cn_s}\chi^{(2)}\vec{E}_p(z)\vec{E}_i^*(z)e^{i\Delta k} \tag{38}$$

$$\frac{\partial \vec{E}_i(z)}{\partial z} + \frac{1}{c}\frac{\partial \vec{E}_i(t)}{\partial t} = i\frac{\omega_i}{cn_i}\chi^{(2)}\vec{E}_p(z)\vec{E}_s^*(z)e^{i\Delta k} \tag{39}$$

In the above equations the time dependence of the electric field has been maintained allowing for the study of time dependent phenomena such as pulsed pumping.

2.6 CW Intracavity OPOs/BOPOs

In the previous discussion a single pass OPO was considered, where the pump field makes only a single pass through the OPO cavity. Another OPO configuration which is commonly used to increase the output power of the generated waves and lower the device threshold is the IC-OPO. In this setup the OPO cavity is placed within the pump cavity, increasing the pump intensity incident on the nonlinear crystal and as a result also increasing the conversion efficiency of the nonlinear process and lowering the threshold.

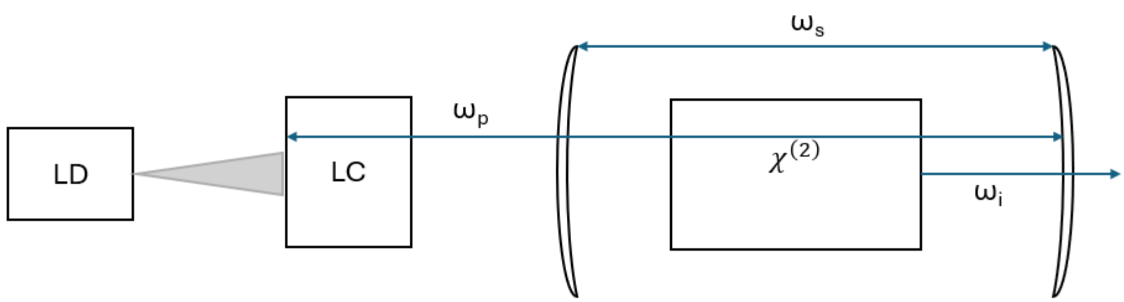

Figure 2-6: diagram of an IC-OPO. LD is the pump laser diode, LC is the laser crystal which is assumed to have a high reflection coating at the OPO pump wavelength on the left hand side.

Placing the nonlinear crystal/OPO cavity within the pump cavity also increases the complexity of the device physics. This is due to the nonlinear process creating an additional, intensity dependent, loss source within the pump cavity. This requires that the standard rate equations for the pump laser be modified to include the loss due to the nonlinear conversion process.

2.6.1 Continuous Wave Pumping

To analyze a CW IC-OPO it is first necessary to determine the circulating pump power within the cavity before considering the effects of the addition of the nonlinear crystal. Assuming that the pumping laser is a diode pumped solid state laser (DPSS), made using a 4-level laser crystal such as Nd:YVO_4, the laser power can be modeled with the transcendental equation [33]:

$$F = \frac{1 + \dfrac{B}{fS}\ln\left(1 + fS\right)}{f\displaystyle\int_0^\infty \frac{\exp\left[-\left(a^2+1\right)x\right]}{1 + fS\exp\left(-a^2 x\right)}dx} \tag{40}$$

where F is the normalized pump power from the laser diode, S is the normalized intracavity pump power, a is the ratio of the pump diode beam waist to the intracavity laser beam waist in the laser crystal, and f is the sum of the Boltzmann occupation factors of the upper and lower laser level. x is equal to:

$$x = \frac{2r^2}{w_p^2} \tag{41}$$

where r is the radius from the beam center, and w_p is the radius of the pump laser. B is the ratio of loss due to reabsorption within the laser crystal to the cavity loss and is expressed as:

$$B = \frac{2N_1^{\,0}\sigma l}{(L+T)} \tag{42}$$

where N_1^0 is the population of the lower laser level, is the gain cross section, l is the crystal length, L is the round trip cavity loss and T is the output transmission. F can be calculated as:

$$F = \frac{4P_p\tau\sigma\eta_a}{\pi h\nu_p w_L^2(L+T)} \tag{43}$$

where P_p is the pump power, τ is the upper laser level lifetime, η_a is the fraction of pump power absorbed, h is Planck's constant, ν_p is the pump diode frequency, and w_L is the intracavity laser radius. Eq. (40) can be solved numerically for the variable S by making using of Eqs. (41) - (43) and using a root finding method. S is related to the intracavity photon flux by the equation:

$$S = \frac{2c\sigma\tau\Phi}{n\pi w_L^2 l} \tag{43}$$

where Φ is the intracavity photon flux, c is the speed of light and n is the refractive index of the laser crystal at the laser wavelength. The one-way intracavity laser power is related to the cavity photon flux by the equation:

$$P_L = \frac{ch\nu_L\Phi}{2nl} \tag{44}$$

where ν_L is the intracavity laser frequency, and P_L is the one-way intracavity power.

2.6.2 CW IC-OPOs

Using the equations from the previous section to model the pump power (referring to the pump from the coupled wave equations and not the LD used to pump the laser crystal) it is possible to the calculate the output power from a CW IC-OPO. The insertion of the nonlinear crystal into the laser cavity creates two sources of additional loss. The first is due to material absorption and can be added to the cavity loss in the previous equations. The second source of loss is the pump depletion due to the nonlinear process.

The first loss source can be accounted for by calculating the pump absorption in the nonlinear crystal which occurs over two trips through the crystal, once in the forward direction and once in the backward direction. The pump loss can be converted to a percent loss and added to the cavity loss, L, in the intracavity laser equations previously presented. The loss due to the nonlinear conversion process can be found by determining the number of pump photons converted into idler photons. By the conservation of energy for every idler photon created one pump photon must be destroyed. Using the coupled wave equations to determine the total idler power, as well as using the intracavity laser model to calculate the initial input pump power to the nonlinear crystal, the percentage of pump photons converted into idler photons can be found. The nonlinear loss can be calculated as:

$$\alpha_{NL} = \frac{\lambda_i}{\lambda_p}\frac{P_i}{P_{p0}} \tag{45}$$

where P_i is the total idler power generated in both the forward and backward direction, and P_{p0} is the pump power calculated using the intracavity laser model. The total loss the pump experiences within the laser cavity can now be calculated as:

$$L = \alpha_{cav} + \alpha_{abs} + \alpha_{NL} \tag{46}$$

where α_{cav} is the cavity loss and α_{abs} is the absorption due to the nonlinear crystal. This new loss value can then be used in the intracavity laser model to determine a new input power which in turn will result in a new loss value. This process is repeated until the loss value converges on its steady state value, at which point the steady state operating conditions of the IC-OPO have been found.

2.6.3 Q-Switched Lasers

Q-switching is a passive method for obtaining pulsed output from a DPSS laser where a Q-switching crystal, such as Chromium Doped Ytterbium Aluminum Garnet (Cr:YAG), is placed within the laser cavity. The Q-switch crystal works as a saturable absorber where the absorption of light by the crystal is inversely proportional to the intensity of the incident light. The physics of saturable absorbers such as Cr:YAG can be understood by considering the energy level diagram.

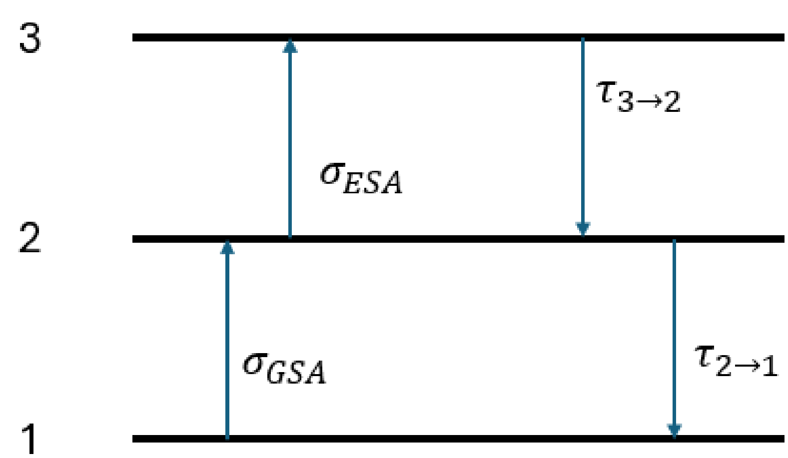

Figure 2-7:Energy level diagram of Cr:YAG

Initially, when no light is indecent on the q-switch crystal the ground state, labeled 1 in the above figure, is fully populated. As the incident intensity on the crystal increases the ground state absorption (GSA) occurs between energy levels 1→2. From energy level 2 an additional excitation can take place called the excited state absorption (ESA) which occurs between states 2→3. The lifetime of the second excited energy level is very short compared to most pulse lengths, on the order of ps [34], and so it is generally assumed that the lifetime of the third energy level is 0. The first excited state has a lifetime on the order of μs [34], which is much longer than the typical laser pulse. In Cr:YAG $\sigma_{GSA} > \sigma_{ESA}$, by about one order of magnitude. As the ground state depopulates due to absorption, the rate of absorption begins to decrease as the 2→3 transition has a much smaller cross section. Since the lifetime of the first energy level is much longer than the pulse, the population will become stuck in this state until the pulse has finished at which point the crystal will reset and return to thermal equilibrium. While the excited particles remain in the first excited state, the absorption of the Q-switch crystal is drastically reduced due to the ESA cross section being much smaller. This results in the crystal becoming nearly transparent and allowing the energy stored within the laser crystal to be released rapidly, resulting in an intense pulse. It is possible to have a fast enough pulse due to high pumping rates that the crystal cannot return to equilibrium between pulses, known as bleaching, resulting in reduced laser performance [26].

The rate equations for a passively Q-switched laser are [35], [36]:

$$\frac{d\phi}{dt} = \frac{\phi}{t_r}\left(2\sigma_e(n_a - n_b)l_g - 2\sigma_{13}n_{s1}l_{Cr} - 2\sigma_{24}\left(n_s - n_{s1}\right)l_{Cr} - L - \ln\left(R\right)\right) \tag{47}$$

$$\frac{dn_a}{dt} = W_p - \frac{n_a - f_a n_u}{\tau_{therm}} - \frac{n_a}{\tau_a} - \sigma_e c\phi\left(n_a - n_b\right) \tag{48}$$

$$\frac{dn_b}{dt} = \sigma_e c\phi\left(n_a - n_b\right) - \frac{n_b}{\tau_b} - \frac{n_b - f_b n_l}{\tau_{therm}} \tag{49}$$

$$\frac{dn_{s1}}{dt} = \frac{n_s - n_{s1}}{\tau_{sa}} - \sigma_{13}c\phi n_s \tag{50}$$

$$\frac{dn_u}{dt} = \frac{n_a - f_a n_u}{\tau_{therm}} - \frac{n_u}{\tau_a} \tag{51}$$

$$\frac{dn_l}{dt} = \frac{n_b - f_b n_l}{\tau_{therm}} - \frac{n_l}{\tau_b} \tag{52}$$

Table 1 contains a description of each variable appearing in the above rate equations.

Table 2.1: Name of each symbol appearing in Eqs. (47)-(52)

Variable	Parameter	Variable	Parameter
ϕ	IC photon density	R	Mirror loss
σ_e	Stimulated emission cross section	W_p	Pumping rate
n_a	Population of upper laser energy stark level	f_a	Ratio of upper stark level population to total level population
n_b	Population of lower laser energy stark level	n_u	Population of remaining upper stark levels
l_g	Length of gain medium	τ_{therm}	Thermalization time
σ_{13}	Absorption cross section of Cr:YAG	τ_a	Upper laser level lifetime
n_{s1}	Population density of first excited state of Cr:YAG	c	Speed of light
l_{cr}	Length of Cr:YAg crystal	f_b	Ratio of lower stark level population to total level population
σ_{24}	Absorption cross section of excited state of Cr:YAG	n_l	Population density of lower laser level
n_s	Total population of Cr:YAG	τ_b	Lifetime of lower laser level
L	Residual optical loss	τ_{sa}	Lifetime of Cr:YAG excited state

Unlike in the case of CW DPSS lasers, a steady state solution does not exist for pulse pumping, requiring the above system of equations to be solved numerically. While there are other models which solve a similar set of rate equations to come to analytical equations for the pulse energy and peak power, they do not account directly for thermalization between the stark levels of the upper and lower lasing energy levels. Instead, these models make use of an “inversion reduction factor” to account for the effects of thermalization. This approach works well when the pulse duration is long compared to the thermalization time of the laser crystal. However, when the pulse length and thermalization time are comparable the value of the inversion reduction becomes dependent on the pulse length.

The unidirectional power within the cavity can then be calculated as:

$$P_{IC} = \frac{h\nu_p \pi r_p^2 \phi c}{2n_{avg}} \tag{53}$$

where n_{avg} is the average refractive index in the laser cavity at the pump wavelength.

Under normal operation, a DPSS laser based on Nd:YAG will have unpolarized emission. This makes the use of Nd:YAG with nonlinear materials such as PPLN less desirable as the nonlinear coefficient is dependent on the polarization of the pump wave. While intracavity elements can be added to polarize the emission, these add an additional source of loss within the cavity reducing the laser performance. Fortunately though, by using the correct crystallographic orientation of Cr:YAG it is possible to achieve linear polarization without reducing the output power [37], [38]. This can be explained as follows: the transmission of [100]-cut Cr:YAG is identical along both the [001] and [010] axis which results in the generated pulse consisting of both polarizations. For [110]-cut Cr:YAG the transmission is highest for only polarization along the [100] axis, which results in generated pulses being linearly polarized.

2.6.3.1 Effect of Thermalization

Each energy level in a laser crystal is comprised of some number of a number of closely spaced energy levels, known as stark sublevels. Since the laser transition occurs between specific stark levels in the upper and lower laser energy level, it is important to properly consider the population distribution of the Stark levels. The population of each stark level, when at thermal equilibrium, is governed by the Boltzmann distribution. The population of an individual Stark level is given by:

$$N_i = N \frac{\exp\left(-\frac{\varepsilon_i}{KT}\right)}{\sum_{j=1}^{M} \exp\left(-\frac{\varepsilon_j}{KT}\right)} \tag{54}$$

where N_i is the population of the i'th Stark level, N is the total population of the M Stark levels, ϵ_i is the energy of the i'th Stark level, K is the Boltzmann constant, and T is the temperature in Kelvin.

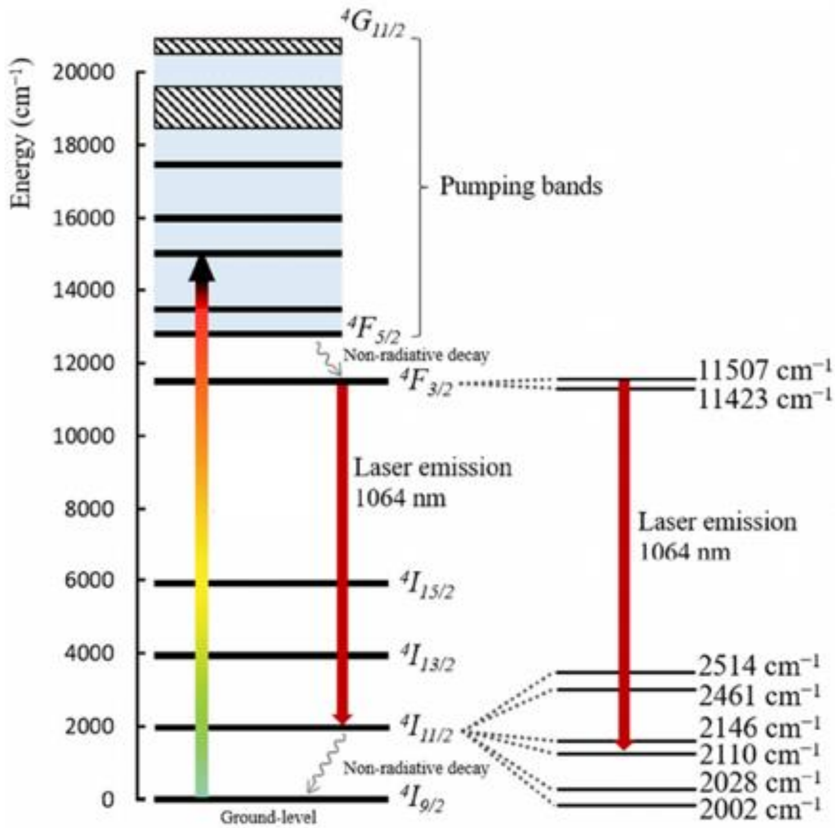

Figure 2-8: Energy level diagram of Nd:YAG adapted from [39]

The process of thermalization drives the population of the upper and lower laser level to their thermal equilibrium values. Thermalization is due to single phonon assisted transitions between the Stark levels [35]. In CW lasers, in pulsed lasers where the pulse duration is much longer than the thermalization time ($t_{pulse} \gg \tau_{therm}$), the thermalization process can be approximated as instantaneous. However, when the pulse length is comparable to the thermalization time, the nonzero thermalization time must be considered.

Thermalization affects laser performance of pulsed lasers in two main ways. The first is by depopulating the lower laser level, and the second is by refreshing the upper laser state. When stimulated emission occurs the lower laser stark level population will increase rapidly from its thermal equilibrium value. Thermalization will result in the depopulation of the Stark level, as population distribution tends to go towards that given by Eq. (54). As a result, thermalization works to improve the population inversion by decreasing the population of the lower laser energy Stark level. Additionally, a similar process happens for the upper laser energy Stark level, where stimulation emission results in the population being decreased below the thermal equilibrium value. Thermalization results in the refreshment of the upper laser energy Stark level as the total population tends towards thermal equilibrium. From this it is clear that as the pulse duration becomes closer and closer to the thermalization time, the effect of thermalization on increasing the population inversion is decreased.

2.6.4 Passively Q-Switched IC-OPOs

The coupling of the time dependent rate equations with the rate equations for a passively Q-switched DPSS laser is similar to the CW setup. The intracavity power calculated with the rate equations is used as the pump input to the time dependent coupled wave equations, resulting in a nonlinear loss which can be calculated and added back into the rate equations. However, unlike the CW case, the laser will not reach steady state operation and as a result the nonlinear loss must be calculated at each time step and used to calculate the input pump power at the next time step. This requires a modification of the rate equation for the intracavity photon flux, Eq. (47), to include a nonlinear loss term. Including the necessary nonlinear loss term gives:

$$\frac{d\phi}{dt} = \frac{\phi}{t_r}\left(2\sigma_e(n_a - n_b)l_g - 2\sigma_{13}n_{s1}l_{Cr} - 2\sigma_{24}\left(n_s - n_{s1}\right)l_{Cr} - L - \ln\left(R\right)\right) - \frac{\phi_{NL}}{t_r} \quad (55)$$

where ϕ_{NL} is the photon density lost due to the nonlinear conversion process and can be calculated as:

$$\phi_{NL} = \frac{n_{avg}P_i}{h\nu_i \pi r_{NL}^2 c} \quad (56)$$

where r_{NL} is the radius of the pump beam within the nonlinear crystal, and P_i is the power of the idler wave in the nonlinear crystal.

2.7 Simulation Methods for IC-OPOs

Due to both the pump and signal wave being resonant within an IC-OPO, there exists both a forwards and backwards component to each field. As such both directions need to be considered when modeling the device. The easiest method to do this is to use two sets of the coupled wave equations, one set for the forward travelling waves and one set for the backward travelling waves [31], [40]. Due to the phase matching condition, only certain groups of waves can interact with each other. In the case of an IC-OPO only the signal, idler and pump which all propagate in the same direction can interact as only this interaction will satisfy the phase matching condition. In an IC-BOPO, two of the forwards travelling waves, the signal and pump, will interact with one backward travelling wave, the idler, and vice versa. When one of the resonant waves reaches the end of the nonlinear crystal, the wave is reflected by the mirror. To model this, the output from the final node of the field in the direction of travel is then used as the input to the first node in the opposite direction of travel.

To improve the efficiency of the model, the substitution $A_j = \sqrt{n_j / \omega_j} E_j$ can be used in the coupled wave equations to allow for a single coupling factor, κ, where κ is equal to:

$$\kappa = \frac{d_{PPLN}^{(2)}}{2c} \sqrt{\frac{\omega_s \omega_i \omega_p}{n_s n_i n_p}} \tag{57}$$

This single term can be substituted into the coupled wave equations to give:

$$\frac{dA_p}{dz} = +\mathrm{i}\kappa \, \mathrm{P}(z) A_i A_s \exp(\mathrm{i}\Delta kz) - \frac{\alpha_p}{2} A_p \tag{58}$$

$$\frac{dA_s}{dz} = +\mathrm{i}\kappa \, \mathrm{P}(z) A_p A_i^* \exp(\mathrm{i}\Delta kz) - \frac{\alpha_s}{2} A_s \tag{59}$$

$$\frac{dA_i}{dz} = +\mathrm{i}\kappa \, \mathrm{P}(z) A_p A_s^* \exp(\mathrm{i}\Delta kz) - \frac{\alpha_i}{2} A_i \tag{60}$$

where α_j is the material loss and has been added into the equations to account for loss as the field propagates through the nonlinear material. P(z) is a function used to account for the effect of periodic poling and takes a value of ±1. A similar set of equations can also be found for a BOPO or for the time dependent coupled wave equations.

The time dependent coupled wave equations can be solved using any first order partial differential equation (PDE) numerical solving method, such as the Lax-Wendroff method [41]. The rate equations for a passively Q-switched DPSS laser can be solved with a 4^{th} or 5^{th} order Runge Kutta method. When simulating multiple pulses, it is ideal to use an adaptive step size algorithm to improve the computational efficiency. During the time between pulses a coarse step size can be used, drastically decreasing the simulation time as the pulse length is generally much shorter than the time between pulses. This becomes especially important when pulses widths are on the order of ns, requiring a time step of 100's of ps. Additionally, since during the time between pulses it is assumed that there is no output from the laser crystal, it is not necessary to solved the coupled wave equations further decreasing the simulation runtime.

3 Theoretical Study of Diode Pumped Intracavity Backwards Optical Parametric Oscillator Based on Quasi-Phase Matched Nonlinear Crystal

*This chapter is reproduced from a journal article **J. Kneller**, L. Flannigan, and C.-Q. Xu, "Theoretical study of diode pumped intracavity backward optical parametric oscillator based on periodically poled lithium niobate," Appl. Phys. B, vol. 129, no. 6, p. 99, 2023, doi: 10.1007/s00340-023-08045-4. Reproduced with permission from Springer Nature*
The author is the first author and main contributor of this publication,

3.1 Preface

The purpose of this research was to develop a new model for an IC-BOPO and to demonstrate that CW operation can be achieved using the intracavity design. Placing the nonlinear crystal within the pump cavity increases the pumping intensity incident on the crystal reducing the input power needed to reach the threshold of the nonlinear interaction. Additionally, confining the signal wave from the BOPO process within a cavity further reduces the pumping intensity needed to reach the device threshold. By employing this design, we showed that it was possible to achieve CW operation using PPLN with 5th order QPM as the nonlinear crystal. The threshold of the proposed laser was found to be less than 10 W. The laser was also capable of achieving 100's of mW of mid-IR emission.

This paper was coauthored with Liam Flannigan who helped with simulation methodologies as well as helped to edit the manuscript. This research article has been published in the Journal of Applied Physics B.

3.2 Abstract

Mid-infrared (mid-IR) lasers with narrow linewidth and high optical output power are in strong demand for remote greenhouse gas (GHG) detection and monitoring. In this paper, a diode pumped mid-IR laser based on an intracavity backwards optical parametric oscillator (IC-BOPO) is proposed and a simulation model is established. The model takes into account light emission from a laser crystal (e.g. $Nd:YVO_4$), an IC-BOPO from a periodically poled nonlinear crystal (e.g. periodically poled lithium niobate (PPLN)), linear loss resulting from optical components and nonlinear loss due to the pump depletion in the BOPO process. It is shown that the proposed mid-IR laser is capable of generating mid-IR light, ranging from 1 μm to 4.5 μm, by employing PPLN with a period ranging from 0.5 μm to 1 μm. It is found that a mid-IR laser with an output power as high as 3 W and a 2 pm linewidth can be achieved by using a 20 W 808 nm pump laser diode and a 4 cm-long PPLN crystal.

3.3 Introduction

Atmospheric greenhouse gas (GHG) detection and monitoring has become increasingly important in recent years due to ever growing concerns with climate change and the resulting run-away feedback loops when certain GHG concentration milestones are reached [1]. A significant body of work details the thresholds for these “points-of-no-return” for the Earth’s climate [1]. As a result, real time, accurate measurement of atmospheric GHG concentrations is needed. Optical techniques, such as light detection and ranging (LiDAR), are well suited for gas monitoring due to the presence of strong absorption lines, which can be used as a fingerprint to identify GHG gasses and their concentrations in the atmosphere provided the laser source has an emission spectrum which matches with an absorption peak of the gas in gas detection, but at the cost of insufficient output power, also making them unacceptable [12]. question [2-5]. Optical detection methods such as differential absorption LiDAR (DIAL) or integrated path differential absorption (IPDA) are attractive optical methods for atmospheric gas monitoring due to the possibility for space-borne monitoring [4,5]. These methods have the benefit of being able to provide real time data for atmospheric gas concentrations around the globe on a weekly basis, allowing for monitoring in remote locations where placing a physical device would be impractical [4].

Laser sources capable of providing narrow emission linewidth and high output power with compact size and low power consumption are required in the aforementioned GHG detection methods [3-7]. Theoretical studies have been completed, determining that approximately watt level output is required for continuous wave sources to be used in these techniques for daytime detection [4-7]. Furthermore, the absorption lines of the gasses of interest are narrow, generally having a full width half maximum (FWHM) on the order of picometers. As such, laser sources with linewidths that are narrower than the absorption lines are required [8]. Additionally, in order for the laser to be integrated into a satellite, low power consumption, room temperature operation, compact size, and robustness are required. A variety of lasers capable of

GHG detection have been developed in the near infrared (NIR [0.8-1.7 micron]) wavelength range and have been used to demonstrate LiDAR based gas detection [5]. However, many of the important GHGs such as methane and nitrous oxide have their fundamental absorption peaks in the mid infrared (mid-IR) wavelength range, while the NIR absorption peaks are much weaker [2]. Due to lack of mid-IR laser sources that can achieve high power and narrow linewidth emission, sources emitting in the suboptimal NIR have been used instead, limiting the sensitivity of the GHG gas sensors [8]. In order to achieve the highest performance possible, high output power, narrow emission linewidth mid-IR lasers with compact size and low power consumption are required [9,10]. Fig. 3.1 shows the absorption cross section of various GHGs at the standard pressure taken from the HITRAN database. As shown in Fig.3.1, the absorption cross sections of the relevant GHGs are 2-3 orders of magnitude higher in the mid infrared region than those in NIR region, clearly demonstrating the need for high quality mid-IR laser sources to achieve high measurement accuracy.

Currently, Quantum and Interband cascade lasers (QCLs & ICLs) are the most commercially mature laser sources emitting in the mid-infrared wavelength range. Recent developments have allowed for watt-level, room temperature operation, greatly reducing the cost of operation [11]. However, achieving both high output powers and narrow emission linewidths simultaneously remains challenging with QCLs and ICLs. For example, high power CW QCLs have been demonstrated with linewidths of approximately 0.5 - 1 nm at 3.8 μm but this linewidth remains too broad for use in gas detection [11]. Other QCLs have demonstrated narrow enough linewidths for use in gas detection, but at the cost of insufficient output power, also making them unacceptable [12].

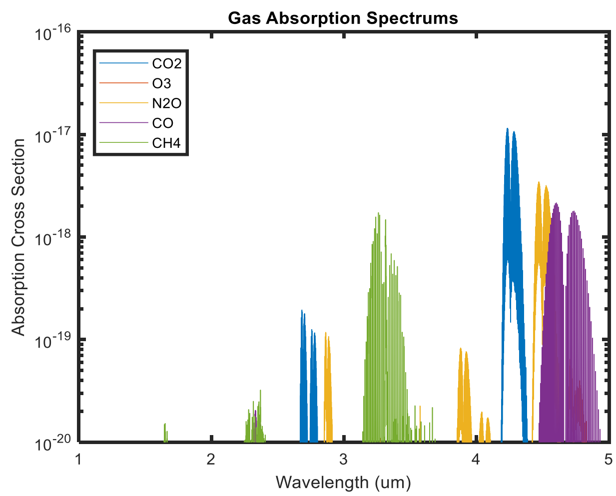

Figure 3.1: Absorption cross section of various GHGs, data taken from HITRAN Database

Mid-IR lasers based on nonlinear optical processes are a promising alternate method to achieve mid-IR emission. Through the use of periodic poling, materials that exhibit a large second order nonlinear coefficient, such as lithium niobate (LN), can be used to achieve high conversion efficiencies. Optical parametric oscillator (OPO) has been used to achieve high output power in the mid-IR wavelength range. For example, singly resonant intracavity (SR IC) OPO has been reported to achieve watt level output in the mid-IR [15]. However, due to the large phase matching bandwidth, OPO has broad emission linewidths [13-15], which is not suitable for GHG detection.

Backwards optical parametric oscillators (BOPO) are also capable of generating high power mid-IR light. BOPOs have attracted significant interest since they can generate narrow linewidth mid-IR light, which potentially avoids some of the pitfalls of forward OPOs [16-17]. As the name implies, in a BOPO, one of the two generated waves counter propagates relative to the pump and the other generated wave [16]. As a result of the backwards travelling wave, effective oscillation can occur within the nonlinear crystal without the need for external mirrors, greatly simplifying the laser structure [16]. Furthermore, the emission linewidths of the generated waves are narrow, within the pm range [17]. However, due to the backwards travelling wave, there is a large momentum mismatch which requires small poling periods on the order of sub-micron, in order to satisfy the quasi-phase matching (QPM) condition [16-18]. Only recently have BOPO been demonstrated in periodically poled KTP (PPKTP) due to the small poling period required [17]. Additionally, only pulsed operation has been achieved due to the high intensities required as a result of the low nonlinear coefficient of PPKTP.

Periodically poled lithium niobate (PPLN) is an attractive nonlinear material due to its high nonlinear coefficient (27 pm/V) [19] and low material loss [20], allowing for the threshold of parametric nonlinear processes to be reached with lower intensity light sources. Recently, sub micron poling periods have been achieved in PPLN [21] leading to the potential for the use of PPLN in BOPO devices. Due to the high nonlinear coefficient, the use of PPLN in BOPO devices can lead to the possibility of continuous wave (CW) operation with reasonable pumping sources. Within this paper we propose the design and simulate the performance of a CW BOPO based on PPLN and show that not only can CW operation be achieved but watt level output in the mid-IR is obtainable with reasonable pump powers by employing an intra-cavity configuration.

3.4 Theory

Fig. 3.2 shows a diagram of the proposed IC-BOPO structure. The pump laser is a 20 W 808 nm laser diode which is used to pump a Nd:YVO_4 crystal to achieve 1064 nm light emission (l_p). The input facet (left hand side) of the Nd:YVO_4 has a high reflection (HR) coating at 1064 nm and an anti-reflection (AR) coating at 808 nm while the output facet (right hand side) has an AR coating at 1064 nm. The nonlinear crystal used is PPLN, with the input facet (left hand side) having an AR coating at 1064 nm and the output facet (right hand side) having an HR coating at 1064 nm. The l_p light is confined within a laser cavity formed by the HR coatings at the input facet of Nd:YVO_4 and the output facet of the PPLN crystal. A dichroic mirror is placed between the Nd:YVO_4 crystal and the PPLN crystal to extract the counter propagating idler wave (l_i) from the laser cavity, and has an AR coating at 1064 nm and an HR coating at the idler wavelength. The signal wave (l_s) comes out from the output facet of the PPLN.

PPLN was chosen as the nonlinear crystal due to its high nonlinear coefficient of 27 pm/V, low material loss and large wafer size (up to 4”). Comparing to PPKTP, which has a nonlinear coefficient of 14.6 pm/V [22], it is clear that PPLN provides a significant advantage. A focusing lens is placed between the pump laser diode and the Nd:YVO_4 crystal to tightly focus the pump beam, guaranteeing a small beam diameter of the 1064 nm light within the PPLN. To achieve single frequency operation of the 1064 nm laser an intracavity etalon was included. This will ensure that the 1064 nm spectrum closely resembles a delta function and as a result both the signal and idler emission spectrums will be narrow enough to be used in gas detection. To ensure that thermal fracture is not an issue in the Nd:YVO_4 crystal, a dopant concentration of 0.5 at% was assumed, allowing for absorbed pump powers of up to at least 23.5 W without causing thermal fracture [23].

There are several features in the proposed structure. First, the BOPO pump light is confined within the cavity created by the two HR coatings shown in blue in Fig. 3.2. By confining the 1064 nm light within the cavity, the circulating power is able to reach the threshold even with a watt level 808 nm pumping and achieve continuous wave (CW) output at the generated wavelengths. Second, the proposed structure, along with the small PPLN period, remove the need for mirrors to be included in the laser structure to achieve CW operation. Third, room temperature operation is achievable as none of the components require extensive cooling to operate and the QPM condition for the nonlinear interaction can be satisfied at room temperature. Last, the intracavity structure allows for the threshold for the nonlinear interaction to be reached with a mature, efficient, semiconductor pump laser diode (LD) at 808 nm, thus the proposed design will have a low power consumption, making it ideal for applications where power consumption is a concern.

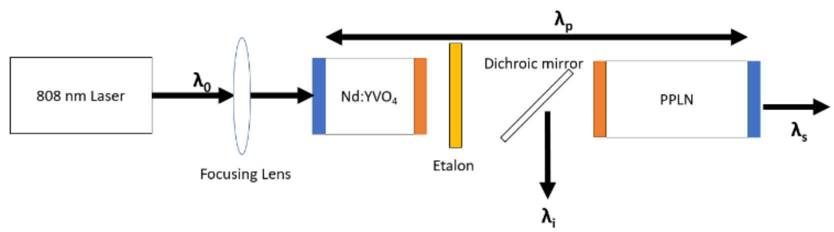

Figure 3.2: Schematic diagram of the prosed IC-BOPO structure. Blue is HR coating at 1064 nm, orange is AR coating at 1064 nm and yellow is the intracavity etalon

We start the analysis of the laser structure shown in Fig. 3.2 by assuming that the pump, signal and idler waves are all plane waves. It is assumed that the forward propagating pump and signal waves travel in the +z direction while the backwards or counterpropagating idler wave travels in the -z direction. The first order coupled wave equations are given by [24]

$$\frac{dA_s}{dz} = +\mathrm{i}\kappa\,\mathrm{P}(z)A_pA_i^*\exp(\mathrm{i}\Delta kz) - \frac{\alpha_s}{2}A_s \tag{61}$$

$$-\frac{dA_i}{dz} = +\mathrm{i}\kappa\,\mathrm{P}(z)A_pA_s^*\exp(\mathrm{i}\Delta kz) - \frac{\alpha_i}{2}A_i \tag{62}$$

$$\frac{dA_p}{dz} = +\mathrm{i}\kappa\,\mathrm{P}(z)A_iA_s\exp(\mathrm{i}\Delta kz) - \frac{\alpha_p}{2}A_p \tag{63}$$

where A_s, A_i and A_p are the slowly varying signal, idler and pump amplitudes, respectively. The substitution $A = \sqrt{n/\omega}E$ was made to enable to the use a single coupling constant *κ*, where

$$\kappa = \frac{d_{PPLN}^{(2)}}{2c}\sqrt{\frac{\omega_s\omega_i\omega_p}{n_s n_i n_p}} \tag{64}$$

where d_{PPLN} is the second order nonlinear coefficient d_{33} of PPLN, c is the vacuum speed of light, ω is the angular frequency of the respective wave and n is the refractive index of the respective wave in PPLN. Δk is the momentum mismatch given by $\Delta k = k_p - k_s + k_i$. P(z) is a function used to account for the sublattice inversion in the crystal and takes a value of either +1 or -1, depending on if the region has a positive or negative nonlinear coefficient. α_s, α_i, α_p are the material loss values for PPLN at the signal, idler and pump wavelengths, respectively.

As is evident from the above equations, only having an initial value for the pump field will result in no output for the signal and idler fields. We followed a similar treatment to other authors and attribute the initial signal and idler field values to the flux of a single photon with energy equal to $\hbar\omega/2$ [24-26]. The factor ½ results from the lowest possible energy of a quantum harmonic oscillator. Following this, and making the same substitution for the electric field as above, the initial field value for the signal wave is:

$$A_s(0,t) = \sqrt{\frac{\hbar}{w_0^2 L\pi\varepsilon_0}} \tag{65}$$

while for the idler the initial value is:

$$\mathrm{A_i}(L,t) = \sqrt{\frac{\hbar}{w_0^2 L \pi \varepsilon_0}} \tag{66}$$

where L is the PPLN crystal length and w_0 is the beam radius.

The simulation was broken into two steps, which were repeated until the returned output value from subsequent runs of the simulation was the same. The first step was the calculation of the circulating 1064 nm power using a previously reported model [27]. The calculated 1064 nm power was used as the initial value for A_p in the coupled wave equations, which were then solved using a Lax-Wendroff method to determine the output power of the signal and idler waves [28].

To properly model the intracavity behavior, the loss of 1064 nm power due to the nonlinear conversion process (a_{nl}) was considered in addition to the linear losses resulting from material loss (a_{PPLN}) and facet reflection of components involved in the cavity (a_{cav}). The calculated signal and idler output powers, along with the intracavity 1064 nm power, were used to calculate the nonlinear loss term. The nonlinear loss term was calculated using the equation:

$$\alpha_{nl} = \frac{N_s}{N_p} \tag{67}$$

where α_{nl} is the nonlinear loss term, N_s is the number of signal photons and N_p is the number of pump photons. Since the number of signal and idler photons generated should be the same, due to the conservation of energy, Eq.(7) can be calculated using either the number of signal or idler photons. With the inclusion of the above nonlinear loss term, the total loss at 1064 nm can be calculated as:

$$\alpha_{tot} = \alpha_{cav} + \alpha_{PPLN} + \alpha_{nl} \tag{68}$$

where α_{tot} is the total loss, α_{cav} the cavity loss, α_{PPLN} the loss in PPLN. By adding in the nonlinear loss term to the existing loss value, the circulating 1064 nm power will be reduced. Note that the loss coefficient α_{PPLN} includes both the material absorption loss and the scattering loss in PPLN. The new value of the 1064 nm circulating power which was calculated by including the nonlinear loss term was then used as the input to the coupled wave equations, resulting in new signal and idler powers, and a new nonlinear loss term. This process was repeated until all output values converged, at which point the steady state signal, idler and intracavity pump powers were found.

To increase the speed at which the coupled wave equations can be solved, an effective nonlinear coefficient was calculated by integrating the domain function, P(z), the phase mismatch term, $\exp[-i\Delta kz]$ and the nonlinear coefficient across the entire length of the crystal and then dividing this value by the length of the crystal. This allows for a step size to be used that is much larger than a single period, greatly decreasing the calculation time. The period size was determined based on the desired signal output wavelength.

Two different types of boundary conditions are needed to solve the coupled wave equations, input and output boundary conditions. The input conditions for the signal and pump fields are the respective field values at the left-hand side (z=0) of the nonlinear crystal, while the input value for the idler is the idler field value at the right-hand side (z=L), of the nonlinear crystal. Since the numerical scheme of the Lax-Wendroff method requires knowledge of the spatial value of node N+1 to evaluate the field at node N, a polynomial interpolation was used to calculate the output boundary conditions, which occur at the right-hand side of the crystal for the signal and pump wave and at the left-hand side of the crystal for the idler wave [29].

The coupled wave equation solution method was validated by comparing the results to previously reported simulation results for a pulsed BOPO based on PPLN [24], which were found to be in excellent agreement. Furthermore, the simulation model was also used to simulate an IC-OPO and found to match well with previously reported experimental results for output power [15].

3.5 Discussion

Fig 3.3 shows the plot of the output wavelengths of the signal and idler wave vs the period of the PPLN crystal based on the phase mismatching in the BOPO process. The refractive index of LN at the three wavelengths was calculated using an appropriate Sellmeier equation at a temperature of 20°C [30]. As shown in Fig. 3, the generated signal wavelength (orange curve) decreases from 2.128 mm to 1.5 mm with the increase of PPLN period, while the generated idler wavelength (blue curve) increases from 2.128 mm to 4.5 mm when PPLN period increases from 0.5 mm to 1 mm. Different from the well-known horseshoe shaped signal/idler wavelength – period curve for an OPO, there exists a sudden turning point in the signal/idler wavelength – period curve for BOPO at the degeneracy point. The wave which counter propagates has a negative wavevector, compared to the wave which co-propagates with the pump wave, as can be seen in the phase matching equation. Due to this negative sign, the change in momentum mismatch when varying the wavelength of the two waves is substantially different, even at the degeneracy point, which leads to two completely different wavelength curves when plotted against the period. In the signal/idler wavelength – period curve of an OPO, the curve of the signal and idler are nearly mirror images of each other at the degeneracy point which is to be expected due to their wavevectors having the same sign. This results in a smooth curve, as opposed to the observed acute angle at the degeneracy point in Fig. 3.3.

As shown in Fig. 3.3, it is necessary to use a sub μm period for 1.5 – 4.5 mm light generation in a PPLN based BOPO. As stated previously, this is a difficult requirement to satisfy with conventional nonlinear materials, but with recent advances in PPLN poling resulting in the fabrication of sub-micron domain periods, as low as 300 nm [21], this condition will likely be able to be satisfied over the entire length of the proposed 4 cm crystal with a high accuracy.

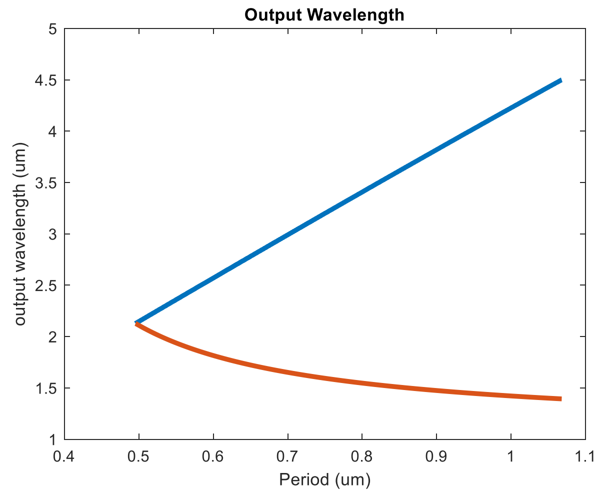

Figure 3.3: Simulated output wavelength of the signal (orange curve) & idler (blue curve) vs the PPLN poling period.

Fig. 3.4 shows simulated signal and idler output power vs the input 808 nm LD power. In the simulations, 100% output coupling of the signal wave from the laser cavity was assumed. Since the signal beam is not confined within a cavity, this assumption does not change the output power by a noticeable amount if the actual output coupling efficiency is slightly less than 100%. The duty cycle of the domain inversion was assumed to be 50/50, with a uniform period of 0.751 µm. The beam waists of the three waves were assumed to be equal and constant throughout the entire length of the nonlinear crystal. The length of the PPLN crystal in the simulation was 4 cm. An overall laser cavity length of 8.5 cm was used in the intracavity simulation, resulting from the 4 cm PPLN crystal, a 0.7 cm Nd:YVO_4 crystal, and a 4 cm space between the PPLN and Nd:YVO_4 crystals where the etalon and dichroic mirror were placed. Different cavity loss values were assumed for the pump beam, which accounts for the loss due to coatings and the intracavity etalon (the loss due to the PPLN crystal is considered separately). The lowest cavity loss value, 0.5%, represents a highly optimized cavity and the maximum performance that would likely be achievable with such a laser. Additional cavity loss values of 1.5% and 2.5% were also simulated to represent more realistic cavity values that would not require the same level of optimization to achieve and be more representative of real device performance. The loss due to the etalon was calculated to be at most 0.3% [31], and included in the cavity loss value, but theoretically could be lower if it is highly optimized and precisely aligned. The signal, idler and pump wavelengths used in the simulation were 1.59 μm, 3.21 μm, and 1.064 μm, respectively. An idler wavelength of 3.21 μm was chosen as this wavelength matches with a known absorption line of methane. The parameters for the Nd:YVO_4 crystal were the same those were used in a previously reported theoretical model for a Nd:YVO_4 laser [32] except the length was set to 0.7 cm and the doping was set to 0.5 at% to prevent thermal fracture. As mentioned above, the simulation models were verified against previously reported experimental results on BOPO [18, 24] and Nd:YVO_4 intracavity lasers [32]. The loss values of the signal, idler and pump in PPLN were assumed to be 0.002 cm^{-1}, 0.07 cm^{-1}, 0.0035 cm^{-1} [20], respectively.

The beam waists of the pump laser diode and the 1064 nm emission in the Nd:YVO_4 crystal were based on experimentally reported values for a similar laser designs. The beam waist of the 808 nm laser was set to 40 μm, while the beam radius of the 1064 nm laser beam (in the Nd:YVO_4 crystal) was set to 60 μm. The beam radius of the 1064 nm laser beam in the PPLN crystal was set to 70 μm to account for the beam expansion. The values were determined using an ABCD matrix method, validated against previous experimental results [33]. The HR coatings at 1064 nm were both assumed to have a reflectivity of 99.9%.

Miller's rule was used to determine the nonlinear coefficient for the wavelengths of interest in the present simulation [34], resulting in a nonlinear coefficient of 22.2 pm/V at the desired wavelengths.

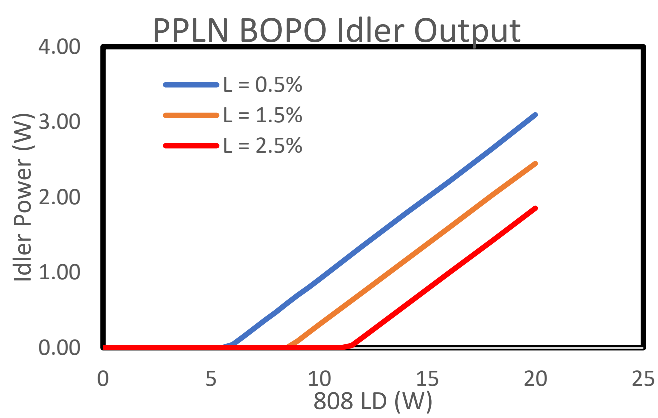

Figure 3.4: Simulated idler output at different cavity loss values

As shown in Fig. 3.4, it is possible to achieve watt level, continuous wave, mid-IR emission with the proposed IC-BOPO structure even when cavity loss is as high as 2.5%. The threshold 808 nm LD powers for the 0.5%, 1.5% and 2.5% cavity loss values were 6 W, 9 W and 11.5 W, respectively. Below the threshold input powers, output powers at the signal and idler wavelengths were negligible, with a rapid rise in output power (several orders of magnitude) occurring near the 808 LD threshold power. The threshold pump power in each loss case corresponds to an intracavity power of approximately 211 W which is in agreement with a previously reported analytical model for the threshold of a BOPO [16]. Furthermore, a clamping of the intracavity power to the threshold value is also observed, which is consistent with previously reported results for IC-OPOs [35], and we expect IC-BOPOs to exhibit the same behaviour. The matching of the both the calculated threshold and the intracavity behaviour with previous results greatly strengthens the validity of the present approach. The maximum idler output power for the 0.5%, 1.5% and 2.5% cavity loss values were 3.1 W, 2.4 W and 1.8 W, respectively. A complete summary of the simulation results for the signal and idler waves at the different cavity loss values are presented in Tables 3.1 & 3.2, respectively.

Table 3.1: Signal output values

	Signal		
	Loss = 0.5%	Loss = 1.5%	Loss = 2.5%
Threshold	6 W	9 W	11.5 W
Max Power	7.2 W	5.7 W	4.3 W
Efficiency	35%	28%	21%
Slope Efficiency	51%	51%	51%

Table 3.2: Idler output values

	Idler		
	Loss = 0.5%	Loss = 0.5%	Loss = 0.5%
Threshold	6 W	9 W	11.5 W
Max Power	3.1 W	2.4 W	1.8 W
Efficiency	15%	12%	9%
Slope Efficiency	22%	22%	22%

In the simulations, only the signal and idler fields generated from the forwards travelling pump wave were calculated. The fields generated from the backwards travelling pump wave were not considered for the following reasons. The intracavity pump power continued to rise as the laser diode power was increased until the threshold power for the BOPO nonlinear interaction was reached. At this point, the 1064 nm intracavity power was effectively clamped. Increasing the laser diode power resulted in a higher nonlinear loss term, which caused the clamping of the intracavity power. Using the nonlinear loss term, we can approximate the backward travelling pump power to be a few percent lower than the forwards travelling pump power. Since the forwards wave is clamped at the threshold value, the backwards travelling wave power was found to be below the threshold of the nonlinear interaction and as such would not generate noticeable BOPO output.

The proposed laser design is capable of satisfying the power requirements for use in LiDAR based atmospheric gas detection in continuous wave operation, while achieving mid-IR output. As shown in Fig. 3.4, the proposed BOPO laser is capable of achieving 3.1 W mid-IR output power with an input power of 20 W from an 808 nm LD when a low loss cavity is used. This satisfies both the output power and low power consumption requirements required for LiDAR based gas detection.

Fig. 3.5 shows the emission spectrum of the signal wave. The x-axis is the deviation from the emission center wavelength, with 0 representing 3.21 μm in the case of the idler, and 1.5 μm in the case of the idler. The plot was generated with an input 808 nm LD power of approximately 20 W and sweeping the wavelength of the signal and idler while maintaining the PPLN period to the value which satisfies the QPM condition for an idler wavelength of 3.21 μm. The predicted FWHM of the signal emission is approximately 2 pm with the 4 cm PPLN crystal, corresponding to a frequency linewidth of 58 MHz. According to the HITRAN data presented in Fig. 1, the FWHM of methane is approximately 300 pm (depending on which absorption line is chosen), indicating the proposed source is more than suitable for use in methane detection. Since the pump spectrum was assumed to be delta function, the emission spectrums of the signal and idler wave were nearly identical, so only the idler spectrum is presented in Fig. 3.5.

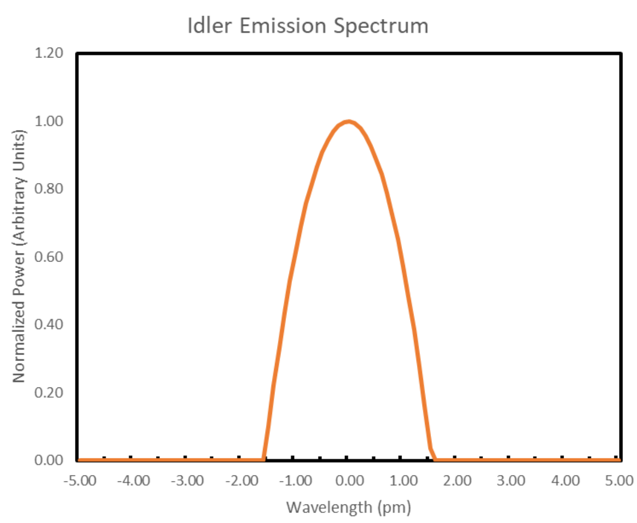

Figure 3.5: Normalized signal emission spectrum for the BOPO device. The x-axis is the deviation from the idlers center emission wavelength of 3.200 μm

The 1064 nm pump was assumed to have a delta function spectrum for the results presented in Fig. 3.5. The reported linewidth of Nd:YVO_4 emission at 1064 nm is approximately 1 nm without the inclusion of a wavelength selective element [36], corresponding to a frequency bandwidth of 265 GHz. A single fused silica etalon with a thickness of 0.1 mm has a free spectral range of approximately 1000 GHz and as such single mode operation should theoretically be achievable with the use of a etalon. The emission linewidth of a single mode Nd:YVO_4 laser has been experimentally shown to be on the order of pm [37], justifying the delta function assumption made in the simulations. Under this assumption the idler spectrum is approximately 2 pm, compared to the 750 pm linewidth of a conventional OPO (including an intracavity etalon) at a similar wavelength [13]. Furthermore, in BOPO devices the bandwidth of the pump is almost entirely transferred to the forward propagating wave [17], which in this case is the signal, resulting in the idler wave having a much narrower spectrum than the pump. Due to this the assumption of the pump having delta function spectrum should be valid and be a true representation of the idler spectrum.

The sinc^2 intensity profile is not observed in Fig. 3.5 due to the exponential increase in power for wavelengths that are able to reach the threshold point. Since only a narrow range of wavelengths are able to reach the oscillation threshold, the power of these wavelengths is several orders of magnitude higher than the wavelengths further from the center of the emission spectrum.

3.6 Conclusions

We have proposed and theoretically studied an intracavity backwards optical parametric oscillator based on PPLN. We have shown theoretically that continuous wave, watt level, mid-IR output is achievable with a low-cost semiconductor pump LD. The maximum output power achievable was 3.1 W at 3.21 μm with 20 W of input pump power and a highly optimized cavity. The proposed laser structure is able to achieve optical to optical conversion efficiency of as high as 15% at 3.21 μm. The output linewidth of the 3.21 μm spectrum is approximately 2 pm (corresponding to a frequency linewidth of 58 MHz).

The output power, linewidth and emission wavelength satisfy all the requirements for a source that is to be used in daytime gas detection through LiDAR methods. The proposed laser structure is capable of achieving emission throughout the entire transparency region of the PPLN crystal through modification of period or by modifying the operation temperature, enabling it to be for detection of different gas species. The proposed laser structure provides a drastic improvement over current technology emitting in the mid-IR wavelengths in terms of cost and output power, while maintaining a comparable emission linewidth. It is expected that the results presented in this paper can provide guidelines in developing mid-IR sources based on PPLN for GHG detection/monitoring.

3.7 Acknowledgements

The authors would like to thank Dr. Daniel Poitras from the NRC for helpful discussion and design of the AR and HR coatings.

3.8 References

[1] J. Randers and U. Goluke, Sci. Rep. **10**, 18456 (2020).
[2] D. Popa and F. Udrea, Sensors **19**, (2019).
[3] L. Joly, V. Zéninari, T. Decarpenterie, J. Cousin, B. Grouiez, D. Mammez, G. Durry, M. Carras, X. Marcadet, and B. Parvitte, Laser Phys. **21**, 805 (2011).
[4] L. Mei and M. Brydegaard, Laser Photon. Rev. **9**, 629 (2015).
[5] G. A. Wagner and D. F. Plusquellic, Appl. Opt. **55**, 6292 (2016).
[6] L. Mei, P. Guan, and Z. Kong, Opt. Express **25**, A953 (2017).
[7] I. Esquivias, A. Consoli, M. Krakowski, M. Faugeron, G. Kochem, M. Traub, J. Barbero, P. Fiadino, X. Ai, J. Rarity, M. Quatrevalet, and G. Ehret, in *Proc.SPIE* (2014).
[8] G. Ehret, C. Kiemle, M. Wirth, A. Amediek, A. Fix, and S. Houweling, Appl. Phys. B **90**, 593 (2008).
[9] S. Yakovlev, S. Sadovnikov, O. Kharchenko, and N. Kravtsova, Atmos. **11**, (2020).
[10] Z. Du, S. Zhang, J. Li, N. Gao, and K. Tong, Appl. Sci. **9**, (2019).
[11] M. Razeghi, SPIE Conf. Proc. **11296**, 112961C (2020).
[12] S. Borri, G. Insero, G. Santambrogio, D. Mazzotti, F. Cappelli, I. Galli, G. Galzerano, M. Marangoni, P. Laporta, V. Di Sarno, L. Santamaria, P. Maddaloni, and P. De Natale, Appl. Phys. B **125**, 18 (2019).
[13] Y. F. Peng, X. B. Wei, G. Xie, J. R. Gao, D. M. Li, and W. M. Wang, Laser Phys. **23**, 55405 (2013).
[14] J. Zhao, P. Cheng, F. Xu, X. Zhou, J. Tang, Y. Liu, and G. Wang, Appl. Sci. **8**, (2018).
[15] K. Wang, M. Gao, S. Yu, J. Ning, Z. Xie, X. Lv, G. Zhao, and S. Zhu, Sci. Rep. **11**, 5079 (2021).
[16] S. E. Harris, Appl. Phys. Lett. **9**, 114 (1966).
[17] C. Canalias and V. Pasiskevicius, Nat. Photonics **1**, 459 (2007).
[18] Y. J. Ding and J. B. Khurgin, IEEE J. Quantum Electron. **32**, 1574 (1996).
[19] R. W. Boyd, "Nonlinear Optics," in Nonlinear Optics (Academic, 2020), p. 80.
[20] 1. M. Leidinger, S. Fieberg, N. Waasem, F. Kühnemann, K. Buse, and I. Breunig, Opt. Express **23**, 21690 (2015).
[21] 1. B. N. Slautin, H. Zhu, and V. Y. Shur, Ferroelectrics **576**, 119 (2021).
[22] 1. I. Shoji, T. Kondo, A. Kitamoto, M. Shirane, and R. Ito, J. Opt. Soc. Am. B **14**, 2268 (1997).
[23] 1. Y.-F. Chen, IEEE J. Quantum Electron. **35**, 234 (1999).
[24] 1. C. E. Minor and R. S. Cudney, Appl. Phys. B **123**, 38 (2017).
[25] 1. G. Rustad, G. Arisholm, and Ø. Farsund, Opt. Express **19**, 2815 (2011).
[26] 1. A. Fix and R. Wallenstein, J. Opt. Soc. Am. B **13**, 2484 (1996).
[27] 1. W. P. Risk, J. Opt. Soc. Am. B **5**, 1412 (1988).
[28] 1. P. Lax and B. Wendroff, Commun. Pure Appl. Math. **13**, 217 (1960).
[29] Z. Du and J. Li, J. Comput. Phys. **369**, 125 (2018).
[30] O. Gayer, Z. Sacks, E. Galun, and A. Arie, Appl. Phys. B **91**, 343 (2008).
[31] W. R. Leeb, Appl. Phys. **6**, 267 (1975).
[32] L. Flannigan, T. Kashak, and C.-Q. Xu, Opt. Express **29**, 6810 (2021).
[33] L. Guillemot, P. Loiko, E. Kifle, J.-L. Doualan, A. Braud, F. Starecki, T. Georges, J. Rouvillain, A. Hideur, and P. Camy, Opt. Mater. (Amst). **101**, 109745 (2020).
[34] R. C. Miller, Appl. Phys. Lett. **5**, 17 (1964).
[35] G. A. Turnbull, M. H. Dunn, and M. Ebrahimzadeh, Appl. Phys. B **66**, 701 (1998).
[36] V. N. Burakevich, V. A. Lisinetskii, A. S. Grabtchikov, A. A. Demidovich, V. A. Orlovich, and V. N. Matrosov, Appl. Phys. B **86**, 511 (2007).
[37] J. Q. Zhao, Y. Z. Wang, B. Q. Yao, and Y. L. Ju, Laser Phys. Lett. **7**, 135 (2010).

4 Design Considerations for Continuous Wave Intracavity Backwards Optical Parametric Oscillators

*This chapter is reproduced from a journal article **J. Kneller**, L. Flannigan, and C.-Q. Xu, "Design Considerations for Continuous Wave Intracavity Backwards Optical Parametric Oscillators," Photonics, vol. 11, no. 4. 2024, doi: 10.3390/photonics11040318.*
The author is the first author and main contributor of this publication,

4.1 Preface

The purpose of this research was to perform a theoretical systematic study on IC-BOPOs to optimize performance and present design guidelines for the proposed laser. In the previous work it was shown that a CW IC-BOPO could be achieved using PPLN with 5th order QPM as a nonlinear crystal. To further improve the performance of the laser a theoretical systematic study was performed on different cavity design elements such as the nonlinear crystal length, cavity length, OC radius, and pump laser spot size in the laser crystal to determine the optimum cavity setup for different performance requirements such as minimizing the pumping threshold or maximizing the output power. A physical explanation for the effect of each cavity variable on the laser performance was also given to provide further understanding into how these parameters affect the laser performance.

This paper was coauthored with Liam Flannigan who helped with simulation methodologies as well as helped to edit the manuscript. This research article has been published in Photonics.

4.2 Abstract

In this paper we report a theoretical systematic study of continuous wave intracavity backwards optical parametric oscillators based on periodically poled lithium niobate (PPLN) for mid-infrared (mid-IR) light generation. We study the effects of varying different cavity parameters including nonlinear crystal length, cavity size, pump laser diode spot size, output coupler radius, and cavity loss values on the output power and threshold of the proposed mid-IR laser. The effects of different physical phenomena are included in the model including pump depletion due to the nonlinear conversion process, the thermal lens effect, and mode overlap between the beams in the nonlinear crystal. We show that high output powers in the mid infrared (> 500 mW at 3.2 μm) can be achieved with proper cavity design and that the laser threshold with a PPLN as short as 2 cm can be reached.

4.3 Introduction

Laser sources based on the parametric oscillation of counterpropagating waves, also known as a backwards optical parametric oscillator (BOPO), are an attractive means to generate high power, narrow linewidth mid-infrared (mid-IR) light emission [1-4]. When compared to a common optical parametric oscillator (OPO), BOPOs exhibit unique advantages including removing the need for external mirrors to confine the generated light and the narrow linewidth counterpropagating wave [1-4]. These traits make BOPOs an ideal source of mid-IR light generation compared to standard OPOs.

Despite these advantages, development of BOPOs has been limited by difficulties in phase matching caused by the counterpropagating wave [1,3]. Due to the counterpropagating wave, the momentum mismatch between the three waves is much larger than in the co-propagating case [1-4]. The most promising method to compensate for this momentum mismatch is the quasi-phase matching (QPM) technique, which periodically inverts the sign of the nonlinear coefficient to satisfy the phase matching condition. However, the large momentum mismatch calls for a sub-micron period with a high-quality duty cycle, which is difficult to achieve in most nonlinear materials. To date, sub-micron poling in bulk materials, with a high-quality duty cycle, has only been demonstrated in periodically poled potassium titanyl phosphate (PPKTP) [2,3]. While achieving sub-micron poling in PPKTP is possible, it has only been demonstrated with short crystal lengths (sub 1 cm), which limits the operation of these BOPO to pulsed mode only [2,3].

One option to overcome the need for a short period is to use higher order QPM, where the period is multiplied by an odd integer [5]. While this does reduce the effective nonlinear coefficient of the material, it removes the need to achieve submicron poling, allowing for the use of materials with higher nonlinear coefficients than KTP such as lithium niobate (LN) as well as the use of longer crystals [5]. Due to the reduced nonlinear coefficient, and hence the reduced conversion efficiency, extensive optimization is needed to ensure that not only can the threshold of the BOPO be reached, but that output powers are high enough to be useful for the desired applications. As such, systematic studies are needed to optimize the laser cavity design. However, due to the prohibitive cost of PPLN, experimental system studies have not been performed. In 2017 a systematic theoretical study on a PPLN BOPO with 5^{th} order QPM in a single pass configuration, aiming to find the optimum pulse parameters to achieve maximum output power was reported [5]. The authors found that it was possible to reach the BOPO threshold with a 700 ps and pulse energy of 70 μJ in a single pass configuration. In 2022 a theoretical study was done on the threshold and linewidth of single pass CW BOPOs but due to the single pass configuration the threshold to reach CW operation is too high even when using 1^{st} order QPM [6]. Another structure which can be used to realize a CW BOPO is an intracavity structure which would reduce the device threshold and allow for operation with a low power pump source. We recently showed it was possible to reach the BOPO threshold for CW operation using 5^{th} order QPM in PPLN with a low pump power [7].

In this paper, we report a systematic study of a CW intracavity BOPO based on 5^{th} order QPM in PPLN to determine the optimum operating configuration. We study the effects of changing various cavity parameters including PPLN length, laser cavity length, pump laser diode power, pump laser diode spot size, output coupler (OC) radius while also accounting for various physical phenomena such as nonlinear loss due to the nonlinear conversion process, the thermal lens effect, and mode overlap between the three waves.

4.4 Theoretical Background and Model

Figure 4.1 shows a diagram of a singly resonant IC-BOPO based mid-IR laser structure. The pump laser is an 808 nm laser diode. In this study, we assume the max output power from the 808 nm LD to be 10 W, which pumps the Nd:YVO_4 crystal to achieve 1064 nm emission. The nonlinear crystal used is PPLN, which is placed inside of the pump cavity. The input facet of the Nd:YVO_4 (coating #1) is high reflection (HR) coated at the BOPO pump wavelength (1064 nm) and high transmission (HT) coated at 808 nm. The output facet of the Nd:YVO_4 crystal (coating #2) is antireflection (AR) coated at the BOPO pump wavelength (1064 nm). The input facet of the PPLN (coating #3) is HR coated at the BOPO signal wavelength (1590 nm) and AR coated at the BOPO pump wavelength 1064 nm. The output facet of the PPLN (coating #4) is AR coated at the BOPO signal, pump and idler (3.2 μm) wavelengths. The optical coupler (OC) is HR coated (coating #5) at both the signal and pump wavelength of BOPO, and AR coated at the BOPO idler wavelength 3210 nm). The pump cavity is formed by coatings #1 and #5. The signal cavity is formed by coatings #3 and #5.

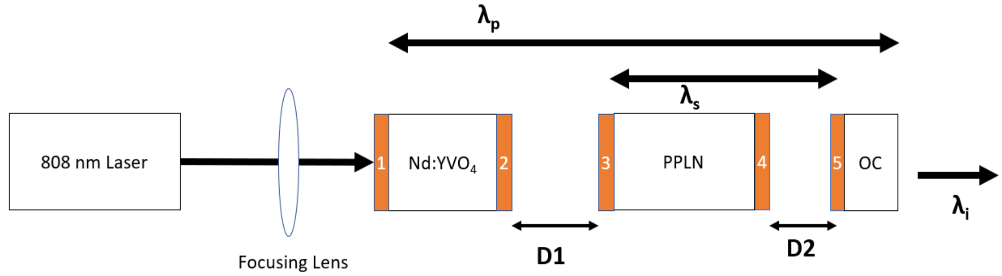

Figure 4.1: Design of proposed mid-IR source. Coatings are shown in orange and numbered.

To analyze the laser depicted in Figure 4.1 we have used a model developed within our group and reported previously [7]. Since the intracavity structure used results in both forwards and backwards propagating waves, forward propagating waves are assumed to travel in the +z direction and backward propagating waves assumed to travel in the -z direction. The first order coupled wave equations for the forward propagating waves can be written as [5]:

$$\frac{dA_s}{dz} = +i\kappa \, \mathrm{P}(z) A_p A_i^* \exp(i\Delta kz)\beta_{pi} - \frac{\alpha_s}{2} A_s \tag{69}$$

$$-\frac{dA_i}{dz} = i\kappa \, \mathrm{P}(z) A_p A_s^* \exp(i\Delta kz)\beta_{ps} - \frac{\alpha_i}{2} A_i \tag{70}$$

$$\frac{dA_p}{dz} = +i\kappa \, \mathrm{P}(z) A_i A_s \exp(i\Delta kz)\beta_{is} - \frac{\alpha_p}{2} A_p \tag{71}$$

where A_s, A_i and A_p are the slowly varying signal, idler and pump amplitudes, respectively. P(z) is a periodic function which models the poling in the LN, taking a value of ±1, depending on if the region has a positive or negative nonlinear coefficient.

Δk is the momentum mismatch given by $\Delta k = k_p - k_s + k_i$. α_s, α_i, α_p are the material loss values for PPLN at the signal, idler and pump wavelengths, respectively. The substitution $A = \sqrt{n/\omega}E$ was made to enable to the use a single coupling constant κ, where:

$$\kappa = \frac{d_{PPLN}^{(2)}}{2c}\sqrt{\frac{\omega_s \omega_i \omega_p}{n_s n_i n_p}} \tag{72}$$

where d_{PPLN} is the second order nonlinear coefficient d_{33} of PPLN, c is the vacuum speed of light, ω is the angular frequency of the respective wave and n is the refractive index of the respective wave in PPLN. Millers rule was used to scale the nonlinear coefficient to the wavelengths used in this study [8]. Additionally, another factor was added to the nonlinear coupling part of Equations (68)-(71), β, which is used to account for the overlap between the respective fields in each coupled wave equation. The term has a value which ranges from 0 – 1, where 0 represents no overlap and 1 represents perfect overlap. Since the plane wave assumption assumes perfect overlap between the fields, this term serves as a correction factor and reduces the efficiency of the nonlinear interaction if the fields spatial overlap is poor, which is used to improve the accuracy of the model. The overlap of two fields, in this case the signal and idler, can be evaluated as:

$$\beta_{is} = \frac{\left|\iint E_s(x,y)\bullet E_i(x,y)dxdy\right|^2}{\iint \left|E_s(x,y)\right|^2 dxdy \bullet \iint \left|E_i(x,y)\right|^2 dxdy} \tag{73}$$

where E_i is the spatial distribution of the idler electric field and E_s is the spatial distribution of the signal electric field. The remaining two overlap parameters can be calculated using the above equation with the corresponding fields. In order to properly evaluate Eq. 73, the spatial distribution of the fields inside of the nonlinear crystal is needed. An ABCD matrix method was used to determine the beam waists of the three fields inside of the cavity.

The initial conditions for the signal and idler wave are determined by calculating the flux of a single photon [5,9,10]. The initial condition for the pump wave can be found by calculating the circulating 1064 nm optical power.

To calculate the circulating 1064 nm optical power, a previously reported model for an intracavity laser was used [11]. The calculated 1064 nm power was then used as the initial condition for the pump field in the coupled wave equations which were then solved using a Lax-Wendroff method [12]. However, due to the inclusion of the nonlinear crystal, an additional loss term, which results from the conversion of the pump beam to the signal and idler in the nonlinear process, must be considered. This nonlinear loss term is added to the linear loss term, which includes material loss due to absorption, reflection of components involved in the cavity, and imperfect mirrors. The nonlinear loss term is the total loss of the 1064 nm beam that occurs from travelling through the nonlinear crystal due to the nonlinear conversion process. This nonlinear loss term can be calculated as:

$$\alpha_{nl} = \frac{N_i}{N_p} \tag{74}$$

where α_{nl} is the nonlinear loss term, N_i is the number of idler photons generated in the forwards and backwards direction and N_p is the number of pump photons incident on the nonlinear crystal. This term can be added to the other loss sources to determine the total loss at the BOPO pump wavelength as:

$$\alpha_{TOT} = \alpha_{cav} + \alpha_{PPLN} + \alpha_{OC} + \alpha_{nl} \tag{75}$$

where α_{tot} is the total loss, α_{cav} the cavity loss, α_{PPLN} the loss in PPLN due to scattering and absorption, and α_{OC} is the loss due to imperfect mirrors. The new value of the 1064 nm circulating power which was calculated by including the nonlinear loss term was then used as the input to the coupled wave equations, resulting in new signal and idler powers, and a new nonlinear loss term. This process was repeated until all output values converged, at which point the steady state signal, idler and intracavity pump powers were found.

In order to properly model the intracavity laser power the thermal lens effect in the $Nd:YVO_4$ crystal must be considered. The thermal lens effect can be modeled as [13]:

$$\frac{1}{f_{th}} = \int_0^l \frac{\zeta P_{abs}}{4\pi \mathrm{K}_c} \frac{\alpha e^{-\alpha z}}{1-e^{-\alpha l}} \frac{dn/dT + n\alpha_T}{\omega_p^2(z)} dz \tag{76}$$

where ζ is the fractional thermal loading, P_{abs} is the absorbed pump power, κ_c is the thermal conductivity, α is the absorption coefficient at the pump wavelength, l is the crystal length, dn/dT is the thermos-optic coefficient, α_T is the thermal expansion coefficient and ω_p is the pump size in the laser crystal. Thermal effects within the PPLN crystal have not been considered due to the low absorption coefficient of PPLN at the wavelengths of interest resulting in negligible heating. Precise temperature control of the PPLN can be achieved with standard methods, such as ovens and thermoelectric coolers, which can maintain temperature control to 0.1°C.

To allow for step sizes greater than the poling period to be used, an effective nonlinear coefficient was calculated by integrating the poling function, P(z), the phase mismatch term, $\exp[-i\Delta kz]$ and the nonlinear coefficient over length of the crystal and then dividing this value by the length of the crystal. The period of the poling function is chosen to equal the momentum mismatch at the desired signal and idler wavelengths.

Due to the intracavity structure used the fields within the cavity must be broken into forwards and backwards components. For the purpose of this paper, we assume forward to refer to fields travelling from left to right (coating #1 to the OC in the context of Figure 4.1) and backwards to refer to fields travelling from right to left (from the OC to coating #1 in the context of Figure 4.1). Since both the pump and signal wave are confined, each will have a forwards and backwards component. Since there are both forwards and backwards travelling signal and pump waves there must also be a forward and backwards travelling idler wave. When considering a BOPO the phase matching convention assumes that the pump and signal wave co-propagate and generate a counterpropagating idler wave, as opposed to a regular IC-OPO where the copropagating pump and signal field will result in a copropagating idler field. This means that the forward travelling signal and pump will generate a backwards travelling idler wave and vice versa in the case of an IC-BOPO.

A list of the parameters used in the simulations is provided in Table 4.1.

Table 4.1: The value of each parameter used in simulation with references where applicable.

Parameter	**Value**	**Reference**
Temperature	293 K	
Mirror Reflectivity (Pump)	99.87%, 99.87%	
Mirror Reflectivity (Signal)	98%, 99.8%	
Wavelength (Pump, Signal, Idler)	1064 nm, 1590 nm, 3210 nm	
Refractive Index PPLN (Pump, Signal, idler)	2.147, 2.128, 2.0811	[15]
$Nd:YVO_4$ Length	7 mm	
$Nd:YVO_4$ refractive index at 1064 nm	2.16	[13]
$Nd:YVO_4$ Thermal Conductivity	0.0523 W m^{-1} K^{-1}	[13]
$Nd:YVO_4$ Thermal Expansion Coefficient	4.43E-6 K^{-1}	[13
$Nd:YVO_4$ Thermo-optic Coefficient	3E-6 K^{-1}	[13]
Fractional Thermal Loading	0.24	[13,16]
Cavity loss (Pump, Signal)	1%, 1%	
OC Radius	100 mm	
PPLN Absorption (Pump, signal idler)	0.0035 cm^{-1}, 0.002 cm^{-1}, 0.07 cm^{-1}	
Cavity Loss (Pump, Signal)	1%, 1%	
808 LD Beam Waist	165 μm	
$d^{(2)}_{PPLN}$	22.3 pm/V	[8, 17]

4.5 Results & Discussion

4.5.1 Dependence on PPLN and Cavity Length

Figure 4.2 shows the idler power for a 5 cm PPLN with various cavity sizes. The power from the 808 nm LD was 10 W, and was focused to a radius of 165 μm in the $Nd:YVO_4$ crystal. The radius of the OC used was 100 mm. The x- and y- axis are the spacing between the $Nd:YVO_4$ crystal and PPLN (D1) and the spacing between the

PPLN and OC (D2), respectively. A number of observations can be made from the data in Figure 4.2. The first observation is that an idler output power of 600 mW is achievable with a 10 W pump source by using the proposed intracavity structure corresponding to an idler conversion efficiency of 6%. This conversion efficiency is comparable to the theoretical report from 2017 [5], however here the device is operated in CW mode instead of pulsed. Second, the idler output power increases slightly with increasing D1 within the range of the simulation (i.e. D1<30 mm), as long as the D2 value is small. Third, the idler output power decreases with increasing D2 for all D1 values. Last, the geometric stability of the cavity shows a greater dependence on the D2 value than the D1 value.

These effects can be explained as follows. Due to the thermal lens effect in the $Nd:YVO_4$ crystal, the shape of the 1064 nm beam waist within the cavity resembles an asymmetric parabola. As a result, it is necessary to place the PPLN in a location within the cavity such that the average beam waist inside of the PPLN is minimized. Increasing D1, while D2 is kept small (< 10 mm), results in the average 1064 beam radius decreasing within the PPLN, resulting in higher conversion efficiencies. The improvement in output power is small though as decreasing the 1064 nm beam in the PPLN also reduces the overlap between the signal and pump as the signal beam size is unaffected by the D1 value. When increasing D2, it was found that the average 1064 nm beam radius always increased, regardless of the D1 value which resulted in the decrease in output power with increasing D2. It was also found that increasing either

D1 or D2 above a certain value, resulted in a rapid increase in the average 1064 nm beam radius in the PPLN leading to a rapid decrease in output power. This rapid decrease in output power occurs as the cavity approaches geometric instability. As can be seen in Figure 4.2, the D1 and D2 values at which this occurs vary depending on the overall cavity size. However, this drop occurs at lower D2 values than D1 values, indicating that the geometric stability of the cavity is affected more by the D2 value than the D1 value.

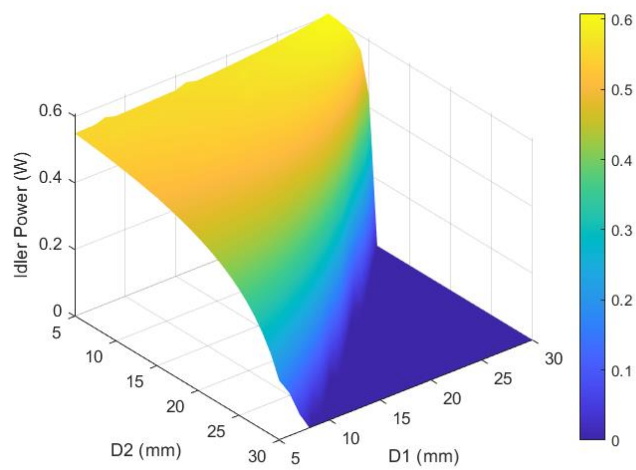

Figure 4.2: Maximum output idler power for different cavity spacings with a 5 cm PPLN

An important point which must be considered is that the optimum cavity setup will largely depend on the focal length of the thermal lens inside the Nd:YVO_4 crystal. Changing the focal length will then affect the optimum D1 and D2 value. As stated earlier, the maximum output power configuration occurs right before a rapid drop in output power if either D1 or D2 is increased further. As such, if the cavity is set up in the optimum configuration, small thermal fluctuations in the Nd:YVO_4 crystal can drastically reduce the output power. However, this can be accounted for in the cavity by using values of D1 and D2 slightly below the optimum values to allow more room for thermal fluctuations.

Based on the above observation two conclusions can be made. First, optimizing the D1 value is important to achieve the highest output power. The output power can be improved by as much as 10% from the most compact cavity configuration (540 mW vs 600 mW) by employing an optimized D1 value. Second, the D2 value should be kept as small as possible so that the cavity remains stable while maximum output power is achieved.

Figure 4.3 shows the threshold of the laser with the same cavity configuration as was used for Figure 4.2. Additionally, the same simulation parameters were used as indicated in Table 4.1. Minimizing the IC-BOPO threshold is necessary to enable the use of a low power pump source. Additionally, due to the use of 5th order QPM the effective nonlinear coefficient is reduced, resulting in the need for increased cavity optimization so the threshold can be reached with a low power source. From Figure 4.3 we can see that the laser threshold is lowest, approximately 5.4 W, when the cavity was in the most compact configuration (D1 = D2 = 5 mm. The threshold was found to increase with increasing D1 and D2 values. The threshold value was also found to be more sensitive to a change in D1 than D2, although the difference was small. The decrease in threshold when the cavity size is reduced is due to the change in the 1064 nm cavity mode. At low input powers, the position of the minimum beam waist is shifted nearer to the Nd:YVO_4 crystal. This results in the 1064 nm beam waist being shifted towards the Nd:YVO_4 crystal due to the larger thermal lens focal length. As a result the PPLN, in order to achieve the smallest average 1064 nm beam waist, must be placed as close to the Nd:YVO_4 crystal as possible.

From Figures 4.2 & 4.3 it is clear that there is a trade-off between achieving high output power and achieving a low threshold. According to Figure 4.2, the maximum idler output power occurs when D1 = 30 mm and D2 = 5 mm, however as previously mentioned the minimum threshold is achieved when D1 = D2 = 5 mm. As such increasing the maximum power would also result in an increased threshold and vice versa.

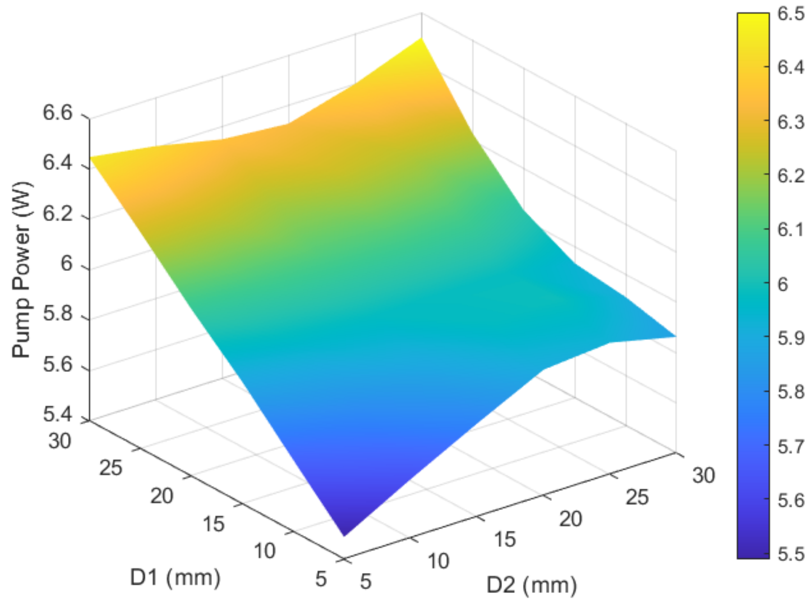

Figure 4.3: Threshold for a 5 cm PPLN at various cavity spacings

Figure 4.4 shows the variation in idler output power with a 10 W pump, for different PPLN sizes when D1 and D2 value are kept constant. Both D1 and D2 were set to 5 mm for all PPLN lengths. D1 and D2 were set to 5 mm for all crystal lengths to ensure that the cavity remained geometrically stable for all crystal lengths at all input powers. Figure 4.4 shows an increased maximum idler power for longer crystals; with a significant increase output power occurring from increasing the length from 3 cm to 4 cm (300 mW to 460 mW), while the increase in output power due to using a 5 cm PPLN instead of 4 cm is not as substantial (460 mW to 540 mW).

Figure 4.4 suggests that there are diminishing returns when increasing the PPLN length in terms of the maximum achievable output idler power. As previously mentioned, increasing the PPLN length from 3 to 4 cm, resulted in an increased output power of roughly 50% while the PPLN length was increased by only 30%. Comparing this to the 20% increase in output power when increasing the PPLN length from 4 cm to 5 cm, it is clear that increasing the PPLN length does not have linear effect on output power. This can be explained as follows: while the conversion efficiency is dependent on the length of the PPLN, increasing the PPLN length also increases the size of all three beams within the cavity reducing the intensity. Additionally, as the conversion efficiency increases with increased PPLN length so does the nonlinear loss term present in Eq. 75, which reduces the intracavity 1064 nm power. The diminishing returns in output power when increasing PPLN length is important to consider as a longer PPLN will increase the device footprint as well as increase the cost. Furthermore, maintaining a high-quality duty cycle over a longer crystal is an additional challenge which could further reduce device performance.

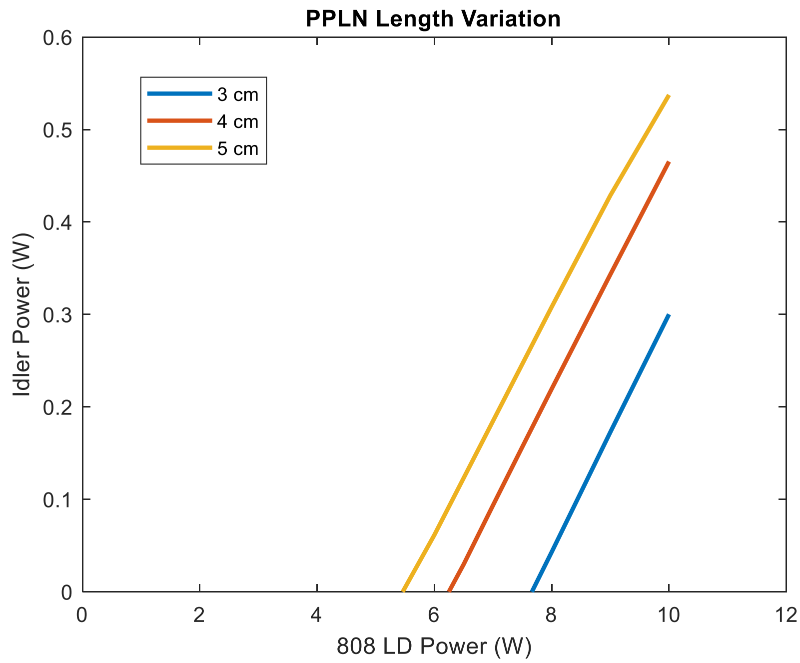

Figure 4.4: Output power for different PPLN lengths with a constant cavity size.

4.5.2 Dependence on 808 nm LD Laser Beam Waist

Figure 4.5 shows the beam radius of the 1064 nm beam in the PPLN crystal for various D1 values and various 808 nm beam spot sizes. For all data points shown in Figure 4.5, D2 was set to 5 mm and the PPLN length was 5 cm. From Figure 4.5 two observations can be made. The first is the importance of choosing an optimum 808 nm beam waist to achieve the minimum 1064 nm beam radius in the PPLN crystal for a given cavity configuration. The second is that the smaller the 808 nm beam waist, the smaller the cavity must be to remain geometrically stable.

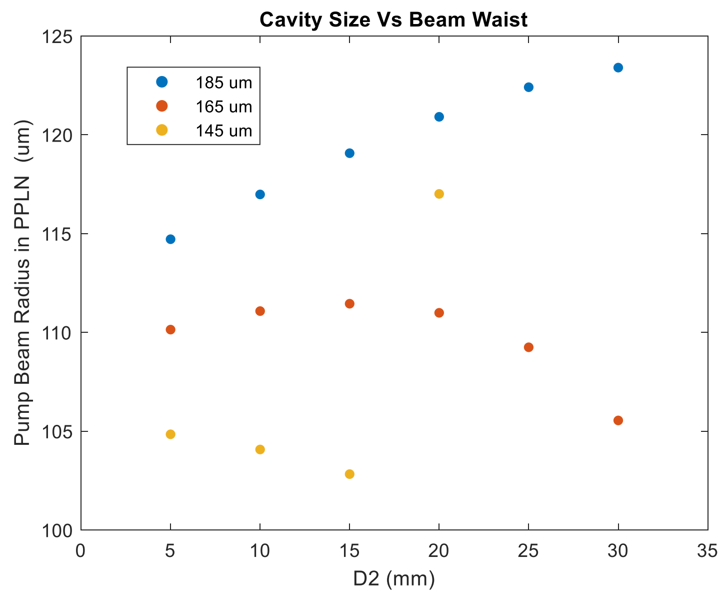

Figure 4.5: Pump beam radius for a 5 cm PPLN at different D1 values and input LD beam waists.

From Figure 4.5, it is clear that there exists an optimum 808 nm beam waist at which the 1064 nm beam will have a minimum radius within the PPLN. As can be seen by the result in Figure 4.5, this optimum beam waist depends on the spatial configuration of the cavity. For the 145 μm 808 nm LD beam waist, we see that the minimum PPLN beam waist is achieved at a D1 value of approximately 15 mm. The change in beam waist was small when decreasing D1 below 15 mm, reaching a value of approximately 105 μm at a D1 value of 5 mm. However, the rate of change in the beam waist was rapid when increasing D1 past 15 mm, with the cavity becoming geometrically unstable at D1 values larger than 20 mm. Choosing the correct D1 value ensures that the 1064 intracavity beam waist is approximately in the center of the PPLN, minimizing the average beam waist in the PPLN. For the other 808 nm beam waists, a similar trend was observed, although not as pronounced as the 145 μm case. This result is due to the thermal lens focal length being dependent on the 808 nm beam waist, with a smaller beam waist producing a smaller focal length and hence a greater focusing power. As a consequence of smaller 808 nm beam waists producing a thermal lens with a smaller focal length, the maximum cavity size must be limited in order to ensure it remains geometrically stable.

This shows the importance of achieving excellent thermal stability to keep the focal length of the thermal lens constant in the Nd:YVO_4 crystal. If the focal length decreases due to heating, then the D1 value that results in the minimum beam waist will also decrease, resulting in a much large beam waist which will lead to a substantial drop in laser performance. As expected, use of a larger 808 nm LD beam waist resulted in a decreased sensitivity to either a change in the temperature stability of the Nd:YVO_4 crystal or a change in the spatial configuration of the cavity. If thermal control/stability is expected to be an issue, then the use of a larger 808 nm LD beam waist is recommended.

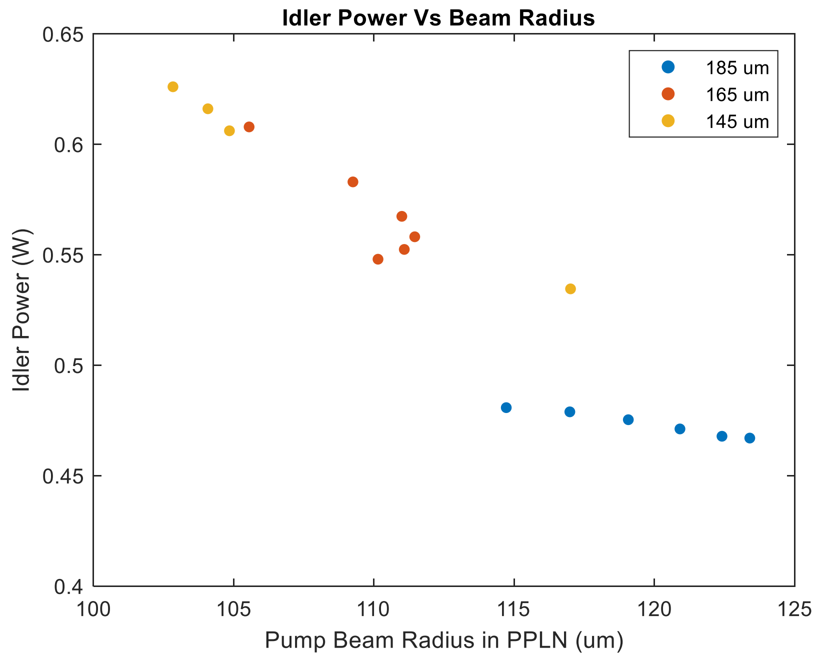

Figure 4.6: Dependence of output power on the pump beam radius in the PPLN for different LD beam waists

Figure 4.6 shows the calculated idler power at each of the data points shown in Figure 4.5. For both the 185 μm and 145 μm beam waist, we see that the idler power decreases roughly linearly with the pump beam radius. For the 165 μm beam waist, only part of the data points follow this trend. The explanation for this is as follows: for the three data points with the lowest output powers, the change in beam waist between the three data points is small, only about 1% between each of the data points. At the same time the change in the overlap integral between the pump and signal increases by about 2% as the 1064 nm beam waist increases, due to the large radius of the signal beam in the PPLN, which offsets the reduced intensity. As the beam radius continues to decrease the change in increased intensity eventually overcomes the loss due to the reduced overlap integral, which resulted in a higher output power. Due to the beams being concentric within the PPLN crystal, the overlap integral value generally remains quite high, >80%, and does not change much when the radius of any of the beams change. As a result of this, we found that it is better to design the cavity to minimize the beam waist in the PPLN crystal than to focus on increasing the overlap integral.

4.5.3 Dependence on OC Radius

Figure 4.7 shows the output idler power calculated for different OC radii with a 5 cm PPLN and having D1 and D2 set to 5 mm. The 808 nm LD beam waist in the Nd:YVO_4 crystal was set to 165 μm. The output power for both the 100 mm radius and 50 mm radius was nearly identical at all input powers. The reasons for this are as follows. Reducing the radius of the OC to 50 mm resulted in a reduced 1064 nm beam radius within the PPLN, which would normally result in a higher idler output power. However, the radius of the 1064 nm beam is also reduced inside of the Nd:YVO_4 crystal, resulting in it being smaller than the 808 nm LD beam waist. As stated in the original paper by Risk [10], it is ideal to have the 808 nm pump waist smaller than the 1064 nm waist in the Nd:YVO_4 crystal to achieve a high slope efficiency. The ratio of the 808 nm LD spot size to the 1064 nm spot size is approximately 1.7 at 10 W when using the 50 mm OC resulting in a reduced slope efficiency and a reduced circulating 1064 nm power inside of the laser cavity. The ratio when using the 100 mm OC was calculated to be 1.3 which resulted in a higher slope efficiency and circulating 1064 nm power. When using the 100 mm OC the 1064 nm power in the forward direction is calculated to be 102 W, compared to the 50 mm OC which resulted in a forward 1064 nm power of 90 W. The slope efficiency was shown to rapidly decrease as the ratio between the two beams was increased above 1, which explains the large reduction in circulating 1064 nm power in our simulations.

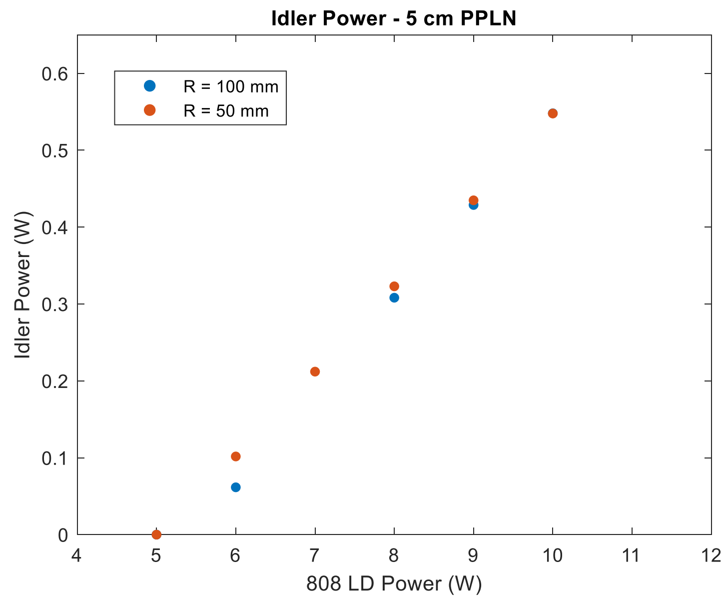

Figure 4.7: Idler power for a 5 cm PPLN with different OC radii.

As mentioned earlier, the signal beam waist inside of the PPLN crystal is much larger than the pump beam waist, which reduces the overlap integral. An advantage of the 50 mm OC is that it reduced the signal beam waist in the PPLN from 160 μm (when using the 100 mm OC) to 130 μm which improved the overlap between the pump and signal beam, increasing the conversion efficiency. The change in the overlap integral, combined with the reduced beam waist, was enough to mitigate the reduced 1064 nm power, resulting in both OCs having the same output idler power.

Figure 4.8 shows a comparison of the idler output power using a 3 cm PPLN for both a 50- and 100-mm OC radius. The 808 nm LD beam waist was set to 165 μm. D1 and D2 were both set to 5 mm. From Figure 8 a substantial increase in output power can be seen when using a 50 mm OC as opposed to a 100 mm OC. The output power increased from 300 mW, when using the 100 mm OC, to 370 mW when using the 50 mm OC. In addition to the increase in output power, the threshold of the laser was also reduced, from 7.5 W to 6.5 W, when using the 3 cm PPLN.

While switching to a 50 mm radius OC does result in a worse 808 nm to 1064 nm beam waist ratio for the 3 cm PPLN (1.46 with the 100 mm OC vs 1.74 with the 50 mm OC), the change is not as significant as with the 5 cm PPLN (1.28 with the 100 mm OC vs 1.69 with the 50 mm OC). As result the reduction in the slope efficiency and circulating 1064 nm power is not as significant when using the 3 cm PPLN. In addition to this the pump beam waist in the 3 cm PPLN has a greater decrease when using the 50 mm OC than when using the 5 cm PPLN, resulting in a greater 1064 nm intensity increase when using the shorter PPLN. The increased 1064 nm intensity results in an increased idler conversion efficiency. There is also a slight increase in the mode overlap between the signal and pump when using the 3 cm PPLN which further increases the output power.

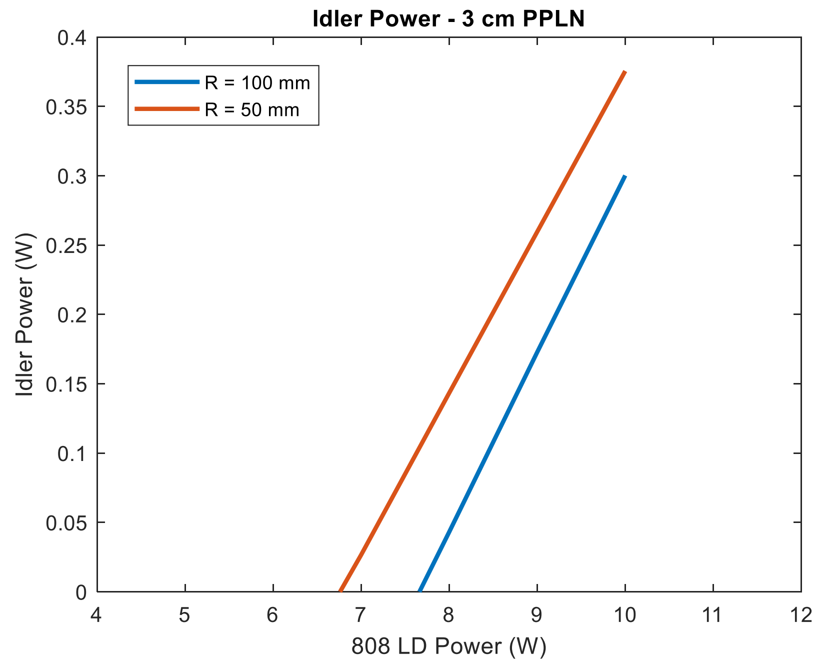

Figure 4.8: Idler power for a 3 cm PPLN with different OC radii.

One option to improve the performance of the laser when using a 50 mm OC would be to decrease the thermal lens focal length, increasing the divergence of the 1064 nm beam in the laser cavity. As a result the 1064 nm beam waist in the $Nd:YVO_4$ crystal will increase, thus increasing the slope efficiency. Figure 4.9 shows the calculated idler output power when using a 50 mm OC for different 808 nm LD beam waists. A roughly linear increase in output power is observed with a decrease in the 808 nm LD beam waist. As predicted, the main reason for the improvement in performance is due to the improved 808 nm LD to 1064 nm beam waist ratio. When the beam waist was set to 115 μm, a drop in power was observed when the input power was increased from 8 to 9 W which is due to the 1064 nm beam waist rapidly increasing in the PPLN. At 10 W the cavity was no longer geometrically stable when an 808 nm LD beam waist of 115 μm was used.

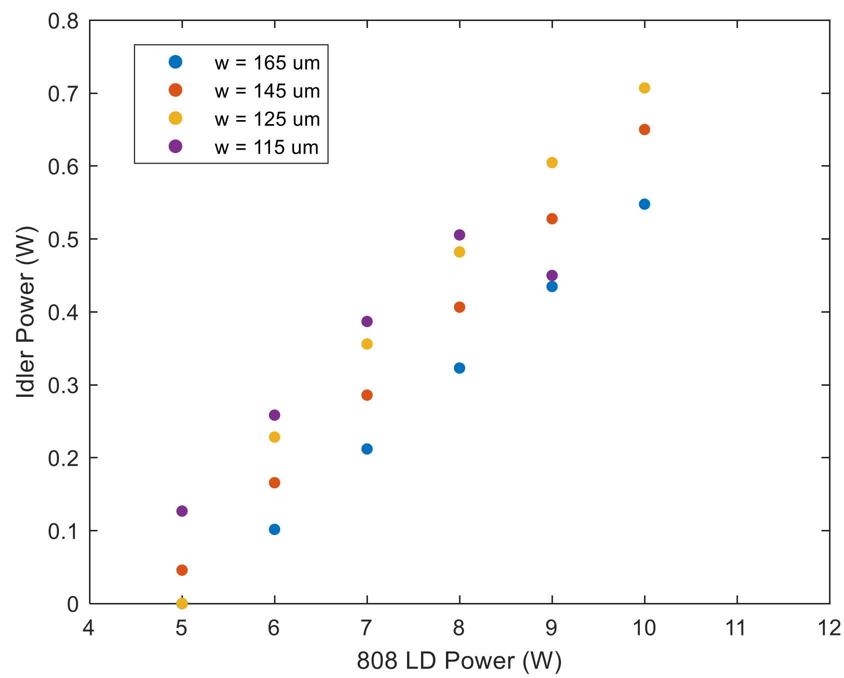

Figure 4.9: Output power for a 5 cm PPLN with a 50 mm radius at different 808 nm LD beam waists.

Figure 4.10 shows the output power for various PPLN lengths using different 808 nm LD beam waists for a 50 mm OC. Both D1 and D2 were set to 5 mm. As was discussed previously, Figure 10 shows that reducing the OC radius has a greater effect on the performance of the laser when using a shorter PPLN. This allows for the use of shorter PPLN crystal while still achieving high output powers.

For the 5 cm PPLN, the output power increased from 550 mW to 710 mW when the 808 nm LD beam waist was decreased from 165 μm to 125 μm, compared to the 3 cm PPLN which increases in power from 380 mW to 600 mW when changing the 808 nm LD beam waist from 165 µm to 110 µm. Similar to previous results, the maximum power point is followed by a rapid drop in output power before the cavity becomes geometrically unstable. For both the 4 and 5 cm PPLN decreasing the 808 nm beam waist from 125 µm to 115 µm resulted in the cavity no longer being geometrically stable.

From Figure 4.10 we can see that if an appropriate 808 nm LD beam waist is chosen, the difference in power between a 4 and 5 cm PPLN is almost negligible. Furthermore, the 3 cm PPLN maximum output power is only 60 mW less than that of the 4 and 5 cm PPLN. From this we can see that it is possible to achieve a higher output power with a 3 cm PPLN using a 50 mm OC than when using a 5 cm PPLN and 100 mm OC. Another interesting result is that if a 50 mm OC is used, is that it is possible to reach the threshold with a 2 cm PPLN, although the requirements for reaching the threshold and maintaining cavity stability are extremely strict. Only a small range of 808 nm LD beam waists allow the laser to reach threshold, before the cavity becomes unstable. From the results it is clear that higher performance can be achieved when using a smaller radius OC compared to a larger radius OC. Improved output power can be achieved with shorter PPLNs allowing for more compact laser designs, but this comes at the cost of increased temperature control requirements.

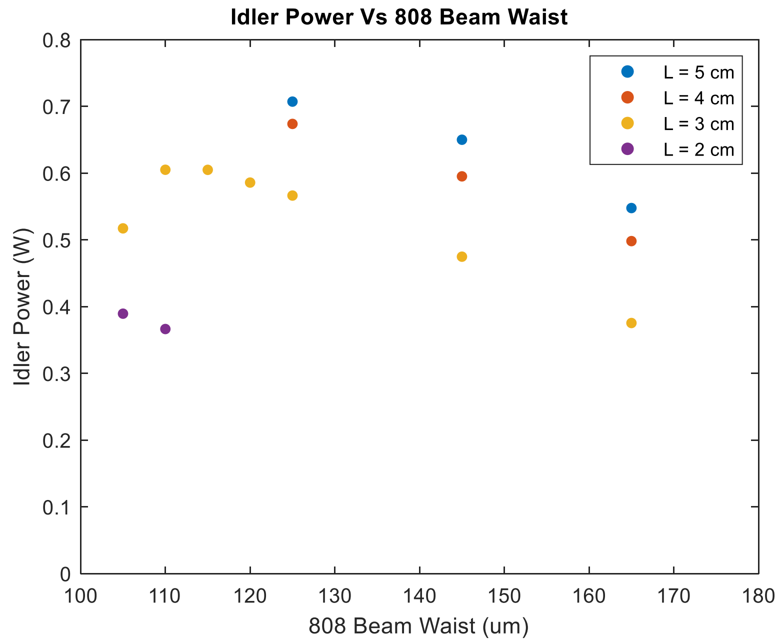

Figure 4.10: Maximum output power for different PPLN lengths at various LD beam waists with a 50 mm OC.

4.5.4 Dependence on Cavity Loss

Figure 4.11 shows the idler output power as a function of both the signal and pump cavity loss values. The loss values displayed on the x- and y-axis do not include material loss and the loss due to mirrors, but these sources of loss were considered when calculating the output power. D1 and D2 were set to 5 mm, and the input power was set to 10 W. From Figure 4.11 we see that optimizing the cavity to minimize the pump loss results in improved performance. Looking at the extremes of Figure 4.11, when the pump loss is set to 1% and the signal loss is set to 0% or vice versa, we see that the performance is approximately 15% better in the case of the 0% pump cavity loss configuration. Additionally, the threshold is also minimized by minimizing the pump cavity loss as opposed to minimizing the signal loss. As such it is found that when optimizing the cavity reducing the lost at the pump wavelength should be the primary focus.

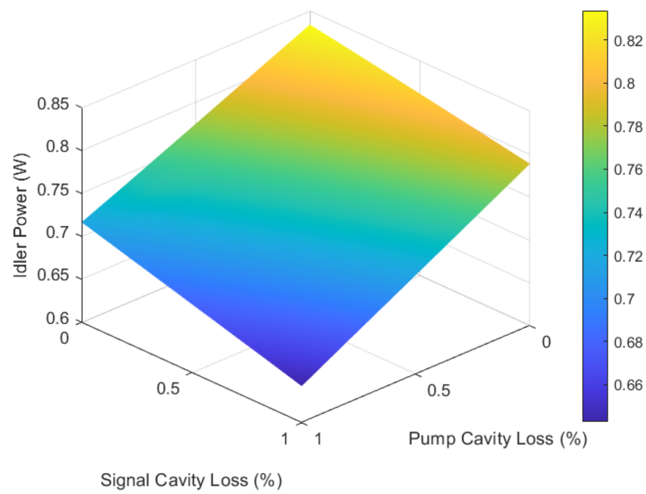

Figure 4.11: Output power for 5cm PPLN at different signal and pump cavity loss values.

Due to the forward idler beam being dependent on the backwards travelling pump it is expected that the forwards travelling idler wave will have a lower intensity than the backwards travelling idler, due to pump depletion from the nonlinear process. A worthwhile consideration is whether or not the use of an intracavity dichroic mirror, placed between the $Nd:YVO_4$ crystal and the PPLN, to extract the backwards travelling idler will result in improved performance despite the additional source of cavity loss. Figure 4.12 shows the output power of the backwards travelling idler for four different dichroic mirror loss values and the forwards travelling idler when no dichroic mirror is present in the cavity for a range of different cavity loss values. The cavity was set to the configuration which achieved the highest idler output power. The

OC radius was 50 mm, PPLN length was set to 5 cm, D1 was set to 30 mm, D2 was set to 20 mm and the 808 nm LD beam waist was set to 165 μm. Important to note is that for the data in Figure 4.12 the loss due to material absorption and due to imperfect mirrors was still considered for both the signal and pump.

As expected, when the loss of both the dichroic mirror and laser cavity is low enough, the backwards travelling idler power is larger than the forwards travelling idler, indicating that it is advantageous to use the dichroic mirror to extract the backwards travelling wave. However, the gain in output power is small. When both the pump and signal cavity have a loss value of 0%, and the loss introduced by the dichroic mirror to the pump wave is set to 0.1%, the backwards travelling idler wave has an output power roughly 6% higher than the forwards travelling idler with no dichroic mirror present in the cavity. As the loss values of the dichroic mirror and signal cavity loss are increased to more realistic values, we see that the output powers of the different cases becomes smaller until the loss due to the dichroic mirror causes the forwards travelling idler to perform better. While theoretically possible to improve the performance with the dichroic mirror and extracting the backwards travelling, low enough loss values would be extremely difficult, if not impossible, to result in a performance improvement.

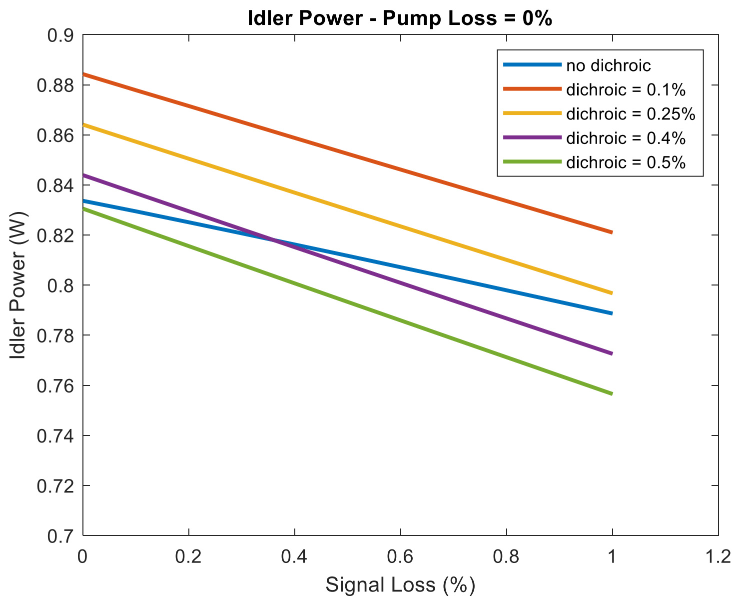

Figure 4.12: Output power achievable with and without a dichroic mirror for different mirror loss values.

4.5.5 BOPO Linewidth

One of the key characteristics of a BOPO is that the generated counterpropagating wave is expected to have a linewidth much narrower than the generated copropagating wave or the pump wave. This allows for the BOPO to be used as a source for narrow linewidth, high power, mid-ir emission. The linewidth can be estimated by expanding the BOPO phase matching condition as first order Taylor series, as long as the BOPO is operated away from the degeneracy point. Assuming the pump spectrum to be a delta function and expanding the phase matching conditions gives:

$$\Delta\omega = \frac{2.783}{\left|v_{g,i} + v_{g,s}\right| \cdot L}, \tag{77}$$

where Δω is the angular frequency bandwidth of the signal or idler wave, $v_{g,i}$ is the idler group velocity, $v_{g,s}$ is the signal group velocity and L is the crystal length. Using equation 9 an idler bandwidth of 0.02 nm is calculated for a 5 cm PPLN. Comparing this to a standard OPO where all waves co-propagate an idler linewidth of 2 nm is found. This difference is due to the counterpropagating nature of the BOPO which results in the additional of the group velocities in the denominator of equation 9; different from the conventional OPO where the difference in the group velocities appears in the denominator. Another unique aspect of the BOPO is that the wavelength tuning rate of the counterpropagating wave with respect to the pump is orders of magnitude smaller than the tuning rate of the copropagating wave with respect to the pump. The counterpropagating idler tuning rate is calculated to be 0.006 with respect to the pump, while the copropagating signal tuning rate is calculated to be 1.006 with respect to the pump [2]. Intracavity 1064 nm lasers generally have a linewidth of a few nm [18], so the idler bandwidth increase due to the pump bandwidth is expected to be approximately 0.02 nm.

4.6 Conclusions

In this chapter we have systematically studied the output performance of an intracavity backwards optical parametric oscillator. We have systematically studied the effects of PPLN length, cavity size, OC radius, input laser diode power, input laser diode spot size, and cavity loss values on the performance of the laser. We have provided design considerations and analyzed tradeoffs in parameters to allow for optimized performance to be achieved without the need for cost prohibitive prototyping. We have shown that output powers as high as 600 mW are achievable with the proposed structure in the mid-ir and that the threshold for the BOPO process can be met with a 2 cm PPLN. We believe this paper will serve as a design guideline for future development of IC-BOPOs for mid-ir light generation and allow for the development of low cost mid-ir sources that are capable of achieving high output power along with a narrow emission linewidth.

4.7 References

1. S. E. Harris, "PROPOSED BACKWARD WAVE OSCILLATION IN THE INFRARED," Appl. Phys. Lett. **9**(3), 114–116 (1966).
2. C. Canalias and V. Pasiskevicius, "Mirrorless optical parametric oscillator," Nat. Photonics **1**(8), 459–462 (2007).
3. R. S. Coetzee, A. Zukauskas, C. Canalias, and V. Pasiskevicius, "Low-threshold, mid-infrared backward-wave parametric oscillator with periodically poled Rb:KTP," APL Photonics **3**(7), 71302 (2018).
4. Y. J. Ding and J. B. Khurgin, "Backward optical parametric oscillators and amplifiers," IEEE J. Quantum Electron. **32**(9), 1574–1582 (1996).
5. C. E. Minor and R. S. Cudney, "Mirrorless optical parametric oscillation in bulk PPLN and PPLT: a feasibility study," Appl. Phys. B **123**(1), 38 (2017).
6. A. Godard, M. Guionie, J.-B. Dherbecourt, J.-M. Melkonian, and M. Raybaut, "Backward optical parametric oscillator threshold and linewidth studies," J. Opt. Soc. Am. B **39**(2), 408–420 (2022).
7. J. Kneller, L. Flannigan, and C.-Q. Xu, "Theoretical study of diode pumped intracavity backward optical parametric oscillator based on periodically poled lithium niobate," Appl. Phys. B **129**(6), 99 (2023)
8. R. C. Miller, "OPTICAL SECOND HARMONIC GENERATION IN PIEZOELECTRIC CRYSTALS," Appl. Phys. Lett. **5**(1), 17–19 (1964).
9. G. Rustad, G. Arisholm, and Ø. Farsund, "Effect of idler absorption in pulsed optical parametric oscillators," Opt. Express **19**(3), 2815–2830 (2011).
10. A. Fix and R. Wallenstein, "Spectral properties of pulsed nanosecond optical parametric oscillators: experimental investigation and numerical analysis," J. Opt. Soc. Am. B **13**(11), 2484–2497 (1996).
11. W. P. Risk, "Modeling of longitudinally pumped solid-state lasers exhibiting reabsorption losses," J. Opt. Soc. Am. B **5**(7), 1412–1423 (1988).
12. P. Lax and B. Wendroff, "Systems of conservation laws," Commun. Pure Appl. Math. **13**(2), 217–237 (1960).
13. Y.-F. Chen, "High-power diode-pumped Q-switched intracavity frequency-doubled Nd:YVO4 laser with a sandwich-type resonator," Opt. Lett. **24**(15), 1032–1034 (1999).
14. Z. Du and J. Li, "A two-stage fourth order time-accurate discretization for Lax–Wendroff type flow solvers II. High order numerical boundary conditions," J. Comput. Phys. **369**, 125–147 (2018).
15. O. Gayer, Z. Sacks, E. Galun, and A. Arie, "Temperature and wavelength dependent refractive index equations for MgO-doped congruent and stoichiometric LiNbO3," Appl. Phys. B **91**(2), 343–348 (2008).
16. Y.-F. Chen, "Design criteria for concentration optimization in scaling diode end-pumped lasers to high powers: influence of thermal fracture," IEEE J. Quantum Electron. **35**(2), 234–239 (1999).
17. R. W. Boyd, *Nonlinear Optics* (Academic, 2020).
18. V. N. Burakevich, V. A. Lisinetskii, A. S. Grabtchikov, A. A. Demidovich, V. A. Orlovich, and V. N. Matrosov, "Diode-pumped continuous-wave Nd:YVO4 laser with self-frequency Raman conversion," Appl. Phys. B **86**(3), 511–514 (2007).

5 The Effects of Thermalization on the Performance of Passively Q-switched IC-OPOs

*This chapter is reproduced from a journal article **J. Kneller**, S. Salimian Rizi, L. Flannigan, and C. Xu, "The effects of thermalization on the performance of passively Q-switched IC-OPOs," Front. Phys., vol. 12, 2024, [Online]. Available: https://www.frontiersin.org/journals/physics/articles/10.3389/fphy.2024.1428671.*

The author is the first author main contributor of this publication.

5.1 Preface

The goal of this research was to develop a model that can accurately predict both the temporal and output power characteristics of passively Q-switched IC-OPOs. As pulse durations become shorter, and comparable to the thermalization time of the stark levels within the laser crystal, the effects of thermalization can no longer be ignored. A rate equation model was proposed for a passively Q-switched laser which included the effects of thermalization as well as excited state absorption within the Q-switch crystal. These rate equations were additionally coupled with the nonlinear coupled wave equations to model a passively Q-switched IC-OPO. The pulse width and output power calculated by the model were found to be in excellent agreement with experimental results.

This paper was coauthored with Liam Flannigan who helped with simulation methodologies as well as helped to edit the manuscript and Saeed Salimian Rizi who helped with the experimental work and figure creation. This research article has been published in Frontiers in Physics.

5.2 Abstract

In this paper, we report a new model for passively Q-switched intracavity optical parametric oscillators (IC-OPOs), using Cr:YAG as a Q-switch crystal. The model considers the effects of thermalization in the Nd:YAG laser crystal, excited state absorption in the Cr:YAG saturable absorber, nonlinear loss due to pump depletion in the nonlinear crystal, the thermal lens effect and the mode overlap of the fields within the nonlinear crystal. The model is able to accurately model the pulse widths and profiles of the IC-OPO, which has not been reported. The calculated pulse width for the 1064 nm pump light was 6.2 ns compared to the experimental result of 6 ns, while the signal wave was calculated to have a pulse width of 1.75 ns compared to the experimental result of 2 ns.

5.3 Introduction

Passively Q-switched intracavity optical parametric oscillators (IC-OPOs) are an attractive method for achieving mid-infrared (mid-IR) emission due to their low cost, broadly tunable wavelength range, low threshold due to the intracavity structure and ability to achieve high output power [1-5]. Passively Q-switched lasers based on Nd:YAG as a laser crystal and Cr:YAG as a saturable absorber are well reported within literature [6,7]. In addition, the use of an optical nonlinear crystal such as periodically poled lithium niobate (PPLN) with the previously mentioned materials is a common way to achieve a passively Q-switched IC-OPOs.

The ability to accurately model both the power and temporal characteristics of IC-OPOs is of great importance to be able to rapidly prototype designs and ensure the output parameters are suitable for practical applications. Due to the nonlinear conversion efficiency increasing as the input pump intensity increases, it is often desirable to operate the pump laser with the highest intensity possible, which is accomplished by decreasing the initial transmission of the Cr:YAG crystal [6,7]. This has the combined effect of increasing the pulse energy while decreasing the pulse width, leading to substantial increases in the maximum achievable power. However, as the pulse widths reach the order of ns and sub ns, theoretical results for the temporal characteristics begin to deviate from experimental results [6,8,9]. The ability to accurately predict the peak output power is necessary to not only ensure the laser will meet the performance requirements but also to ensure the intensity does not exceed the damage threshold of the nonlinear crystal. To fully optimize the performance of the device, it is necessary to operate the IC-OPO as close to the damage threshold as possible which requires a model that can accurately calculate the peak intensity.

Currently, there exist many models for passively Q-switched IC-OPOs. However, none of them are able to accurately calculate the pulse width, resulting in inaccurate calculations of the peak intensity [1,4,9]. This is due to the developed models not considering the effects of the thermalization in the Nd:YAG crystal, which becomes important as pulse widths reach ns and sub ns levels. Currently, there exists no model for an passively Q-switched IC-OPO which considers both the effects of thermalization in the Nd:YAG laser crystal and the exited state absorption in the Cr:YAG saturable absorber.

In this paper we report a new model for a passively Q-switched IC-OPO which accounts for both the effects of thermalization in the Nd:YAG laser crystal, excited state absorption in the Cr:YAG saturable absorber, model overlap within the PPLN nonlinear crystal, and the thermal lens effect in the Nd:YAG laser crystal. We use this model to accurately calculate the output characteristics for both a pulsed 1064 nm laser and a passively Q-switched IC-OPO. We show that the model is able to accurately reproduce both the output powers of pump, signal and idler, as well as accurately model the pulse width and shape of the different beams.

5.4 Theory and Methods

5.4.1 Theoretical Model

The equations for a continuously pumped Q-switched laser, accounting for thermalization rates in the upper and lower laser level, are given by:

$$\frac{d\phi}{dt} = \frac{\phi}{t_r}(2\sigma_e(n_a - n_b)l_g - 2\sigma_{13}n_{s1}l_{Cr} - 2\sigma_{24}(n_s - n_{s1})l_{Cr} - L - \ln(R)) \tag{78}$$

$$\frac{dn_a}{dt} = W_p - \frac{n_a - f_a n_u}{\tau_{therm}} - \frac{n_a}{\tau_a} - \sigma_e c\phi(n_a - n_b) \tag{79}$$

$$\frac{dn_b}{dt} = \sigma_e c\phi(n_a - n_b) - \frac{n_b}{\tau_b} - \frac{n_b - f_b n_l}{\tau_{therm}} \tag{80}$$

$$\frac{dn_s1}{dt} = \frac{n_s - n_{s1}}{\tau_{sa}} - \sigma_{13} c\phi n_s \quad (81)$$

$$\frac{dn_u}{dt} = \frac{n_a - f_a n_u}{\tau_{therm}} - \frac{n_u}{\tau_a} \quad (82)$$

$$\frac{dn_l}{dt} = \frac{n_b - f_b n_l}{\tau_{therm}} - \frac{n_l}{\tau_b} \quad (83)$$

where ϕ is the intracavity photon density, t_r is the round trip transit time, σ_e is the stimulated emission cross section of the laser crystal, n_a is the population of the lasing stark level of the upper laser level, n_b is the population of the lower laser stark level, l_g is the length of the gain medium, σ_{13} is the absorption cross section of Cr:YAG, n_{s1} is the population density of the first excited state in Cr:YAG, l_{cr} is the length of the Cr:YAG crystal, σ_{24} is the absorption cross section of the excited state of Cr:YAG, n_s is the total population density of the Cr:YAG, L is the residual optical loses in the cavity, R is the mirror loss, W_P is the pumping rate to the upper laser level, fa is the ratio of the population density of the upper stark level and the remaining stark levels, n_u is the population density of the remaining stark levels, τ_{therm} is the thermalization time for the upper and lower laser stark levels, τ_a is the lifetime of the upper laser level, c is the speed of light, f_b is the ratio of the lower laser stark level and the remaining stark levels in the lower laser level, n_l is the population density of the lower laser level, τ_b is the lifetime of the lower laser level, τ_{sa} is the lifetime of the Cr:YAG excited state. The variables and their value are summarized in Table 1 at the end of the manuscript, with references provided where applicable.

Equations similar to Eqs.(78)-(83) presented above have been well reported in literature and have been successfully used to accurately predict the output power of passively Q-switched lasers based on Cr:YAG [6,7]. However, when calculating the temporal characteristics of the laser pulse, the models fail and return pulse values much shorter than what is experimentally measured when the duration of the pulse is comparable to the thermalization time [8]. To account for this issue, the equations have been modified to include the thermalization effects. This requires the inclusion of two additional equations (Eqs. 82 & 83) to model the population densities of the remaining stark levels in the upper and lower laser level [8].

When the pulse duration is long as compared to the thermalization time, the standard values for f_a and f_b can be used (i.e. the population fraction at thermal equilibrium of the upper and lower laser stark level, respectively). However, when the pulse duration becomes comparable to the thermalization time, the equilibrium occupation factors can no longer be used. To understand how the inclusion of thermalization rates in the upper and lower laser level affect the performance of the Q-switched laser, let us consider a laser operating during the pulse phase. When the population inversion reaches sufficient levels, the intracavity photon density beings to rapidly grow. This results in an increase in the population density of the lower laser stark level due to stimulated emission events. Generally, when not considering the thermalization rates, it is assumed that the occupation of the lower laser stark level will be roughly equal to the Boltzmann occupation factor. This assumption requires that the thermalization time is short as compared to the pulse length. If the pulse length is comparable to the thermalization time this assumption becomes invalid. If we look at Eq. (80), we can see that by including a term for the thermalization rate, this creates a bottleneck and causes a buildup of the population of the lower laser stark value much larger than the Boltzmann occupation factor when the pulse length is short. This results in a substantial reduction in the population inversion density which lowers the rate of stimulated emission. The reduced stimulated emission results in a lower photon density, reducing the rate at which energy can be extracted from the laser crystal. Since the total population densities of the upper and lower laser level remain the same, only the distribution of the population within the stark levels is changed, the total energy able to be extracted remains unchanged. The result is that the pulse width of the laser is increased, resulting in a decreased peak power.

At low to moderate pumping levels, the time between pulses is long compared to the thermalization time allowing for the use of previously reported equations to calculate the pulse repetition rate [7]:

$$f = \tau_a \ln\left(\frac{\left(1 - \frac{\beta W_{th}}{W}\right)}{1 - \frac{W_{th}}{W}}\right) \tag{84}$$

where f is the repetition rate, and W_{th} is the threshold pumping rate. β is defined as [7]:

$$\beta = 1 - \frac{f_a}{\gamma}\left(1 - \frac{n_f}{n_i}\right) \tag{85}$$

where γ is the inversion reduction factor, n_f is the population density of the upper laser level after the laser pulse and n_i is the population density of the upper laser level when the pulse begins.

Modeling a pulsed optical parametric oscillator requires solving the coupled wave equations in both time and space. The time and spatially dependent coupled wave equations are given by:

$$\frac{\partial A_s}{\partial z} + \frac{1}{\nu_s}\frac{\partial A_s}{\partial t} = +i\kappa P(z) A_p A_i^* \exp[i\Delta kz]\beta_{pi} - \frac{\alpha_s}{2} A_s \tag{86}$$

$$\frac{\partial A_i}{\partial z} + \frac{1}{\nu_i}\frac{\partial A_i}{\partial t} = +i\kappa P(z) A_p A_s^* \exp[i\Delta kz]\,\beta_{ps} - \frac{\alpha_i}{2} A_i \tag{87}$$

$$\frac{\partial A_p}{\partial z} + \frac{1}{\nu_p}\frac{\partial A_p}{\partial t} = +i\kappa P(z) A_s A_i \exp[i\Delta kz]\,\beta_{si} - \frac{\alpha_p}{2} A_p \tag{88}$$

where A_s, A_i and A_p are the slowly varying signal, idler and pump amplitudes, respectively. P(z) is a periodic function which models the poling in the PPLN, taking a value of ±1 depending on if the region has a positive or negative nonlinear coefficient. Δk is the momentum mismatch given by $\Delta k = k_p - k_s + k_i$. α_s, α_i, α_p are the material loss values for PPLN at the signal, idler and pump wavelengths, respectively. The substitution $A = \sqrt{n/\omega}E$ was made to enable the use of a single coupling constant *κ,* where:

$$\kappa = \frac{d_{PPLN}^{(2)}}{2c}\sqrt{\frac{\omega_s\omega_i\omega_p}{n_s n_i n_p}} \tag{89}$$

where d_{PPLN} is the second order nonlinear coefficient d_{33} of PPLN, c is the vacuum speed of light, ω is the angular frequency of the respective wave and n is the refractive index of the respective wave in PPLN. Within the coupled wave equations, an additional term, β was added, which is used to account for the overlap between the relevant waves in each of the equations. The value of β ranges from 0-1 depending on the overlap of the two fields, with β=1 representing perfect overlap and β=0 representing no overlap. The overlap of two fields can be evaluated as:

$$\beta_{is} = \frac{|\iint E_s(x,y)\cdot E_i(x,y)dxdy|^2}{\iint |E_s(x,y)|^2 dxdy \iint |E_i(x,y)|^2 dxdy} \tag{90}$$

where E_i is the spatial distribution of the idler electric field and E_s is the spatial distribution of the signal electric field. Calculation of the overlap parameter requires knowledge of the special distribution of the fields within the nonlinear crystal. To accomplish this an ABCD matrix method was used to model the intensity distributions of the three fields within the laser cavity.

Due to the placement of the nonlinear crystal within the laser cavity, the effect of the nonlinear conversion process on the intracavity photon pump density must be considered. In order to do this, the rate equations (Eqs. (78)-(83)) must be coupled with the nonlinear wave equations (Eqs. (86)-(88)). The first step in coupling the two sets of equations together is to use the intracavity power determined by the photon density from Eq. (78) as the input to the pump wave in the coupled nonlinear equations. The unidirectional intracavity power result from a photon density ϕ can be calculated as:

$$P_{IC} = \frac{h\nu_p \pi r_p^2 \phi c}{2n_{avg}} \tag{91}$$

where h is Plancks constant, ν_p is the pump wave frequency, r_p is the radius of the pump beam in the laser crystal, and n_{avg} is the average refractive index of the laser cavity at the pump wavelength.

To model the loss in photon density due to the nonlinear conversion process, an additional term must be added to Eq.(78). Modifying Eq. (78) to include this term gives:

$$\frac{d\phi}{dt} = \frac{\phi}{t_r}(2\sigma_e(n_a - n_b)l_g - 2\sigma_{13}n_{s1}l_{Cr} - 2\sigma_{24}(n_s - n_{s1})l_{Cr} - L - \ln(R)) - \frac{\phi_{NL}}{t_r} \tag{92}$$

where ϕ_{NL} is the photon density lost due to the nonlinear conversion process. Determining ϕ_{NL} can be done by considering the underlying physics of the nonlinear conversion process. For every generated signal and idler photon, there must be a pump photon removed due to the conservation of energy. From this, it is clear that an increase in either the signal or idler photon count due to the nonlinear process must result in an equal and opposite change in the pump photon count. From this, the photon density change can be calculated by considering the mode area of the pump beam in the nonlinear crystal. This can be calculated as:

$$\phi_{NL} = \frac{n_{avg} P_i}{h\nu_i \pi r_{NL}^2 c} \tag{93}$$

where P_i is the change in idler power within the nonlinear crystal, ν_i is the idler frequency, r_{NL} is the radius of the pump beam within the nonlinear crystal.

5.4.2 Numerical Method

A 5th order Runge Kutta method was used to solve the system of ODEs (ordinary differential equations) for the pulsed laser [10]. The time between pulses was solved with an adaptive error method to allow for the largest possible step size to be used until the photon density (Eq. (78)) began to increase. Once the photon density began to increase a constant step size was used to ensure that the numerical method used to solve the coupled nonlinear equations remained stable. During the time between pulses, the intracavity power was assumed to be 0 and hence there was no input to the coupled wave equations. This eliminated the need to solve them during the time between pulses, which greatly reduced the computation time.

To solve the coupled wave equations, a lax-wendroff method was used [11]. The intracavity operation results in the confinement of both the signal and pump beam, resulting in both waves travelling in the forwards and backwards direction. To account for this, each field was divided into two components, a forwards and backwards component, and handled separately [12]. By the conservation of energy, a forward and backwards travelling idler wave must also be generated, although both idler waves are assumed to be perfectly coupled out of the cavity. Due to the conservation of momentum from the phase matching conditions, the forwards travelling waves do not interact with the backwards travelling waves and vice versa. The boundary conditions for each wave were calculated using polynomial interpolation [13].

5.4.3 Experimental Setup

Figure 5.1a shows the experimental setup used to test the 1064 nm pulsed laser. An 808 nm fiber laser diode (Aerodiode 808LD-2-0-0) was used to pump an Nd:YAG crystal. The light from the fiber was focused into the Nd:YAG crystal to a radius of 120 μm. The input facet of the Nd:YAG crystal was antireflection (AR) coated at 808 nm and high reflection coated (HR) at 1064 nm. The output facet of the Nd:YAG crystal was AR coated at 1064 nm. The Nd:YAG crystal had a length of 4.9 mm. A [110] Cr:YAG crystal with T_0 = 60% was used as the Q-switch crystal. The [110] orientation was used to polarize the output from the Nd:YAG crystal, which is normally unpolarized [14]. The output coupler was a curved mirror with a 100 mm radius and was HR coated at 1064 nm (R = 99.98%). The total cavity length was 53 mm.

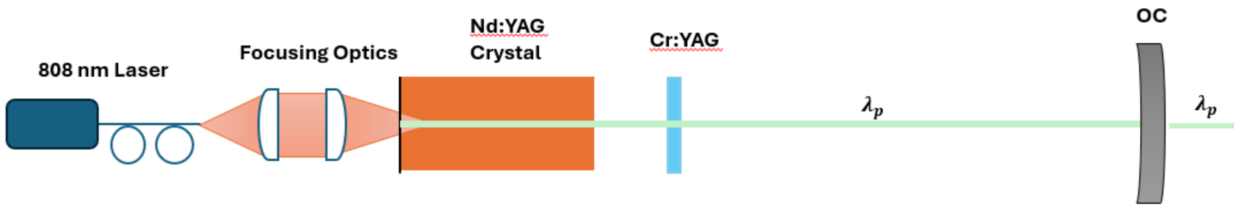

Figure 5.1a: Setup for 1064 nm pulsed laser

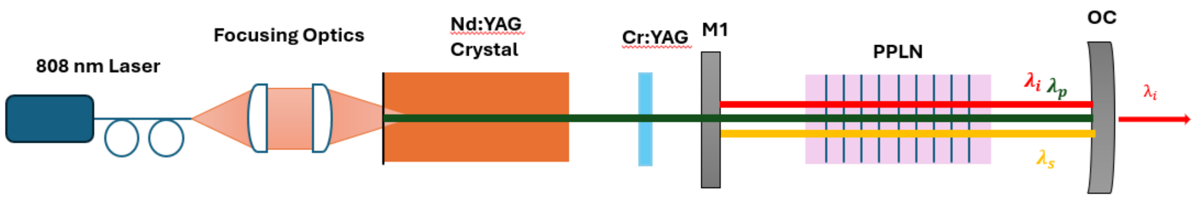

Figure 5.1b: Setup for passively Q-switched IC-OPO

Figure 5.1b. shows the experimental setup for the passively Q-switched IC-OPO. The structure is similar to the setup presented in Figure 1a, the difference being the addition of a dichroic mirror (M1) after the Cr:YAG crystal and a PPLN crystal. The dichroic mirror had high transmission at 1064 nm and was HR coated at the signal wavelength (1550 nm). Both faces of the PPLN crystal were AR coated at the pump, signal and idler wavelength. The length of the PPLN crystal was 14.7 mm. The nonlinear coefficient of PPLN for second harmonic generation at 1064 nm is reported as 25.3 pm/V [15]. Millers rule was used to calculate the appropriate nonlinear coefficient, which was found to be 20.7 pm/V [16]. The OC used was the same as in Figure 1a, having a partial reflection at the signal wavelength (R = 15%) and a high transmission at the idler wavelength (3394 nm) (R < 1%). The total cavity length was 53 mm.

5.5 Results

5.5.1 Passively Q-switched 1064 nm Laser

To validate the proposed rate equations, the laser setup described in Figure 1a. was investigated initially. Figure 5.2 shows the theoretically calculated repetition rate as compared to the experimentally measured repetition rate as a function of input laser diode power. The simulation parameters used are provided in Table 5.1. The theoretical repetition rate was calculated by solving the rate equations for two full pulses and then calculating the time between the two pulses. As expected, the theoretical repetition rate increases linearly with increasing input power, indicating inclusion of the thermalization rate does not affect the relationship between input power and the repetition rate. The linear relationship between the input power and repetition rate is in agreement with previously reported experimental and theoretical results [6,7]. Our experimental results exhibit a minor deviation from the expected linear increase with pump power, which is likely due to thermal instability. Above input powers of 4.5 W, the temperature of the laser diode and Nd:YAG crystal began to increase, which resulted in reduced absorption efficiency of the pump light by the Nd:YAG crystal.

As previously stated, the inclusion of the thermalization terms in the rate equations should not affect the calculated repetition rate due to the thermalization time being significantly less than the time between pulses. This was confirmed by calculating the repetition rate using Equation (7), which was found to be in agreement with the results obtained from solving the rate equations. Additionally, the recovery time of the Cr:YAG crystal is in an order of microseconds, which would prevent the time between pulses approaching the thermalization time [7].

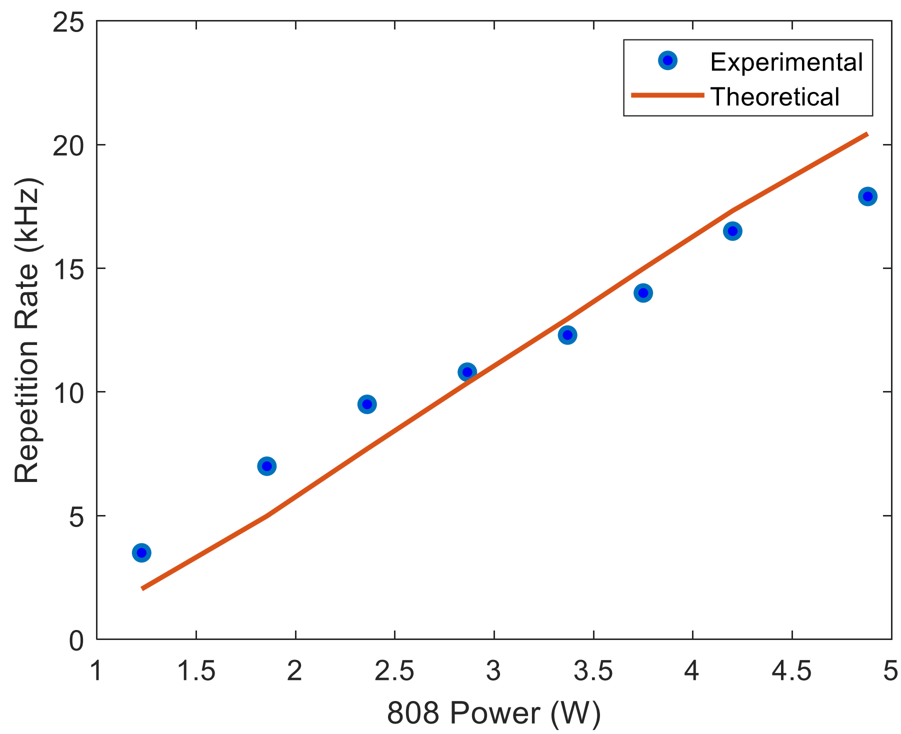

Figure 5.2: Repetition rate of the passively Q-switched 1064 nm laser

Figure 5.3 shows the measured pulse profile of the 1064 nm laser as compared to the theoretical calculated from the proposed model. A thermalization time of 5 ns was found to produce the best results, which is in agreement with previously reported results for the thermalization time in Nd:YAG of 3 - 5 ns [8]. As shown in Figure 5.3, the model accurately predicts the asymmetric pulse shape, as well as correctly models the rise and fall time of the pulse. The theoretically calculated pulse width was 6.2 ns which is in good agreement with the experimentally measured pulse width of 6 ns.

It is worth noting that the experimental results cannot be explained by the previously reported models, where the calculated pulse width is generally much shorter than the experimental pulse width [6,7]. Without considering the effects of thermalization, the simulated pulse width was approximately 3 ns, half of what was experimentally measured. Additionally, when the effects of thermalization are not considered a symmetric pulse profile is returned, consistent with the pulse shape using previously reported models [6].

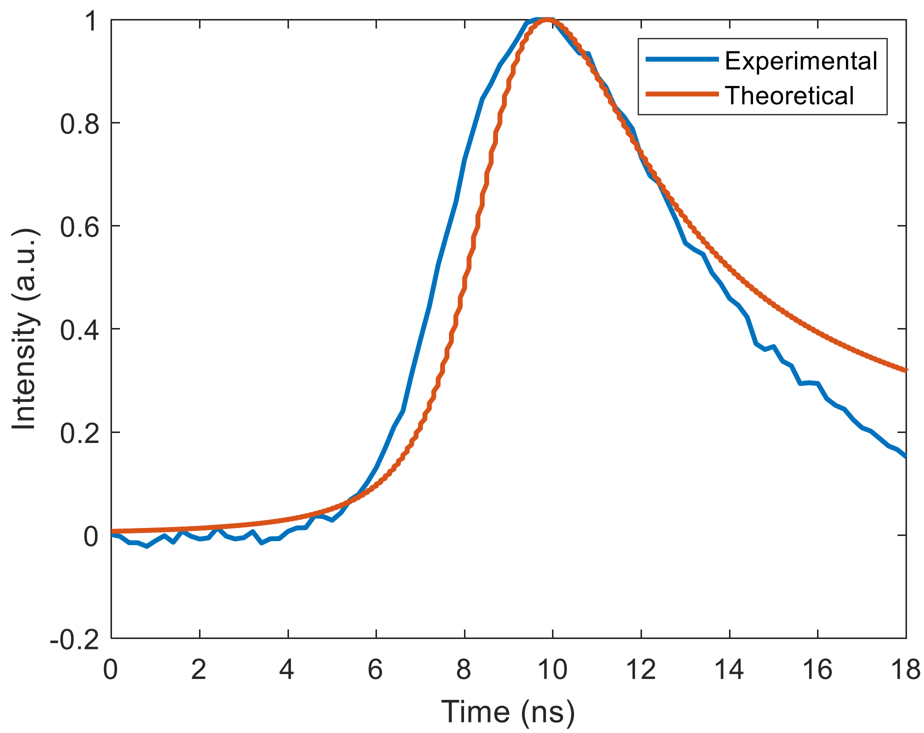

Figure 5.3: Pulse shape of the 1064 nm Q-switched laser

It is also worth mentioning that the presented model predicts average power of the passively Q-switched IC-OPO. Due to the high reflectivity of the OC at 1064 nm used in our experiments, the average output was only able to be measured at high input powers. At an input power of 4.2 W, the average power was measured to be 800 μW, which is in good agreement with the model prediction of 820 uW. To the best of our knowledge, for the first time, the modal presented in this paper enables us to predict precisely both the pulse properties (pulse shape and pulse width) and output power of the passively Q-switched IC-OPO.

5.5.2 Passively Q-switched IC-OPO

The laser structure in Figure 5.1b was used to validate the model for a passively Q-switched IC-OPO, focusing on signal and idler pulses. The pulse repetition rate and pulse profile of the signal wave were calculated with the model and compared to experimental results. Due to equipment limitations, we were only able to measure the pulse shape of the signal wave and not the idler. The repetition rate of the IC-OPO was found to be the same as the previous laser structure which is expected as the loss due to the insertion of the PPLN into the cavity is much smaller than the loss due to the Cr:YAG crystal. Figure 5.4 shows the experimentally measured pulse shape of the signal as compared to the theoretical pulse shape predicted by the model. In the study, pump, signal and idler wavelength were 1064 nm, 1548 nm, and 3400 nm, respectively. The material loss values at the pump, signal and idler wavelength were 0.0035 cm^{-1}, 0.0035 cm^{-1} and 0.008 cm^{-1}, respectively [17]. The model predicts the pulse shape with reasonable accuracy. The measured pulse width was 2 ns, as compared to the theoretical pulse width of 1.75 ns. It is worth noting that when the effects of thermalization were not considered, the signal pulse width was approximately 1 ns. This is consistent with the results for the 1064 nm pulsed laser, where removing the thermalization effects resulted in a reduced pulse width.

As shown in Figure 5.4, the experimental rise time of the signal pulse was much longer than the theoretical pulse, while the falling edge of the pulse was almost identical to the experimentally measured pulse. This discrepancy between the measured results and theoretical results is likely due to either an incorrect pump beam size in the PPLN being used or errors in the poling of the PPLN reducing the effective nonlinear coefficient which was not considered in the model. If the 1064 nm beam waist in the PPLN used in the simulation was less than the actual value, it will result in the 1064 nm field intensity in the PPLN being higher in the simulation than in the actual laser. As a result, the conversion efficiency of the nonlinear process will increase which would result in a quicker pulse buildup, as seen in Figure 5.4. Errors in the PPLN poling could also be responsible for the discrepancy as this would result in a reduced conversion efficiency in the experiment, leading to a longer pulse buildup time in the experimental case.

The rapid increase in the signal intensity is consistent with previously reported results for Q-switched IC-OPOs [2,18], although the OC reflectivity at the signal wavelength was much larger than in our setup. The lack of a rapid rise in the signal pulse in our experimental results is likely due to limitations of the time resolution of the oscilloscope used in our experiments. Therefore, it is likely that the minor discrepancy between the theoretical and experimental results (both the pulse width and the rise time) is due to the oscilloscope used.

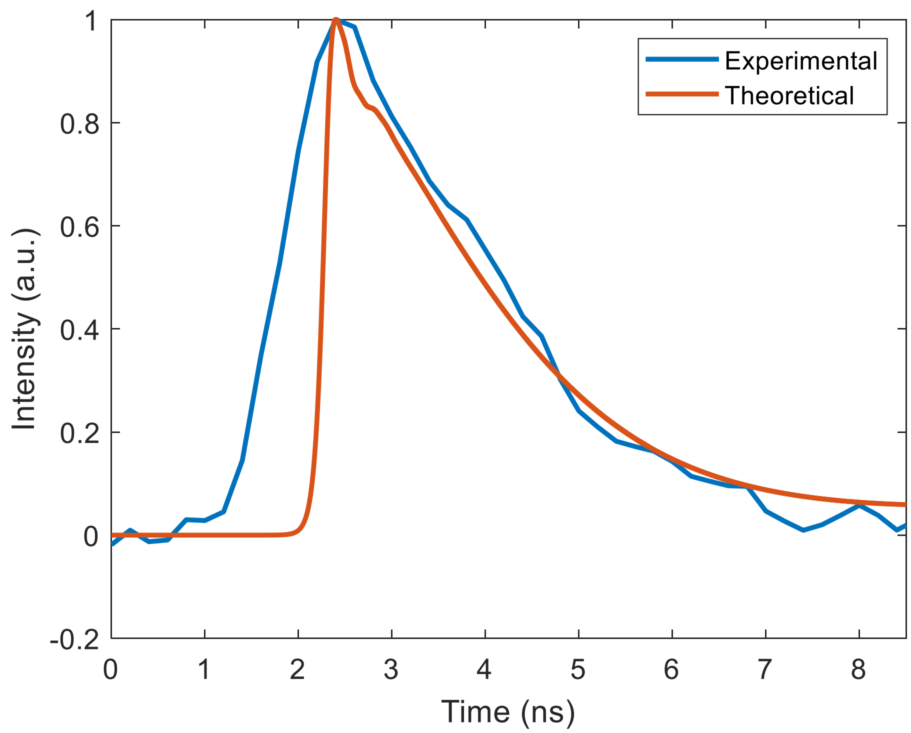

Figure 5.4: Pulse shape of the signal from the IC-OPO

In addition to the consideration of the thermalization effects, our model for signal and idler pulses also considers the spatial intensity variation of the pump, signal and idler within the nonlinear crystal. If the spatial variation in the pump wave within the nonlinear crystal is not considered, which arises due to pump depletion from the nonlinear conversion process with a high efficiency, the calculated conversion efficiency will likely be overestimated [18]. From Eq. (92), we can see that the increased nonlinear loss term would cause the cavity photon density to decrease faster which in turn would produce a shorter pulse; consistent with what the authors observed from their model. We tested this conclusion with our own model by multiplying Eq. (93) by a constant, with a value greater than 1, and found that it did result in a decreased pulse width as expected. The pulse width decreasing as the nonlinear conversion efficiency increases is consistent with previously reported results where only the time dependence of the three fields in the cavity was considered [18].

The measured average output power of the signal as compared to the theoretically predicted value is presented in Figure 5.5. As shown in Figure 5.5, the theoretical results match the linear trend observed in the experimental results and accurately predict the average power values. The deviation in the experimental results from the theoretical ones is likely due to thermal instability resulting in an inconsistent repetition rate. Another discrepancy can be caused by the uncertainty in the laser mode size in the Nd:YAG crystal. Since the mode size determined by the cavity geometry, calculated with an ABCD matrix, is larger than the beam waist of the 808 nm pump laser, the laser mode size will be determined by the 808 nm beam radius. However, as discussed in-depth previously by other authors [19], lasing is not able to be achieved over the entire area illuminated by the 808 nm laser beam. Instead, an effective area must be used. Using the same method [19], we estimate the effective beam area of the 808 nm laser to be roughly 70% of the actual 808 nm beam area. We set the area of the 1064 nm laser mode in the Nd:YAG crystal to be equal to the effective area of the 808 nm laser diode. As a result, it is difficult to determine the exact 1064 nm spot size, and hence the pulse energy.

Although the theoretical results show the expected linear trend, the theoretically simulated curve is not smooth as is generally expected. This is due to the inclusion of the thermal lens in the Nd:YAG crystal. As the input power changes, the value of the thermal lens changes, which results in a small change in the pump radius within the PPLN. The change in pump radius results in a change in the conversion efficiency of the nonlinear interaction, causing the pulse energy of the signal to change. Since the repetition rate does not change, this results in slight deviation from the expected linear curve.

To investigate the mid-IR idler wave generated from the IC-OPO, the calculated idler power as compared to the measured idler power is shown in Figure 5.6. A germanium filter was placed between the OC and power meter and was used to filter all wavelengths besides the idler wavelength. An initial linear growth in both the theoretical and experimental results is seen, until the output rate beings to decrease. This is likely due to temperature instability in the Nd:YAG crystal and pump fiber laser, which results in a reduced pulse repetition rate due to the 808 nm LD pump depletion. Another reason for this is the changing of the pump beam waist due to a change in the thermal lens focal length in the Nd:YAG crystal. Increasing the input power from the 808 nm laser will decrease the focal length of the thermal lens, changing the pump beam radius in the PPLN crystal.

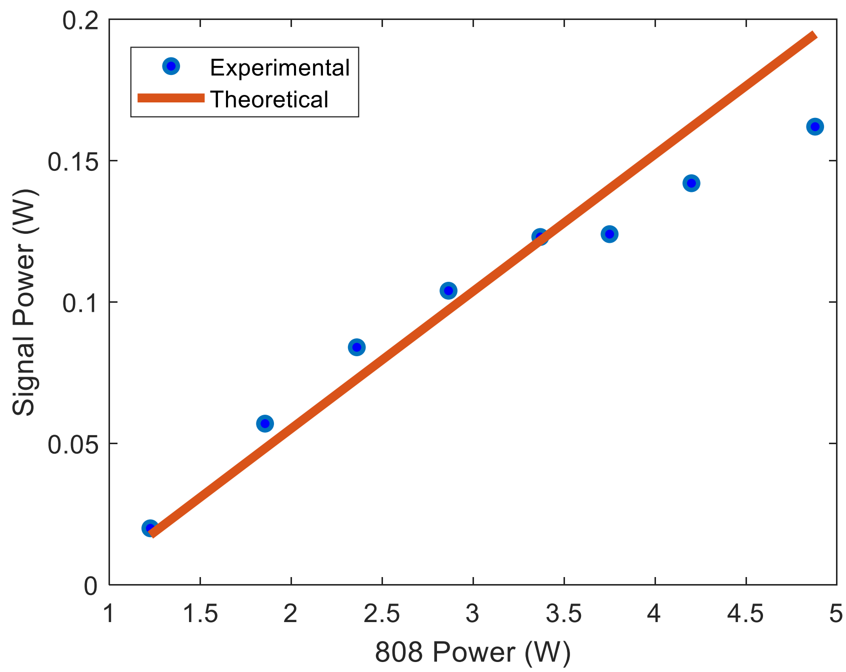

Figure 5.5: Average output power from the IC-OPO at the signal wavelength.

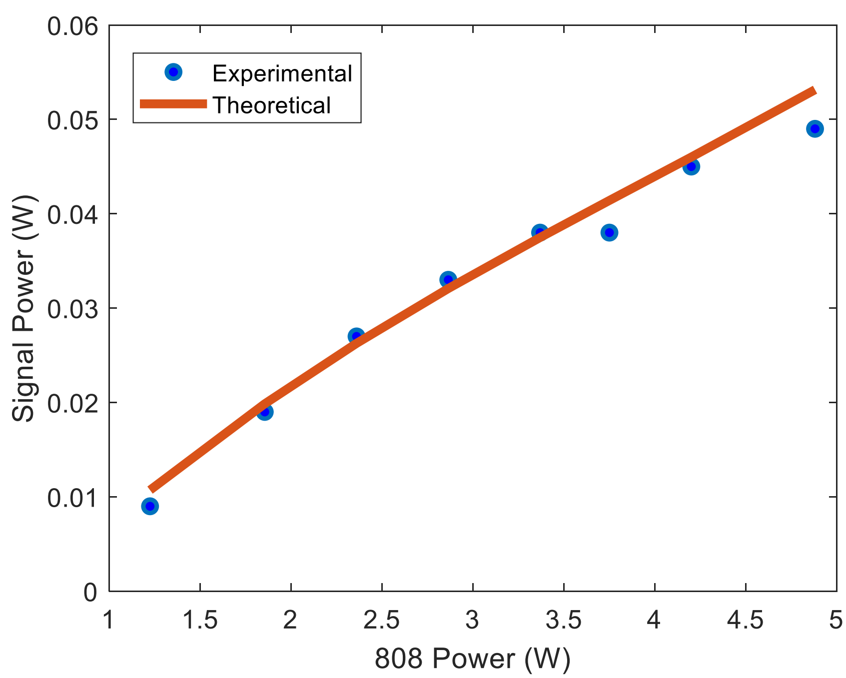

Figure 5.6: Average output power form the IC-OPO at the idler wavelength.

We also measured the profile and divergence angle of the pump and signal beams. Figures 5.7a and 5.7b show the measured beam profile of the pump and signal beams, respectively, 18 cm after the OC. The radius of the pump and signal at the point of measurement were 1.1 mm and 2.4 mm, respectively. The divergence angle of the pump and signal beams were measured to be 3.7 and 11 mrad, respectively. Using these values, we can estimate the beam waist of the pump and signal at the OC to be 0.43 mm and 0.42 mm, respectively. Both values are in good agreement with the calculated values from the ABCD matrix method which was used. Additionally, both fields have a gaussian intensity distribution which was assumed when using the overlap integral and is required for the ABCD matrix method to be valid. We also measured the wavelength of the signal beam and found it to be 1553 nm, which results in an idler wavelength of 3379 nm.

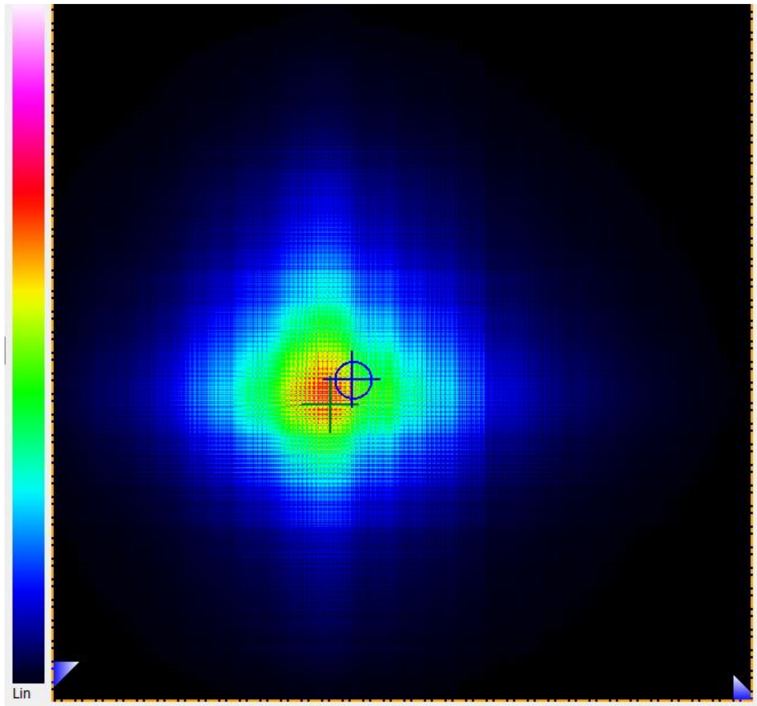

Figure 5.7a: Profile of the pump beam.

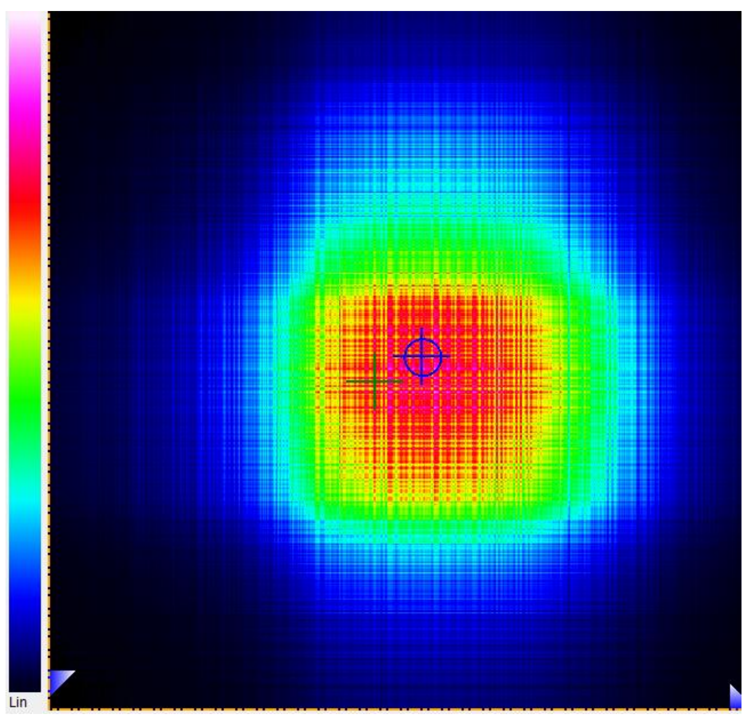

Figure 5.7b: Profile of the signal beam.

5.6 Conclusions

We have developed a theoretical model to calculate the output characteristics of passively Q-switched lasers with Nd:YAG as the laser medium and Cr:YAG as the saturable absorber. The model accounts for the effects of thermalization between the stark levels of the upper and lower laser levels as well as excited state absorption within the Cr:YAG saturable absorber. To validate the proposed model we compared the results against experimental data for Nd:YAG/Cr:YAG passively Q-switched laser. A pulse width of 6 ns was experimentally measured from the passively Q-switched laser, while a pulse width of 6.2 ns was calculated demonstrating the accuracy of the proposed model. Additionally, the repetition rate was also found to agree well with the experimental values and not be affected by the inclusion of thermalization effects as expected.

The developed model for the passively Q-switched laser was modified to include an intracavity nonlinear crystal to simulate the theoretical performance of a passively Q-switched IC-OPO. The IC-OPO model considers both the time and spatial variation of the pump, signal and idler fields, and uses a nonlinear loss parameter to couple it to the passively Q-switched laser model to account for pump depletion due to the nonlinear process. A passively Q-switched IC-OPO was developed to gather experimental results to validate the model. The model was found to be in good agreement with experimental results, returning a signal pulse width of 1.7 ns compared to the experimentally measured pulse width of 2 ns. The developed model is the first model, to the best of our knowledge, to allow for the accurate prediction of temporal characteristics of passively Q-switched IC-OPOs.

Table 5.1: Values of constants used in the rate equations.

Variable	Value	Reference	Variable	Value	Reference
σ_e	6.6E-19	[7]	R	99.98 %	
l_g	4.9 mm		f_a	0.69	
σ_{13}	4.3E-18 cm^2	[6,7]	τ_{therm}	5 ns	[8]
l_{cr}	3 mm		τ_a	230 μs	[6,7]
σ_{24}	8.2 E-19 cm^2	[6,7]	c	3E8 m/s	
L	3 %		f_b	0.23	
τ_b	300 ns	[7]	τ_{sa}	4 μs	[6,7]

5.7 References

1. Huang YP, Huang YJ, Cho CY, Chen YF. Influence of output coupling on the performance of a passively Q-switched Nd:YAG laser with intracavity optical parametric oscillator. Opt Express [Internet]. 2013;21(6):7583–9. Available from: https://opg.optica.org/oe/abstract.cfm?URI=oe-21-6-7583

2. Chen YF, Chen SW, Chen YC, Lan YP, Tsai SW. Compact efficient intracavity optical parametric oscillator with a passively Q-switched Nd:YVO4/Cr4+ : YAG laser in a hemispherical cavity. Appl Phys B [Internet]. 2003;77(5):493–5. Available from: https://doi.org/10.1007/s00340-003-1279-3

3. Xiao G, Bass M, Acharekar M. Passively Q-switched solid-state lasers with intracavity optical parametric oscillators. IEEE J Quantum Electron. 1998;34(11):2241–5.

4. Chen YF, Chen SW, Tsai LY, Chen YC, Chien CH. Efficient sub-nanosecond intracavity optical parametric oscillator pumped with a passively Q-switched Nd:GdVO4 laser. Appl Phys B [Internet]. 2004;79(7):823–5. Available from: https://doi.org/10.1007/s00340-004-1623-2

5. Tsai LY, Chen YF, Lin ST, Lin YY, Huang YC. Compact efficient passively Q-switched Nd:GdVO4/PPLN/Cr4+:YAG tunable intracavity optical parametric oscillator. Opt Express [Internet]. 2005;13(23):9543–7. Available from: https://opg.optica.org/oe/abstract.cfm?URI=oe-13-23-9543

6. Pavel N, Saikawa J, Kurimura S, Taira T. High Average Power Diode End-Pumped Composite Nd:YAG Laser Passively Q-switched by Cr4+:YAG Saturable Absorber. Jpn J Appl Phys [Internet]. 2001;40(3R):1253. Available from: https://dx.doi.org/10.1143/JJAP.40.1253

7. Zhang X, Zhao S, Wang Q, Zhang Q, Sun L, Zhang S. Optimization of Cr/sup 4+/-doped saturable-absorber Q-switched lasers. IEEE J Quantum Electron. 1997;33(12):2286–94.

8. Degnan JJ, Coyle DB, Kay RB. Effects of thermalization on Q-switched laser properties. IEEE J Quantum Electron. 1998;34(5):887–99.

9. Bai F, Wang Q, Liu Z, Zhang X, Wan X, Lan W, et al. Theoretical and experimental studies on output characteristics of an intracavity KTA OPO. Opt Express [Internet]. 2012;20(2):807–15. Available from: https://opg.optica.org/oe/abstract.cfm?URI=oe-20-2-807

10. Dormand JR, Prince PJ. A family of embedded Runge-Kutta formulae. J Comput Appl Math [Internet]. 1980;6(1):19–26. Available from: https://www.sciencedirect.com/science/article/pii/0771050X80900133

11. Lax P, Wendroff B. Systems of conservation laws. Commun Pure Appl Math [Internet]. 1960 May 1;13(2):217–37. Available from: https://doi.org/10.1002/cpa.3160130205

12. Kneller J, Flannigan L, Xu C-Q. Theoretical study of diode pumped intracavity backward optical parametric oscillator based on periodically poled lithium niobate. Appl Phys B [Internet]. 2023;129(6):99. Available from: https://doi.org/10.1007/s00340-023-08045-4

13. Du Z, Li J. A two-stage fourth order time-accurate discretization for Lax–Wendroff type flow solvers II. High order numerical boundary conditions. J Comput Phys [Internet]. 2018;369:125–47. Available from: https://www.sciencedirect.com/science/article/pii/S0021999118302948

14. Sakai H, Sone A, Kan H, Taira T. Polarization stabilizing for diode-pumped passively Q-switched Nd:YAG microchip lasers. In: Advanced Solid-State Photonics [Internet]. Incline Village, Nevada: Optica Publishing Group; 2006. p. MD2. (Technical Digest). Available from: https://opg.optica.org/abstract.cfm?URI=ASSP-2006-MD2

15. Shoji I, Kondo T, Kitamoto A, Shirane M, Ito R. Absolute scale of second-order nonlinear-optical coefficients. J Opt Soc Am B [Internet]. 1997;14(9):2268–94. Available from: http://www.osapublishing.org/josab/abstract.cfm?URI=josab-14-9-2268

16. Miller RC. OPTICAL SECOND HARMONIC GENERATION IN PIEZOELECTRIC CRYSTALS. Appl Phys Lett [Internet]. 1964 Jul 1;5(1):17–9. Available from: https://doi.org/10.1063/1.1754022

17. Leidinger M, Fieberg S, Waasem N, Kühnemann F, Buse K, Breunig I. Comparative study on three highly sensitive absorption measurement techniques characterizing lithium niobate over its entire transparent spectral range. Opt Express [Internet]. 2015;23(17):21690–705. Available from: http://opg.optica.org/oe/abstract.cfm?URI=oe-23-17-21690

18. Bai F, Wang Q, Liu Z, Zhang X, Wan X, Lan W, et al. Theoretical and experimental studies on output characteristics of an intracavity KTA OPO. Opt Express [Internet]. 2012;20(2):807–15. Available from: https://opg.optica.org/oe/abstract.cfm?URI=oe-20-2-807

19. Degnan JJ. Optimization of passively Q-switched lasers. IEEE J Quantum Electron. 1995;31(11):1890–901.

6 Conclusions

6.1 Summary

A theoretical analysis of both IC-OPOs and IC-BOPOs has been presented and compared to experimental results where applicable. The use of PPLN as the nonlinear material to achieve continuous wave operation of an IC-BOPO was discussed. It was shown that by using 5th order QPM, PPLN would be a suitable nonlinear material for use in an IC-BOPO as PPLN is commercially available with the required periods. Despite the reduction in effective nonlinear coefficient due to the 5th order QPM the threshold of IC-BOPO was able to be reached with a low power pump laser diode. Additionally, the maximum mid-IR output power when using a highly optimized cavity and a 20 W pump laser diode was found to be 3 W. Finally, the theoretical linewidth of mid-IR emission of 58 MHz was presented and discussed. It was shown that the proposed laser is capable of simultaneously achieving watt level mid-IR emission and narrow emission linewidth. The output power and linewidth demonstrate the proposed lasers suitability for use in day remote gas detection.

A theoretical systematic study on the output performance of an IC-BOPO was completed. Parameters such as cavity length, nonlinear crystal length, OC radius and pump laser diode spot size were varied systematically to study how they affect the laser performance. It was shown that to reduce the laser threshold, the cavity size should be reduced as much as possible. It was also shown that with proper cavity design output powers as high as 700 mW in the mid-IR could be achieved with the proposed laser structure using a 10 W laser diode as the pump source. Additionally, it was found that by reducing the OC radius from 100 mm to 50 mm it was possible to reach the threshold for the BOPO process using a 2 cm PPLN. It was also shown that the output power in the mid-IR increased as the spot size of the pump laser diode in the laser crystal was reduced; until a threshold was reached upon which the output power would rapidly drop off with a further decrease in spot size. Finally, it was demonstrated that despite the power of the backwards travelling idler wave being larger than that of the forwards, coupling it out of the cavity using a dichroic mirror reduced the performance due to the increase in intracavity loss from the dichroic mirror at the BOPO pump wavelength.

A model for a passively Q-switched IC-OPO was presented. The model accounts for thermalization between the stark levels of the upper and lower laser energy levels as well as excited state absorption in the Cr:YAG saturable absorber. The model also accounts for the time and spatial dependence of the field intensities within the nonlinear crystal. The model was validated using experimental results. A signal pulse width of 1.75 ns was calculated using the model, compared to an experimentally measured pulse width of 2 ns.

6.2 Future Work

The work presented focused on the development of theoretical models to simulate IC-OPO and IC-BOPO performance. To simplify the simulations, the plane wave assumption was made for all waves within the nonlinear crystal. As a result of this, the intensity is only dependent on the z-axis position, while being constant along the x- and y-axes. While the overlap integral of the fields within the nonlinear crystal was calculated and applied to the coupled wave equations to account for the spatial distribution, this is not a perfect fix. Ideally, the transverse intensity distribution of the waves would be accounted for. This can be accomplished by using a different numerical scheme such as the split step method and solving the paraxial coupled wave equations. The coupling of the coupled wave equations with the models for calculating the intracavity power can be done the same way when using a different solving method such as the split step method.

In addition to the plane wave approximation, it was also assumed that all fields in the model were single frequency. A result of this the described models are not capable of directly calculating the bandwidth of the generated waves. Instead, approximations were made using a first order Taylor Series expansion of the phase matching equation to estimate the bandwidth of the generated waves. This however does not account for intracavity effects which would narrow the spectrum of the confined wave. The next step would be to simulate the laser systems assuming some finite pump bandwidth and the existence of multiple longitudinal modes. For many applications, such as remote gas detection, the emission linewidth is of great interest necessitating the need for models capable of accurately calculating it.

Finally, much of the work presented here was theoretical in nature focusing on feasibility and optimization of IC-BOPO devices. Ideally this work will serve as a guideline for experimental realization of these lasers. Based on the results it is possible to realize a continuous wave IC-BOPO, which has not yet been demonstrated experimentally.

7 References

[1] T. H. MAIMAN, ‘Stimulated Optical Radiation in Ruby’, *Nature*, vol. 187, no. 4736, pp. 493–494, 1960, doi: 10.1038/187493a0.

[2] P. A. Franken, A. E. Hill, C. W. Peters, and G. Weinreich, ‘Generation of Optical Harmonics’, *Phys Rev Lett*, vol. 7, no. 4, pp. 118–119, Aug. 1961, doi: 10.1103/PhysRevLett.7.118.

[3] J. A. Giordmaine and R. C. Miller, ‘Tunable Coherent Parametric Oscillation in LiNb03 at Optical Frequencies’, *Phys Rev Lett*, vol. 14, no. 24, pp. 973–976, Jun. 1965, doi: 10.1103/PhysRevLett.14.973.

[4] R. G. Smith, J. E. Geusic, H. J. Levinstein, S. Singh, and L. G. Van Uitert, ‘Low-Threshold Optical Parametric Oscillator using Ba2NaNb5O15’, *J Appl Phys*, vol. 39, no. 8, pp. 4030–4032, Jul. 1968, doi: 10.1063/1.1656899.

[5] R. G. Smith, J. E. Geusic, H. J. Levinstein, J. J. Rubin, S. Singh, and L. G. Van Uitert, ‘CONTINUOUS OPTICAL PARAMETRIC OSCILLATION IN Ba2NaNb5O15’, *Appl Phys Lett*, vol. 12, no. 9, pp. 308–310, May 1968, doi: 10.1063/1.1652004.

[6] J. E. Bjorkholm, ‘SOME SPECTRAL PROPERTIES OF DOUBLY AND SINGLY RESONANT PULSED OPTICAL PARAMETRIC OSCILLATORS’, *Appl Phys Lett*, vol. 13, no. 12, pp. 399–401, Dec. 1968, doi: 10.1063/1.1652488.

[7] S. T. Yang, R. C. Eckardt, and R. L. Byer, ‘Continuous-wave singly resonant optical parametric oscillator pumped by a single-frequency resonantly doubled Nd:YAG laser’, *Opt Lett*, vol. 18, no. 12, pp. 971–973, 1993, doi: 10.1364/OL.18.000971.

[8] J. Bjorkholm, A. Ashkin, and R. Smith, ‘Improvement of optical parametric oscillators by nonresonant pump reflection’, *IEEE J Quantum Electron*, vol. 6, no. 12, pp. 797–799, 1970, doi: 10.1109/JQE.1970.1076366.

[9] F. G. Colville, M. H. Dunn, and M. Ebrahimzadeh, ‘Continuous-wave, singly resonant, intracavity parametric oscillator’, *Opt Lett*, vol. 22, no. 2, pp. 75–77, 1997, doi: 10.1364/OL.22.000075.

[10] G. A. Turnbull, M. H. Dunn, and M. Ebrahimzadeh, ‘Continuous-wave, intracavity optical parametric oscillators: an analysis of power characteristics’, *Applied Physics B*, vol. 66, no. 6, pp. 701–710, 1998, doi: 10.1007/s003400050456.

[11] T. Debuisschert, J. Raffy, J.-P. Pocholle, and M. Papuchon, ‘Intracavity optical parametric oscillator: study of the dynamics in pulsed regime’, *Journal of the Optical Society of America B*, vol. 13, no. 7, pp. 1569–1587, 1996, doi: 10.1364/JOSAB.13.001569.

[12] Y. F. Chen, S. W. Chen, Y. C. Chen, Y. P. Lan, and S. W. Tsai, ‘Compact efficient intracavity optical parametric oscillator with a passively Q-switched Nd : YVO4/Cr4+ : YAG laser in a hemispherical cavity’, *Applied Physics B*, vol. 77, no. 5, pp. 493–495, 2003, doi: 10.1007/s00340-003-1279-3.

[13] J. A. Armstrong, N. Bloembergen, J. Ducuing, and P. S. Pershan, ‘Interactions between Light Waves in a Nonlinear Dielectric’, *Physical Review*, vol. 127, no. 6, pp. 1918–1939, Sep. 1962, doi: 10.1103/PhysRev.127.1918.

[14] W. R. Bosenberg, A. Drobshoff, J. I. Alexander, L. E. Myers, and R. L. Byer, ‘Continuous-wave singly resonant optical parametric oscillator based on periodically poled LiNbO3’, *Opt Lett*, vol. 21, no. 10, pp. 713–715, 1996, doi: 10.1364/OL.21.000713.

[15] P. G. Schunemann *et al.*, ‘Continuous wavelength tuning from 3.9–12 µm from an optical parametric oscillator based on orientation-patterned GaP grown on GaAs’, *Opt Mater Express*, vol. 11, no. 3, pp. 654–663, 2021, doi: 10.1364/OME.417990.

[16] K. L. Vodopyanov, I. Makasyuk, and P. G. Schunemann, ‘Grating tunable 4 - 14 μm GaAs optical parametric oscillator pumped at 3 μm’, *Opt Express*, vol. 22, no. 4, pp. 4131–4136, 2014, doi: 10.1364/OE.22.004131.

[17] S. E. Harris, ‘PROPOSED BACKWARD WAVE OSCILLATION IN THE INFRARED’, *Appl Phys Lett*, vol. 9, no. 3, pp. 114–116, Aug. 1966, doi: 10.1063/1.1754668.

[18] C. Canalias and V. Pasiskevicius, ‘Mirrorless optical parametric oscillator’, *Nat Photonics*, vol. 1, no. 8, pp. 459–462, 2007, doi: 10.1038/nphoton.2007.137.

[19] C. E. Minor and R. S. Cudney, ‘Mirrorless optical parametric oscillation in bulk PPLN and PPLT: a feasibility study’, *Applied Physics B*, vol. 123, no. 1, p. 38, 2017, doi: 10.1007/s00340-016-6602-x.

[20] C. Liljestrand, A. Zukauskas, V. Pasiskevicius, and C. Canalias, ‘Highly efficient mirrorless optical parametric oscillator pumped by nanosecond pulses’, *Opt Lett*, vol. 42, no. 13, pp. 2435–2438, 2017, doi: 10.1364/OL.42.002435.

[21] G. Strömqvist, V. Pasiskevicius, C. Canalias, P. Aschieri, A. Picozzi, and C. Montes, ‘Temporal coherence in mirrorless optical parametric oscillators’, *Journal of the Optical Society of America B*, vol. 29, no. 6, pp. 1194–1202, 2012.

[22] Y. Peng, W. Wang, X. Wei, and D. Li, ‘High-efficiency mid-infrared optical parametric oscillator based on PPMgO:CLN’, *Opt Lett*, vol. 34, no. 19, pp. 2897–2899, 2009, doi: 10.1364/OL.34.002897.

[23] M. W. Haakestad, T. P. Lamour, N. Leindecker, A. Marandi, and K. L. Vodopyanov, 'Intracavity molecular spectroscopy in the mid-IR using ultra-broadband optical parametric oscillator', in *Proc.SPIE*, Mar. 2013, p. 86040T. doi: 10.1117/12.2006122.

[24] J. Hodgkinson and R. P. Tatam, 'Optical gas sensing: a review', *Meas Sci Technol*, vol. 24, no. 1, p. 12004, 2013, doi: 10.1088/0957-0233/24/1/012004.

[25] J. Randers and U. Goluke, 'An earth system model shows self-sustained thawing of permafrost even if all man-made GHG emissions stop in 2020', *Sci Rep*, vol. 10, no. 1, p. 18456, 2020, doi: 10.1038/s41598-020-75481-z.

[26] X. Zhang, S. Zhao, Q. Wang, Q. Zhang, L. Sun, and S. Zhang, 'Optimization of Cr/sup 4+/-doped saturable-absorber Q-switched lasers', *IEEE J Quantum Electron*, vol. 33, no. 12, pp. 2286–2294, 1997, doi: 10.1109/3.644112.

[27] He Jing-liang *et al.*, 'Cr4+:YAG as a Passive Q-Switch in a Diode-Pumped cw Nd:YVO4 Laser', *Chinese Physics Letters*, vol. 15, no. 12, p. 883, 1998, doi: 10.1088/0256-307X/15/12/009.

[28] Y. P. Huang, Y. J. Huang, C. Y. Cho, and Y. F. Chen, 'Influence of output coupling on the performance of a passively Q-switched Nd:YAG laser with intracavity optical parametric oscillator', *Opt Express*, vol. 21, no. 6, pp. 7583–7589, 2013, doi: 10.1364/OE.21.007583.

[29] F. Bai *et al.*, 'Theoretical and experimental studies on output characteristics of an intracavity KTA OPO', *Opt Express*, vol. 20, no. 2, pp. 807–815, 2012, doi: 10.1364/OE.20.000807.

[30] R. W. Boyd, *Nonlinear Optics*. Elsevier Science, 2020. [Online]. Available: https://books.google.ca/books?id=9Ic0swEACAAJ

[31] G. Rustad, G. Arisholm, and Ø. Farsund, 'Effect of idler absorption in pulsed optical parametric oscillators', *Opt Express*, vol. 19, no. 3, pp. 2815–2830, 2011, doi: 10.1364/OE.19.002815.

[32] S. M. Spillane, M. Fiorentino, and R. G. Beausoleil, 'Spontaneous parametric down conversion in a nanophotonic waveguide', *Opt Express*, vol. 15, no. 14, pp. 8770–8780, 2007, doi: 10.1364/OE.15.008770.

[33] W. P. Risk, 'Modeling of longitudinally pumped solid-state lasers exhibiting reabsorption losses', *Journal of the Optical Society of America B*, vol. 5, no. 7, pp. 1412–1423, 1988, doi: 10.1364/JOSAB.5.001412.

[34] H. Ridderbusch and T. Graf, 'Saturation of 1047- and 1064-nm Absorption in ${\hbox {Cr}}^{4+}$:YAG Crystals', *IEEE J Quantum Electron*, vol. 43, no. 2, pp. 168–173, 2007, doi: 10.1109/JQE.2006.889055.

[35] J. J. Degnan, D. B. Coyle, and R. B. Kay, 'Effects of thermalization on Q-switched laser properties', *IEEE J Quantum Electron*, vol. 34, no. 5, pp. 887–899, 1998, doi: 10.1109/3.668777.

[36] J. Kneller, S. Salimian Rizi, L. Flannigan, and C. Xu, 'The effects of thermalization on the performance of passively Q-switched IC-OPOs', *Front Phys*, vol. 12, 2024, [Online]. Available: https://www.frontiersin.org/journals/physics/articles/10.3389/fphy.2024.1428671

[37] H. Sakai, A. Sone, H. Kan, and T. Taira, 'Polarization stabilizing for diode-pumped passively Q-switched Nd:YAG microchip lasers', in *Advanced Solid-State Photonics*, in Technical Digest. Incline Village, Nevada: Optica Publishing Group, 2006, p. MD2. doi: 10.1364/ASSP.2006.MD2.

[38] S. Li, S. Zhou, P. Wang, Y. C. Chen, and K. K. Lee, 'Self-Q-switched diode-end-pumped Cr,Nd:YAG laser with polarized output', *Opt Lett*, vol. 18, no. 3, pp. 203–204, 1993, doi: 10.1364/OL.18.000203.

[39] M. Catela *et al.*, 'Doughnut-Shaped and Top Hat Solar Laser Beams Numerical Analysis', *Energies (Basel)*, vol. 14, p. 7120, Oct. 2021, doi: 10.3390/en14217102.

[40] J. Kneller, L. Flannigan, and C.-Q. Xu, 'Theoretical study of diode pumped intracavity backward optical parametric oscillator based on periodically poled lithium niobate', *Applied Physics B*, vol. 129, no. 6, p. 99, 2023, doi: 10.1007/s00340-023-08045-4.

[41] P. Lax and B. Wendroff, 'Systems of conservation laws', *Commun Pure Appl Math*, vol. 13, no. 2, pp. 217–237, May 1960, doi: https://doi.org/10.1002/cpa.3160130205.